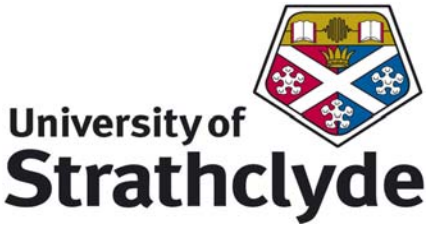

Department of Physics

Microwave Pulse Compression using 3-Fold and 5-Fold Helically Corrugated Waveguides

Michael McStravick

(B.Sc., M.Sc., University of Strathclyde)

Thesis submitted for the Degree of Ph.D.

September 2011

This thesis is the result of the author's original research. It has been composed by the author and has not been previously submitted for examination which has led to the award of a degree.

Signed:
Date:

I would like to dedicate this thesis to the memory of Christopher McStravick.

CONTENTS

Acknowledgements VIII
Abstract IX
Table of Abbreviations X
Table of Symbols XII
Table of Figures XV
Table of Tables XXIII

Chapter 1 Microwave Pulse Compression 24

1.1 Applications of microwaves 25
1.2 Microwave pulse compression techniques 27
1.3 Sweep-frequency microwave pulse compression 30
1.4 Circular waveguide pulse compressor 33
1.5 Helically corrugated waveguide pulse compressor 34
1.6 Previous research 35
1.7 Research pursued in this thesis 35

Chapter 2 Electromagnetism and Waveguide Theory 37

2.1 Classical electromagnetism 38
2.2 Waveguides 40
2.3 Rectangular waveguide theory 42
2.4 Circular waveguide theory 48
2.5 Electromagnetic wave velocity 52
2.6 Power density of electromagnetic wave 54
2.7 Waveguide losses 55
2.8 Helically corrugated waveguide theory 56
2.9 Physics of microwave pulse compression 58
2.10 Theoretical compression of a frequency-swept microwave pulse 60

Chapter 3 The 3-fold Helically Corrugated Waveguide 62

3.1 Physics of a 3-fold helically corrugated waveguide 63
3.2 Eigenwave dispersion calculated analytically 65
3.3 Eigenwave dispersion calculated numerically 69
3.4 Eigenwave dispersion calculated experimentally 73
3.5 Analysis of eigenwave dispersion results 76
3.6 Losses measurement using SNA 78
3.7 Losses measurement using VNA 80
3.8 Analysis of losses results 82
3.9 Simulation of microwave pulse compression 84

Chapter 4 The 3-Fold Pulse Compression Experiments 86

4.1 Introduction to pulse compression experiments 87
4.2 Pulse compression experiments at mW powers 87
4.2.1 Measurement of a.c. microwave input pulse 87
4.2.2 Measurement of a.c. microwave output pulse 91
4.3 Method of attenuation experiment at mW powers 95
4.3.1 Measurement of rectified input microwave pulse 95
4.3.2 Measurement of rectified output microwave pulse 96
4.4 Pulse compression experiments at kW powers 98
4.4.1 Measurement of kW input and output microwave pulses 101
4.5 Method of attenuation experiment at kW powers 104

Chapter 5 The 5-fold Helically Corrugated Waveguide 107

5.1 Introduction 108
5.2 Design of a 5-fold microwave pulse compressor 108
5.3 Manufacture and construction of waveguides 116
5.4 Eigenwave dispersion calculated analytically 119
5.5 Eigenwave dispersion calculated numerically 123
5.6 Eigenwave dispersion calculated experimentally 126
5.7 Analysis of eigenwave dispersion results 130
5.8 Losses measurements in 5-fold waveguide system 132
5.8.1 SNA measurement 132
5.8.2 VNA measurement 134
5.9 Simulation of microwave pulse compression 137

Chapter 6 The 5-Fold Pulse Compression Experiments 138

6.1 Introduction to 5-fold compression experiments 139
6.2 Pulse compression experiments at mW powers 139
6.2.1 Measurement of a.c. input microwave pulse 139
6.2.2 Measurement of a.c. output microwave pulse 141
6.3 Pulse compression at kW powers 144
6.3.1 Measurement of a.c. input microwave pulse 145
6.3.2 Measurement of a.c. output microwave pulse 147
6.4 Method of attenuation at kW powers 149

Chapter 7 Conclusion 151

7.1 Overview of study 152
7.2 Microwave pulse compression experiments 153
7.2.1 The 3-fold microwave pulse compressor 153
7.2.2 The 5-fold microwave pulse compressor 154
7.3 Possible applications of findings from study 154
7.4 Future work 154
7.4.1 Gyro-TWT 154
7.4.2 Frequency-swept BWO 155
7.5 Discussion 155

References 157

Appendices 167
Appendix A Overview of vacuum electronics and devices 168
Appendix B Maxwell's equations in matter 175
Appendix C Mode patterns for rectangular and circular waveguide 178
Appendix D Matlab code to calculate dispersion using coupled wave theory 179
Appendix E VBA macro for helically corrugated waveguide 181
Appendix F Polarisation 182
Appendix G Matlab code to drive AWG in pulse compression experiments 187
Appendix H Matlab code for analysis of measured input pulses 191
Appendix I Author's publications 193

ACKNOWLEDGEMENTS

I would like to sincerely thank Professor Alan Phelps and my Ph.D. supervisors Dr. Adrian Cross, Dr. Wenlong He and Dr. Colin Whyte. I would particularly like to thank Dr. Cross for his constant guidance and encouragement.

I would like to extend thanks to Dr. Alan Young and Dr. Craig Robertson for their contribution with technical design studies on the production of the pulse compressor. Dr Kevin Ronald is thanked for his expertise and guidance with VNA measurements. Mr David Barclay and Mr Bob Wiley are thanked for their expert work in the manufacturing of the helically corrugated waveguides.

I would like to thank Dr. Sergey Samsonov and Mr Sergey Mishakin both from the Institute of Applied Physics in Russia for their theoretical and technical insights.

I would like to thank UK EPSRC, JGS scheme and the Faraday Partnership in High Power RF for supporting this work.

I would like to thank mum, dad and Gary for their continual and unwavering support in my education.

ABSTRACT

The use of an over-moded circular waveguide with helical corrugations of its inner surface as a dispersive medium enables compression of frequency-modulated microwave pulses. The helical corrugation couples a pair of partial modes of the circular waveguide having significantly different group velocities. As a result of the resonant coupling an eigenmode of the helically corrugated waveguide appears which has a strongly frequency dependent group velocity, which is favourable for the pulse compression. Two helically corrugated waveguide structures were investigated as sweep-frequency microwave pulse compressors for X-band microwave radiation.

The investigation comprised the analytical, numerical and experimental study of the eigenwave and group velocity dispersion characteristics for the 3-fold and 5-fold helically corrugated waveguide compressors. Sweep-frequency based microwave pulse compression experiments were carried out at low (mW) and medium (kW) power levels.

A 3-fold helically corrugated waveguide system resonantly coupled the fast-travelling counter-rotating $TE_{1,1}$ mode and $TE_{2,1}$ near cut-off mode. A 5.6 kW, 80 ns input pulse with 5 % frequency modulation from a conventional TWT was compressed to a maximum peak power of 140 kW, 1.5 ns pulse resulting in a peak power amplification of 22.5 ± 2.5 times, where 42 ± 5 % of the input energy was compressed to the main body of the output pulse.

A larger diameter 5-fold helically corrugated waveguide system was designed to compress microwave pulses with frequency-modulation within the frequency interval 9.0 GHz to 9.6 GHz and simultaneously provide low reflection of the input radiation within a frequency interval of 8.0 GHz to 10.0 GHz. The 5-fold helically corrugated waveguide resonantly coupled the fast-travelling counter-rotating $TE_{3,1}$ mode and $TE_{2,2}$ near cut-off mode. An input pulse of 5.8 kW, 85 ns duration was compressed to a maximum peak power of 144 kW, 1.5 ns pulse resulting in a peak power compression ratio of 22.3 ± 2.5 and compression efficiency of 40 ± 5 %.

TABLE OF ABBREVIATIONS

ABC	Active Bragg Compressor
a.c.	Alternating Current
AKS	Advanced Krylov Subspace
AWG	Arbitrary Waveform Generator
BPM / BPC	Binary Power Multiplier / Binary Pulse Compressor
BWO	Backward Wave Oscillator
CNC	Computer Numerical Control
CST MWS	Computer Simulation Technology Microwave Studio
CW	Continuous Wave
dB	Decibel
DC	Direct Current
DSO	Digital Storage Oscilloscope
DUT	Device Under Test
FEA	Finite Element Analysis
FEL	Free Electron Laser
FM	Frequency-Modulated
FWHM	Full Width Half Maximum
GPIB	General Purpose Interface Bus
GUI	Graphical User Interface
Gyro	Gyrotron
HP	Hewlett Packard
IQ	In-phase and Quadrature data
LRL	Line-Reflect-Line
PDE	Partial Differential Equation
Q-factor	Quality Factor
Radar	Radio Detection and Ranging
RELS	Resonant Line SLED
RF	Radio Frequency
S-parameter	Scattering parameter
SES	Switched Energy Storage

SLAC	SLAC National Accelerator Laboratory
SLED / II	SLAC Energy Development / 2nd Generation
SNA	Scalar Network Analyzer
TE	Transverse Electric
TEM	Transverse Electromagnetic
TM	Transverse Magnetic
TWT	Travelling Wave Tube
VBA	Visual Basic Application
VNA	Vector Network Analyzer
VSG	Vector Signal Generator
WG	Waveguide

TABLE OF SYMBOLS

$\underline{E}$	Electric field strength
$\underline{B}$	Magnetic flux density
$\underline{D}$	Electric flux density
$\underline{H}$	Magnetic field strength
$\underline{J}$	Current density
$\underline{J}_f$	Free current density
$\underline{J}_b$	Bound current density
$\underline{J}_p$	Polarisation current density
$\underline{P}$	Electric polarisation
$\underline{M}$	Magnetisation
ρ	Charge density
ρ_f	Free charge density
ρ_b	Bound charge density
Q	Charge
ε	Permittivity of a material
ε_0	Electric permittivity of free space
ε_r	Relative electric permittivity of material
μ	Permeability of a material
μ_0	Magnetic permeability of free space
μ_r	Relative magnetic permeability of material
f	Frequency
f_c	Cut-off frequency
ω	Angular frequency
ω_c	Cut-off angular frequency
λ	Wavelength in free-space
λ_g	Waveguide wavelength

λ_c	Cut-off wavelength
k	Wave number
k_g	Waveguide wave number
k_c	Cut-off wave number
$k_\perp$	Transverse wavenumber
k_z	Axial wave number
c	Speed of electromagnetic wave in free-space
m,n	Waveguide mode numbers
ζ_{mn}	n^{th} root of the m^{th} Bessel function
P	Power
t	Time
E	Energy
E_{out}	Energy in compressed pulse
E_{in}	Energy in input pulse
v	Velocity
v_{gr}	Group velocity
v_{ph}	Phase velocity
φ	Phase
δ	Skin depth
σ	Electrical conductivity
I	Current
R	Resistance
u_e	Energy within electric field
u_m	Energy within magnetic field
$\underline{S}$	Poynting's vector
$\underline{S}_{av}$	Time-averaged Poynting's vector
r_0	Mean radius
l	Corrugation amplitude
d	Corrugation period

N_c	Total number of periods of helix
m_B	Azimuthal number of Bragg periodicity vector
m_1	Azimuthal indice of wave co-rotating in helix
m_2	Azimuthal indice of wave counter-rotating in helix
k_B	Axial component of Bragg periodicity vector
k_{z1}	Axial wave number of wave co-rotating in helix
k_{z2}	Axial wave number of wave counter-rotating with helix
$k_{\perp 1}$	Cut-off wavenumber of wave co-rotating in helix
$k_{\perp 2}$	Cut-off wavenumber of wave counter-rotating in helix
k_0	Wave vector of exact Bragg resonance
κ	Coupling coefficient
S_1	Normalised coupling coefficient of wave co-rotating in helix
S_2	Normalised coupling coefficient of wave counter-rotating in helix
θ	Boundary phase angle
W_1	Operating eigenwave
W_2	Upper eigenwave
L	Length of compressor
L_{opt}	Optimum length of compressor
P_{inst}	Instantaneous power
P_{in}	Input power
P_{peak}	Peak power
τ_{in}	Input pulse duration
τ_c	Compressed pulse duration
C_t	Time compression ratio
C_p	Power compression ratio
Δf	Frequency-modulation band
γ	Attenuation coefficient
η_c	Compression efficiency

TABLE OF FIGURES

Figure 1-1 Illustration of the principle of pulse compression 30

Figure 1-2 Illustration of frequency-modulation of input pulse..... 31

Figure 1-3 Illustration of group velocity change in a dispersive medium 31

Figure 1-4 Illustration of compressed pulse in a dispersive medium..... 32

Figure 1-5 Schematic of dispersion diagram of $TE_{1,1}$ mode in circular waveguide 33

Figure 1-6 Schematic of dispersion diagram of helically corrugated waveguide showing operating eigenmode 34

Figure 2-1 Schematic of rectangular waveguide geometry..... 42

Figure 2-2 Schematic of electromagnetic wave propagating in rectangular waveguide 44

Figure 2-3 The electric field in rectangular waveguide at some value z..... 44

Figure 2-4 The z-dependence of the field in the waveguide; E is the electric field (red arrows) and B is the magnetic field (black dots)..... 45

Figure 2-5 Electric, magnetic and current field pattern of the $TE_{1,0}$ mode of a rectangular waveguide, Dobbs 1985 47

Figure 2-6 Schematic of circular waveguide geometry 48

Figure 2-7 Schematic of dispersion diagram for modes in circular waveguide showing phase velocity (v_{ph}) and group velocity (v_{gr}) 52

Figure 3-1 Schematic of a 3-fold helically corrugated waveguide 63

Figure 3-2 Digital photograph of a section of 3-fold helically corrugated waveguide 64

Figure 3-3 Dispersion diagram: (1) is a lower partial mode of a smooth circular waveguide, (2) is a spatial harmonic of a near cut-off mode; W_1 and W_2 are the eigenmodes of the helical-waveguide 64

Figure 3-4 Dispersion diagram of 3-fold helically corrugated waveguide calculated using coupled wave theory from Matlab code..... 67

Figure 3-5 Eigenmode dispersion plot from coupled wave theory data 67

Figure 3-6 Group velocity dispersion plot calculated from coupled wave theory eigenwave dispersion data..... 68

Figure 3-7 Curve outline of 3-fold helical face created using VBA macro ... 69

Figure 3-8 CST MWS model of single period of 3-fold helical waveguide .. 70

Figure 3-9 Eigenmode contour plots of (a) electric field and (b) magnetic field; red is region of larger amplitude and blue is lower amplitude..... 71

Figure 3-10 Eigenmode dispersion plot using CST MWS data..... 71

Figure 3-11 Group velocity dispersion plot calculated from CST MWS eigenwave dispersion data..... 72

Figure 3-12 Experimental set-up in RF laboratory for 3-fold helically corrugated waveguide dispersion measurement using VNA 73

Figure 3-13 VNA phase measurement: (a) raw data from experiment and (b) after digital processing to remove 360˚ phase jumps..... 74

Figure 3-14 Eigenmode dispersion plot from VNA measurement data..... 75

Figure 3-15 Group velocity dispersion plot using VNA eigenwave dispersion data 75

Figure 3-16 Chart of eigenwave dispersion results..... 76

Figure 3-17 Chart of group velocity dispersion results..... 76

Figure 3-18 SNA losses measurement (a) Experimental set-up in RF laboratory and (b) schematic of set-up for measurement..... 78

Figure 3-19 SNA transmission (S_{21}) measurement 8.8 GHz – 9.8 GHz..... 79

Figure 3-20 Experimental set-up in RF laboratory for losses measurement using VNA 80

Figure 3-21 VNA transmission (S_{21}) measurement 8.8 GHz – 9.8 GHz 80

Figure 3-22 Chart of 3-fold helically corrugated waveguide losses from SNA and VNA measurements 82

Figure 3-23 Optimum frequency-sweep for 3-fold helical waveguide..... 85

Figure 3-24 Simulation of input pulse and compressed pulses..... 85

Figure 4-1 Input (a) pulse shape (b) frequency-sweep for AWG 88

Figure 4-2 Experimental set-up in RF laboratory for 3-fold microwave pulse compression experiments at mW power levels 89

Figure 4-3 Input pulse measurement (a) real-time a.c. input pulse on DSO and (b) chart of measured input pulse using Microsoft Excel 90

Figure 4-4 Power envelope of measured microwave input pulse 90

Figure 4-5 Frequency sweep: Measured (blue) and AWG programmed sweep (red) 91

Figure 4-6 Schematic of mode transformation from input-to-output in 3-fold helically corrugated waveguide compressor 92

Figure 4-7 (a) Measurement of compressed RF pulse on 12 GHz DSO and (b) chart of compressed microwave pulse..... 93

Figure 4-8 Power envelope of measured compressed microwave pulse..... 93

Figure 4-9 Measurement of rectified input microwave pulse 95

Figure 4-10 Experimental set-up to measure rectified output pulse 96

Figure 4-11 Measurement of rectified compressed microwave pulse..... 97

Figure 4-12 Schematic of experimental set-up for kW pulse compression experiments 98

Figure 4-13 Digital photograph of trigger set-up for TWT..... 99

Figure 4-14 Digital photograph of TWT and RF isolator 100

Figure 4-15 Digital photograph of experimental set-up in RF laboratory for kW pulse compression experiments 101

Figure 4-16 Input pulse details for kW pulse compression experiment 102

Figure 4-17 Power meter measurement of input pulse 102

Figure 4-18 Power envelope of compressed kW pulse 103

Figure 4-19 Digital photograph of measured rectified input pulse 104

Figure 4-20 Measurement of rectified input pulse to compressor from TWT .. 105

Figure 4-21 Measurement of rectified compressed microwave pulse 105

Figure 5-1 Schematic of 5-fold helically corrugated waveguide pulse compressor system 109

Figure 5-2 Model of input cone, mode converter, and intermediate cone created using CST MWS 112

Figure 5-3 Simulation of the input mode to the mode converter 112

Figure 5-4 Simulation of the output mode from the mode converter 113

Figure 5-5 The S-parameters measured using CST MWS at output of the mode converter 113

Figure 5-6 Digital photograph of CNC machine cutting 5-fold helical shape onto aluminium former 116

Figure 5-7 Machined waveguide pieces: (a) aluminium mandrels and (b) after electroform deposition 117

Figure 5-8 Waveguide pieces; (a) waveguide system components (b) intermediate cones and tapers (c) input cone and mode converter and (d) regular 5-fold compressor section 117

Figure 5-9 The 5-fold pulse compressor waveguide connection pieces 118

Figure 5-10 Dispersion diagram for 5-fold helically corrugated waveguide calculated from coupled wave theory using Matlab code..... 121

Figure 5-11 Eigenwave dispersion calculated analytically using coupled wave theory data 121

Figure 5-12 Group velocity chart calculated from analytical eigenwave dispersion data of coupled wave theory 122

Figure 5-13 (a) 5-fold face outline and (b) single period of 5-fold helically corrugated waveguide created using CST MWS 123

Figure 5-14 Eigenmode for 5-fold helix; (a) electric field and (b) axial magnetic field..... 124

Figure 5-15 Eigenwave dispersion chart using CST MWS data..... 124

Figure 5-16 Eigenwave group velocity chart using CST MWS data..... 125

Figure 5-17 Digital photograph of experimental set-up in RF laboratory 126

Figure 5-18 Chart of measured phase on VNA..... 127

Figure 5-19 Chart of phase after digital processing to remove phase jumps 128

Figure 5-20 Eigenwave dispersion chart from measured VNA data..... 128

Figure 5-21 Group velocity dispersion chart using eigenwave dispersion data from VNA 129

Figure 5-22 Comparison of eigenwave dispersion results 130

Figure 5-23 Comparison of group velocity dispersion results 131

Figure 5-24 Losses measurement in 5-fold using SNA 132

Figure 5-25 Experimental set-up for VNA losses measurement..... 134

Figure 5-26 Transmission (S_{21}) measurement in 5-fold using VNA..... 134

Figure 5-27 Comparison of losses measurements using SNA and VNA 135

Figure 5-28 Optimum frequency-sweep for 5-fold helix..... 137

Figure 5-29 Simulation of pulse compression in 5-fold helix 137

Figure 6-1 Frequency-sweep data from AWG of the input pulse to 5-fold helically corrugated waveguide compressor 139

Figure 6-2 Measurement of a.c. input microwave pulse on 12 GHz DSO 140

Figure 6-3 Frequency sweep of input pulse; red is AWG and blue is calculated frequency sweep from measured input pulse data 140

Figure 6-4 Power envelope of the input pulse to 5-fold compressor 141

Figure 6-5 Digital photograph of compressed pulse displayed on DSO..... 141

Figure 6-6 Chart of measured a.c. microwave compressed pulse..... 142

Figure 6-7 Chart of power envelope of compressed microwave pulse..... 142

Figure 6-8 Digital photograph of experimental set-up to measure the a.c. input microwave pulse to the compressor from the TWT..... 144

Figure 6-9 Chart of AWG frequency sweep for the input pulse..... 145

Figure 6-10 (a) Measured input pulse from the TWT and (b) Attenuated input pulse plotted on Microsoft Excel 146

Figure 6-11 Chart of the frequency response of measured input pulse 146

Figure 6-12 Chart of power envelope of input microwave pulse..... 147

Figure 6-13 Measured output (compressed) pulse using 12 GHz DSO..... 147

Figure 6-14 Chart of power envelope of compressed kW microwave pulse 148

Figure 6-15 Measurement of (a) rectified input and (b) rectified output pulse . 149

Figure 7-1 Schematic of (a) circular compressor and (b) helically corrugated waveguide dispersion diagrams 152

TABLE OF TABLES

Table 2-1 Zeros for Bessel functions of the first kind $J_m(\nu) = 0$ for the TM modes 49

Table 2-2 Zeros for derivatives of Bessel functions of the first kind $dJ_m(\nu)/d\nu$ for the TE modes 50

Table 3-1 The 3-fold helically corrugated waveguide parameters..... 63

Table 3-2 Group velocity results for 3-fold helically corrugated waveguide 77

Table 3-3 Loss measurements for 3-fold compressor using SNA 79

Table 3-4 Loss measurements for 3-fold compressor using VNA..... 81

Table 3-5 Comparison of loss measurements for SNA and VNA 82

Table 5-1 The 5-fold helically corrugated waveguide parameters..... 115

Table 5-2 Group velocity results for 5-fold helically corrugated waveguide 131

Table 5-3 Loss measurements for 5-fold compressor using SNA 133

Table 5-4 Loss measurements for 5-fold compressor using VNA..... 135

Table 5-5 Comparison of loss measurements for SNA and VNA 136

Chapter 1

Microwave Pulse Compression

The chapter begins with an introduction on microwaves and extends to a description on the applications of microwaves within science and industry. This is followed by a review of various types of microwave pulse compression techniques. The use of both circular and helically corrugated waveguides as dispersive media for the passive sweep-frequency based microwave pulse compression is discussed. A synopsis of the thesis research carried out within the Atoms, Beams and Plasmas group at the University of Strathclyde for X-band sweep-frequency based microwave pulse compression concludes the chapter.

1.1 APPLICATIONS OF MICROWAVES

Microwaves are electromagnetic waves of very short wavelength and arise as radiation from electrical disturbances at high frequencies, [Fuller 1969]. The microwave band designates the range of frequencies in the electromagnetic spectrum from about 300 MHz where the wavelength is 1 m to 300 GHz where the wavelength is 1 mm, [Phelps 1997]. Microwave frequencies are also grouped into smaller bands designated by letters. This thesis is concerned with X-band microwave frequencies which range from about 8.20 GHz to 12.40 GHz, corresponding to a wavelength range of around a few centimetres, [Ishii 1989, 1995, Seeger 1986].

Microwaves can be bound and directed using microwave transmission lines such as coaxial lines or waveguides. Coaxial lines are two concentric metallic conductors separated by a non-conductor. The lines are often flexible but generally cannot transmit large amounts of power, [Cook 1986, Scott 2005]. For many applications, waveguides are the better choice, as they are able to transmit higher frequency radiation at higher powers with reduced losses as compared to coaxial cables. Typically, waveguides are metallic tubes, usually, of a circular or rectangular cross section of specific dimensions. It is these waveguide dimensions which determine the frequency of microwave radiation that such waveguides can support, [Pozar 1998].

Microwave sources can be either continuous wave (CW) or pulsed and typically high-power means CW sources with average powers of tens of kWs to MWs and pulsed sources are capable of peak powers from MWs to GWs, [Benford 2007]. Solid state devices are successful sources of generating microwaves at lower power levels, however for the higher power levels above a few 100 Ws at high frequencies (X-band and above) and for MW power levels, vacuum electronic devices are the main sources in use, [Barker 2001, Cairns 1997, Gilmour 1986, Granatstein 1987]. An overview detailing the developments within the field of microwave vacuum electronics and high-power microwave sources can be located in Appendix A.

Applications of microwaves and microwave sources can be found in many areas of science and technology including radar technology, plasma physics, particle physics and medicine. Radar systems are used to locate and characterise remote distant objects such as range, altitude, direction or speed of an object by using the reflected electromagnetic energy from the object. The frequency of the microwave radiation used in radar allows the waves to penetrate fog and clouds which allows for obstacles that are not visible to the naked eye to be detected, [Cook 1986, Page 1962]. Advances in radar systems are concerned with improving the processing of the returned echo signal and in the development of high-power microwave sources such as high-peak power, short pulse (ns) sources and longer (μs) millimetre-wave sources, [Gold 1997].

In plasma physics microwave energy is used for heating and driving steady-state currents in magnetically confined plasmas for controlled fusion experiments in tokamaks. The plasma is heated by ion cyclotron heating (ICH), lower hybrid heating (LHH) or electron cyclotron heating (ECR). Much focus is on gyrotrons for electron-cyclotron heating and current drive at frequencies above 100 GHz, [Cohen 1991].

In the field of high-energy particle physics, accelerators are used to increase the speed of particles in a beam(s) to close to the speed of light to be used in, for example, experimental physics programs such as the Large Hadron Collider (LHC) experiment at CERN (European Organisation for Nuclear Research). RF microwave sources are used to power such particle accelerators and microwave amplifiers are used in the RF acceleration of the particles, [Granatstein 1996].

In medicine microwaves are used in medical linear accelerator systems to aid in the acceleration of the electron beam to produce x-rays for use in radiotherapy. Abnormalities of the heart such as supra-ventricular arrhythmia can be treated with localised high-power microwave beams to ablate the abnormal tissue. The thermal effects of the electromagnetic fields are used in procedures to help patients with back pain, liver cancer and varicose veins, [Rosen 2002, Vrba 2005].

1.2 MICROWAVE PULSE COMPRESSION TECHNIQUES

The principles and methods of microwave pulse compression have been studied for many decades and there is great interest in microwave pulse compressors since ultra-high-power microwave pulses are used in plasma experiments, particle accelerators and in high-resolution radar [Gaponov-Grekhov 1994] as discussed in section 1.1.

Microwave pulse compression can be achieved using either a passive pulse compressor or an active pulse compressor. Typically, passive pulse compressors consist of a passive RF circuit with frequency dispersion and require a phase-modulated RF input pulse. This ensures different components of the pulse spectrum travel with different velocities so that all these components arrive at the compressor output simultaneously. Active compressors do not require a frequency-modulated input pulse. If microwave energy is injected into a microwave cavity during a long time period and then extracted during a short time period, the microwave power is enlarged. For such an active pulse compressor the Q-factor of the cavity in the accumulation period should be much higher than in the extraction part, [Thumm 2002]. A combined active-passive compressor is reported that consists in combining an electrically controlled phase shifter with a passive compressor, [Petelin 2000].

SLAC National Accelerator Laboratory in California USA, houses the longest RF linear accelerator in the world at around two miles long. The high-power microwave group at SLAC investigate various microwave pulse compressors for applications in particle accelerators, [Hirshfield 2004, Tantawi 1999, 2004 and 2005].

An active method of microwave pulse compression is the binary power multiplier (BPM) device or binary pulse compressor (BPC) which multiplies RF power in binary steps. The BPC usually comprises of one or more stages, each of which doubles the input power and halves the input pulse duration. The BPC includes a front-end, a pair of high-power klystron amplifiers, and one or more compression stages. The front-end consists of a power splitter and two bi-phase modulators which

encode the klystron inputs in accordance with either a zero or 180˚ phase shift. The klystron outputs are connected to one or more pulse compression stages. Each stage consists of a 3 dB hybrid coupler with one output port connected to a delay line with a delay equal to half the input pulse duration and the other end connected to zero delay transmission line. Compression factors of up to 8 have been reported using a 3-stage BPC device with superconducting delay lines, [Farkas 1986, 1989 and 1993].

Switched energy storage (SES) is another active pulse compression method. This method generates short high-power microwave pulses by storing RF microwave energy in a resonant cavity over a relatively long fill-time and extracting it very rapidly by changing the Q-factor of the cavity. Using this pulse compression technique power gain roughly equal to the ratio of fill time to extraction time can be obtained. During the filling of a resonant cavity some of the energy is lost in heating of the cavity walls and some will generally be reflected at the input coupling of the cavity. Commonly a plasma discharge is used to 'switch' the energy stored in the superconducting resonator to an external load, [Birx 1978]. The SES method of pulse compression has generated power compression factors of up to 35, [Alvarez 1986].

In the SLAC energy development (SLED) RF pulse compression system a Klystron is used to build up the fields in two high-Q resonators for a relatively long time interval around 3 μs to 5 μs. Triggered by a reversal in RF phase, the stored energy is released during a much shorter interval equal to the filling time of the accelerating structure. Peak power gains of approximately 3 with a compression efficiency of about 60 % have been attained. One drawback to the SLED system is the shape of the output pulse is a sharply decaying exponential, [Farkas 1974].

In the 2nd generation SLED (SLED-II) the two cavities are replaced by two lengths of resonant line, forming a Resonant Line SLED (RELS) to store the energy during most of the duration of the incoming pulse, [Gold 1997, Nantista 1993]. A resonant line is a transmission line terminated in a short circuit and connected to an input transmission line via a coupling network. The distance between the coupling network and the short must be an integral multiple of half-guide wavelengths. The round-trip

time of an RF signal through one of the delay lines determines the length of the compressed pulse. To discharge the lines, the phase of the incoming pulse is reversed by 180˚ ensuring the reflected signal from the inputs of the lines and the emitted fields from the lines add constructively, producing a high-power compressed pulse. The RELS system has the advantage over the SLED system in that it produces a flat-topped rectangular output pulse. Using this arrangement RELS stages can be cascaded to give a greater peak power compression factor, [Wilson 1990].

To enhance the efficiency of the SLED-II system an active variation of the SLED-II utilises the notion of changing the coupling coefficient of the storage RF lines during the discharge phase thus the intrinsic efficiency of the system can reach 100 % using this time-switched line, [Tantawi 1996]. A high-power microwave switch using optical excitation of an electron-hole plasma layer on the surface of a pure silicon wafer and designed to operate in the $TE_{0,1}$ mode in a circular waveguide was used to discharge the resonant delay lines, [Tantawi 1997].

A further example of an active microwave pulse compressor is the Active Bragg Compressor (ABC). The ABC operates in the $TE_{0,1}$ mode and utilises an oversized waveguide and electrically controlled Bragg reflectors. Power compression ratios in the range of 11 to 12 with a compression efficiency of 50 % were reported, [Vikharev 1999].

There are other active pulse compression techniques using various types of switches as active elements, such as the X-band electrically controlled ferroelectric switch, [Yakovlev 2003], and more recent advances have been documented in the developments of plasma switch tubes in active pulse compression techniques, [Vikharev 2003, 2004 and 2009].

1.3 SWEEP-FREQUENCY MICROWAVE PULSE COMPRESSION

In principle, microwave pulse compression is a technique used to compress a long duration lower-power pulse P_{in} , with pulse duration τ_{in} , into a short duration higher-power pulse P_{peak} , with compressed duration τ_c , as illustrated in Figure 1-1. The input pulse $u_0(t)$ is given by $u_0(t) = A_0 \sin(\omega t)$, where A_0 is the amplitude of the wave, ω is the angular frequency and $\omega = 2\pi f(t)$ where f is the frequency given by $f = f(t)$.

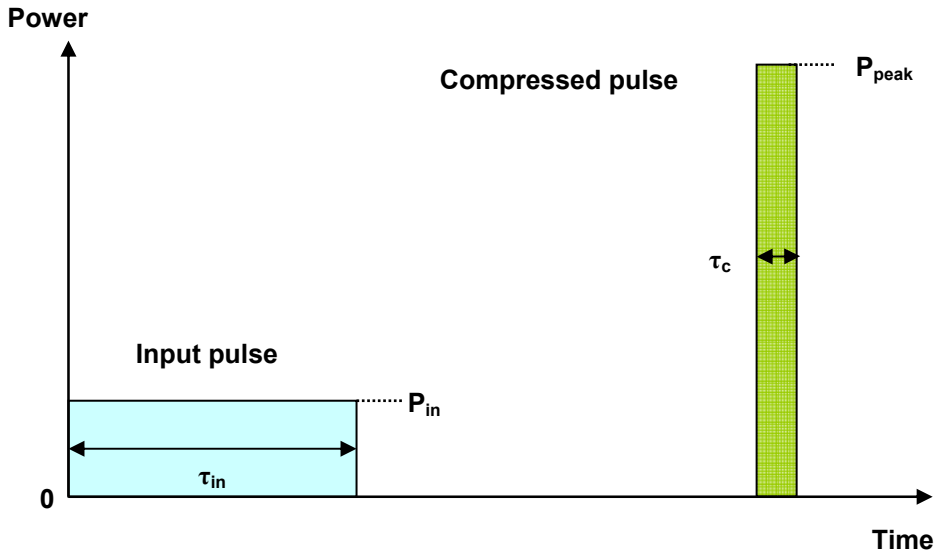

Figure 1-1 Illustration of the principle of pulse compression.

Theoretically the input pulse energy and compressed pulse energy would be equal where $P_{in}\tau_{in} = P_{peak}\tau_c$. However due to losses associated with the waveguide the energy in the compressed pulse is smaller, $E_{out} < E_{in}$. If an input pulse, which is frequency modulated Δf , were constructed as shown in Figure 1-2 then in a dispersive waveguide medium the group velocity of the electromagnetic wave propagating through it is dependent only on the frequency of the wave, $v_{gr} = v_{gr}(f)$.

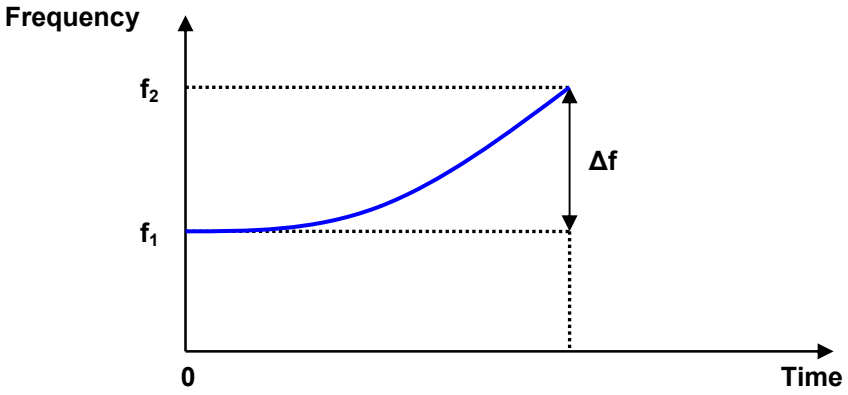

Figure 1-2 Illustration of frequency-modulation of input pulse.

Consider a microwave pulse where at time $t = 0$ the leading edge of the pulse has a lower-frequency f_1, (low-group velocity v_{gr1}) and at the tail of the pulse a higher-frequency f_2, (high-group velocity v_{gr2}) as shown in Figure 1-3. As the pulse propagates in the dispersive medium the tail of the pulse having a higher group velocity will move to over take the leading edge of the pulse resulting in a pulse shortening and a corresponding growth in amplitude if the losses are sufficiently small.

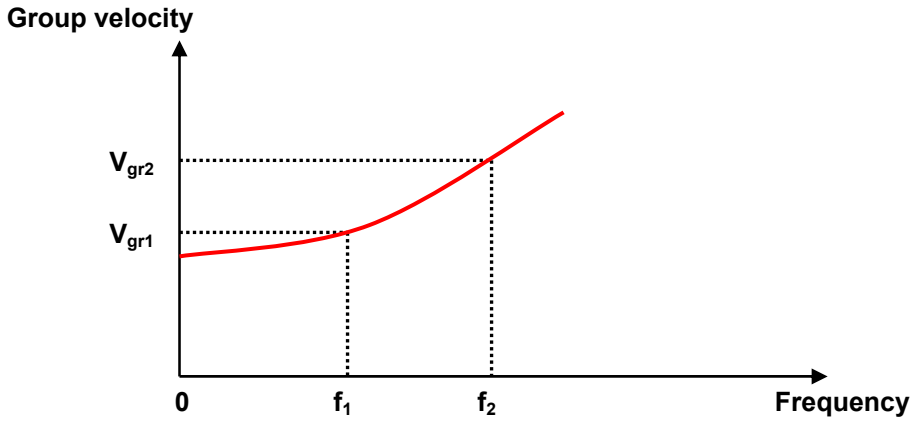

Figure 1-3 Illustration of group velocity change in a dispersive medium.

To maximise the microwave pulse compression, the length of dispersive waveguide medium has to be optimised. This length (L_{opt}) is calculated to be when the tail of the pulse approaches the leading edge of the pulse at time t^*, as shown in Figure 1-4 below,

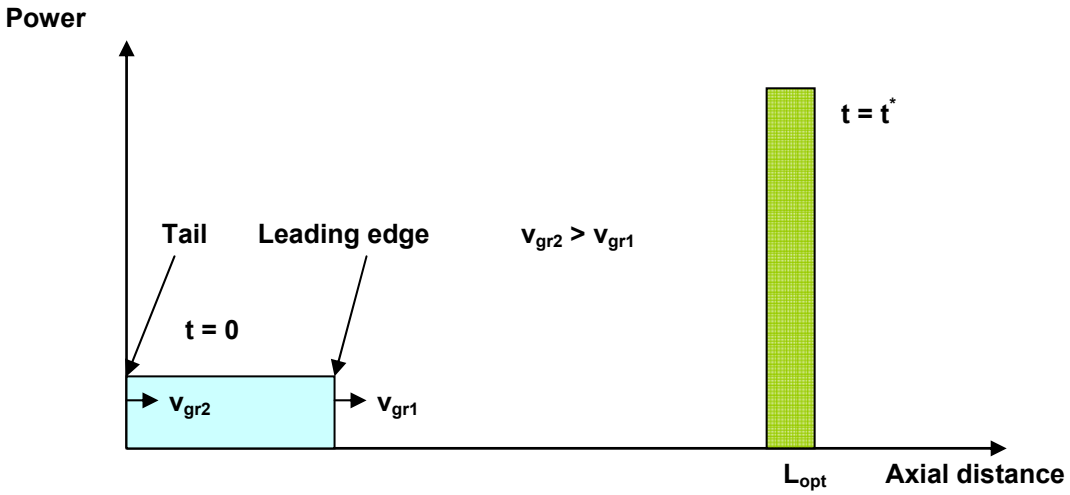

Figure 1-4 Illustration of compressed pulse in a dispersive medium.

1.4 CIRCULAR WAVEGUIDE PULSE COMPRESSOR

The circular (cylindrical) waveguide was the first type of waveguide to be investigated for use as a microwave pulse compressor where a compression factor of 10 was reported, [Bromley 1967]. The compressor operates by sweeping the frequency of an input microwave pulse from a start-frequency with a low-group velocity to a higher-frequency with a high-group velocity. As the input pulse propagates through the circular compressor the group velocity of the tail of the pulse will increase from zero to close to the speed of light and approach the leading edge of the pulse resulting in the pulse duration shortening with a corresponding growth in the pulse amplitude if the losses in the waveguide are sufficiently small.

The optimum frequency range is where the largest change in group velocity occurs. From the dispersion diagram ($\omega - k_z$) for the circular waveguide for the $TE_{1,1}$ mode, (Figure 1-5) the optimum frequency range is close to cut-off. This is a major drawback to using this particular type of compressor as operating close to cut-off has implications for the microwave amplifier source to the compressor such as a TWT in terms of unwanted feedback resulting in damage to the TWT, [Antonsen 2002].

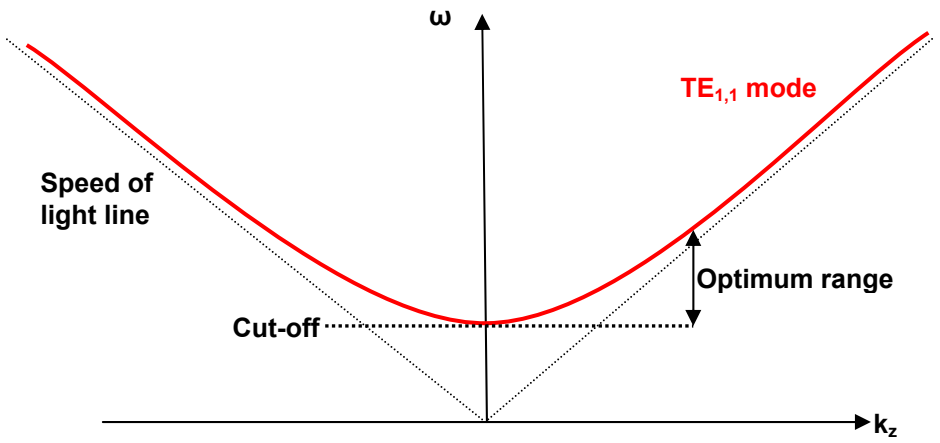

Figure 1-5 Schematic of dispersion diagram of $TE_{1,1}$ mode in circular waveguide.

1.5 HELICALLY CORRUGATED WAVEGUIDE PULSE COMPRESSOR

An alternative and attractive way of achieving microwave pulse compression is to use a helically corrugated waveguide. This waveguide is an oversized cylindrical waveguide with a helical corrugation of its inner surface which results in both an azimuthal and axial periodicity. As a result of the helical wall perturbation the rotational symmetry of the cylindrical waveguide is no longer established resulting in selective coupling between the waveguide modes, [Burt 2005, Samsonov 2004]. The dispersive properties of the helically corrugated waveguide have been used as slow wave structures in relativistic Cherenkov devices [Abubakirov 2002], mode converters [Thumm 1997, 2002] and Bragg reflectors, [Fuks 2002].

A higher, close to cut-off (mode A in Figure 1-6) and a lower (mode B in Figure 1-6) propagating circularly polarised mode can be resonantly coupled in the helically corrugated waveguide resulting in an operating eigenmode, where the dispersion characteristics of one mode gradually transform into the other, [Burt 2004, Cooke 1998]. In the optimum frequency region of their resonant coupling the eigenmode has a strongly frequency dependent group velocity which is attractive for the pulse compression as this optimum region is far from cut-off. This means the helically corrugated waveguide compressor system can be used for increasing the power from powerful non-resonant electron devices such as relativistic BWOs [Gunin 1998] and TWTs [Gilmour 1994], up to extremely high power levels.

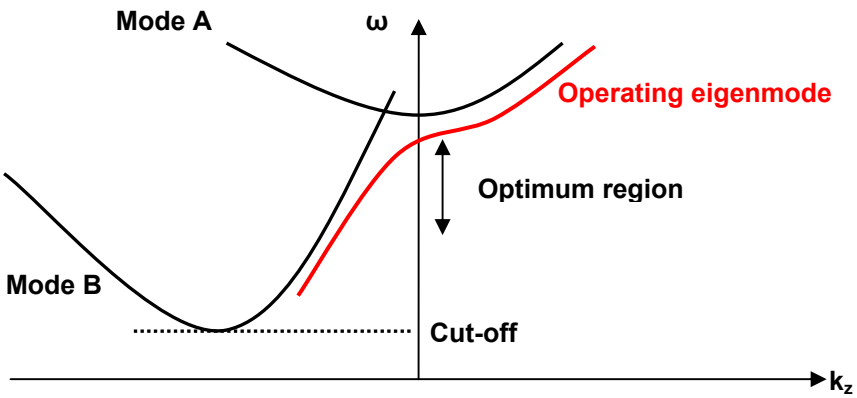

Figure 1-6 Schematic of dispersion diagram of helically corrugated waveguide showing operating eigenmode.

1.6 PREVIOUS RESEARCH

Previous research has been carried out on X-band sweep-frequency microwave pulse compression at the University of Strathclyde. Using a solid state microwave oscillator in conjunction with a 2 m length of 3-fold helically corrugated waveguide a 70 ns, 1 kW input pulse from a conventional travelling-wave tube was compressed and had a peak power of 10.9 kW and duration of 3 ns, [Burt 2004, 2005].

Furthermore, helically corrugated waveguides have been successfully used as interaction regions in gyro-TWTs [Bratman 2000, 2007, Cooke 1998, Cross 2007, Denisov 1998] and gyro-BWOs [He 2005, 2006, Samsonov 2004].

1.7 RESEARCH PURSUED IN THIS THESIS

The research work presented in this thesis examines the use of two types of oversized circular waveguides with helical corrugations of their inner surfaces. Firstly, the dispersion characteristics of the 3-fold helically corrugated waveguide were determined and from this analysis the findings were used in sweep-frequency based microwave pulse compression experiments using an optimised input pulse formed using an arbitrary waveform generator (AWG) and vector signal generator (VSG). Secondly a complete design, manufacture and experimental test of a 5-fold helically corrugated waveguide pulse compressor system was investigated for sweep-frequency based microwave pulse compression at low (mW) and medium (kW) powers. A summary of the main findings presented in this thesis are given immediately below,

i. The eigenwave dispersion of a 3-fold helically corrugated waveguide was established using three independent methods. Firstly, analytically, using a Matlab program based on coupled wave theory, secondly, numerically, using a dedicated eigenmode solver within CST Microwave studio (CST MWS) and thirdly, experimentally, using an Anritsu vector network analyzer (VNA).

ii. The power compression factor for the 3-fold compressor was calculated using a Matlab program.

iii. The ohmic losses of the 3-fold helically corrugated waveguide microwave pulse compressor were measured.

iv. An input pulse was created using an Agilent arbitrary waveform generator (AWG) and an Agilent vector signal generator (VSG). Using the 3-fold helically corrugated waveguide compressor sweep-frequency based microwave pulse compression experiments were performed in the RF laboratory at both low (mW) and medium powers (kW). The input and output pulses were measured using a 12 GHz Tektronix digital storage oscilloscope (DSO). From the microwave pulse measurements the peak power compression ratio and compression efficiency were calculated.

v. The 5-fold helically corrugated waveguide eigenwave dispersion characteristics were determined from analysis using analytical (coupled wave theory), numerical (CST MWS) and experimental (VNA) methods.

vi. The power compression factor for the 5-fold compressor was calculated using a Matlab program.

vii. The 5-fold helically corrugated waveguide compressor was designed, manufactured and constructed.

viii. The ohmic losses of the 5-fold helically corrugated waveguide microwave pulse compressor were measured.

ix. The 5-fold helically corrugated waveguide sweep-frequency-based microwave pulse compression experiments were performed both at mW and kW power levels to establish the peak power compression ratio and compression efficiency.

Chapter 2

Electromagnetism and Waveguide Theory

The chapter begins by reviewing classical electromagnetism by way of an overview of Maxwell's equations for electromagnetic fields in free-space including the wave equations for the electric and magnetic fields. The physics of waveguides are discussed for the rectangular, circular and helical geometries. Details of waveguide modes, dispersion properties, losses and power flow within waveguide are given. To complete the chapter the physics of pulse compression is presented.

2.1 CLASSICAL ELECTROMAGNETISM

James Clerk Maxwell (1831-1879) was a Scottish theoretical physicist and mathematician. Maxwell published a paper describing the behaviour of the electromagnetic field, [Maxwell 1865]. Maxwell's theory resulted in a set of four equations which are known as the Maxwell's equations and are four of the most influential equations in all of science. In Maxwell's equations there are two kinds of electric field: the electrostatic field produced by electric charge and the induced electric field produced by the changing magnetic field, [Benson 1996]. Maxwell's equations in free space in their differential form are shown below in equations 2-1 to 2-4, [Fleisch 2009].

$$\underline{\nabla} \circ \underline{E} = \frac{\rho}{\varepsilon_0}$$

Equation 2-1 Gauss's Law for electric fields

$$\underline{\nabla} \circ \underline{B} = 0$$

Equation 2-2 Gauss's Law for magnetic fields

$$\underline{\nabla} \times \underline{E} = -\frac{\partial \underline{B}}{\partial t}$$

Equation 2-3 Faraday's Law

$$\underline{\nabla} \times \underline{B} = \mu_0 \left(\underline{J} + \varepsilon_0 \frac{\partial \underline{E}}{\partial t} \right)$$

Equation 2-4 Ampere-Maxwell Law

where $\underline{E}$ is the electric field strength (Vm^{-1}), ρ is the charge density (Cm^{-3}), ε_0 is the electric permittivity of free space ($\varepsilon_0 = 8.854 \times 10^{-12}$ Fm^{-1}), $\underline{B}$ is magnetic flux density (T), μ_0 is the magnetic permeability of free space ($\mu_0 = 4\pi \times 10^{-7}$ Hm^{-1}), $\underline{J}$ is the current density vector (Am^{-2}) and t is the time (s). From Maxwell's equations in their differential form and applying vector operator identities [Spiegel 1959] the wave equation can be deduced. The wave equation is a linear, second-order, homogenous partial differential equation (PDE) that describes an electric or magnetic field that travels from one point in space to another. The wave equation for

the electric field and magnetic field are shown below in equations 2-5 and 2-6, respectively.

$$\nabla^2 \underline{E} = \mu_0 \varepsilon_0 \frac{\partial^2 \underline{E}}{\partial t^2}$$

Equation 2-5 Wave equation for electric field

$$\nabla^2 \underline{B} = \mu_0 \varepsilon_0 \frac{\partial^2 \underline{B}}{\partial t^2}$$

Equation 2-6 Wave equation for magnetic field

The general mathematical form of a wave equation can be given by,

$$\nabla^2 \underline{\Gamma} = \frac{1}{v^2} \frac{\partial^2 \Gamma}{\partial t^2}$$

Equation 2-7 General form of wave equation

where ∇^2 is the Laplacian, $\underline{\Gamma}$ is a function, v is the wave speed and t is time. Comparing equations 2-5 and 2-6 with equation 2-7 the electromagnetic wave speed v is calculated using,

$$\frac{1}{v^2} = \mu_0 \varepsilon_0 \Rightarrow v = \sqrt{\frac{1}{\mu_0 \varepsilon_0}}$$

Equation 2-8 Speed of propagation of wave

Inserting $\mu_0 = 4\pi \times 10^{-7}\ \mathrm{Hm^{-1}}$ and $\varepsilon_0 = 8.854 \times 10^{-12}\ \mathrm{Fm^{-1}}$ into equation 2-8 the speed of propagation of the wave is $v \cong 3.0 \times 10^8\ \mathrm{ms^{-1}}$. In free-space the electromagnetic waves travel at the speed of light, (c).

Maxwell's equations (equations 2-1 to 2-4) apply to electric and magnetic fields in free-space. For a review of Maxwell's equations inside matter the reader is directed to Appendix B.

2.2 WAVEGUIDES

To efficiently contain and transport electromagnetic waves from one point to another a waveguide can be used. The first waveguide was proposed by J.J. Thomson in 1893 and experimentally verified in 1894 by Oliver Lodge. Waveguide is a highly conducting hollow metal conductor whose cross-section is of a simple and constant shape. The walls of the waveguide reflect the waves to-and-fro, and the reflected waves combine in such a way as to add up to a wave that is propagated along the length of the waveguide with very little attenuation, [Grant 2004, Lorrain 1985].

Electromagnetic waves travelling within a waveguide can have many possible field configurations, each of which has either a magnetic or an electric field component in the direction of propagation. There are two possible sets of waves that can propagate in the hollow waveguide. When the electric field is perpendicular to the direction of propagation and a component of the magnetic field is in the direction of propagation these are known as transverse electric (TE) waves. Conversely, when the magnetic field is perpendicular to the direction of propagation and a component of the electric field is in the direction of propagation these are known as transverse magnetic (TM) waves, [Vanderlinde 2003]. Transverse electromagnetic (TEM) modes have no component of electric field or magnetic field in the axial direction. TEM modes cannot propagate in hollow waveguide because of the boundary conditions associated with the fields within the waveguide structure. The boundary conditions stipulate that the tangential component of the electric field at the walls is zero, i.e. $\underline{E}_{//} = 0$ thus the electric field is normal to the surface. In the case of the magnetic field the normal component of the magnetic field at the walls is zero, i.e. $\underline{B}_{\perp} = 0$.

The different electromagnetic field configurations that can be supported in waveguide are called modes and are designated by $TE_{m,n}$ or $TM_{m,n}$ where m = 0,1,2,…, and n = 0,1,2,… The integer ‘m’, gives the number of half-wave variations of the transverse field in the x-direction, and the integer ‘n’, gives the number of half-wave variations in the y-direction of a rectangular waveguide. For a circular wave guide ‘m’ gives the number of full wave variations of the radial electric field in

the azimuthal direction and ‘n’ gives the number of half-wave variations of the azimuthal electric field in the radial direction.

A hollow waveguide supports electromagnetic waves above a certain minimum frequency known as the cut-off frequency (f_c). Each of the $TE_{m,n}$ and $TM_{m,n}$ modes has a specific cut-off frequency. At a given operating frequency f , only those modes having $f > f_c$ will propagate; modes with $f < f_c$ will lead to an imaginary axial wave number k_z , ensuring that all field components will decay exponentially away from the source of excitation as it enters into the waveguide. These are referred to as evanescent modes.

A TE mode with the lowest cut-off frequency is termed the dominant mode. For a rectangular waveguide this is the $TE_{1,0}$ mode and for the circular waveguide this is the $TE_{1,1}$ mode. The reader is directed to Appendix C for examples of waveguide mode plots for the rectangular and circular waveguide, [Thumm 1997].

As the electromagnetic wave propagates along the waveguide there is small energy losses at each reflection due to currents induced in the walls by the transmitted electromagnetic fields; these losses are referred to as ohmic losses. As the frequency increases the current tends to flow near the surface of the conductor where the energy does not penetrate the metal to any significant depth resulting in increased (I^2R) losses, [Thomas 1972].

2.3 RECTANGULAR WAVEGUIDE THEORY

The rectangular waveguide is a hollow metal pipe of rectangular cross-section with width 'a', in the x-direction and height 'b', in the y-direction. The direction of propagation of the electromagnetic waves is in the z-direction, [Collin 2001, Dobbs 1985, Phelps 1997]. Cartesian coordinates (x, y, z) are used for the geometry of the rectangular waveguide as shown in Figure 2-1 below,

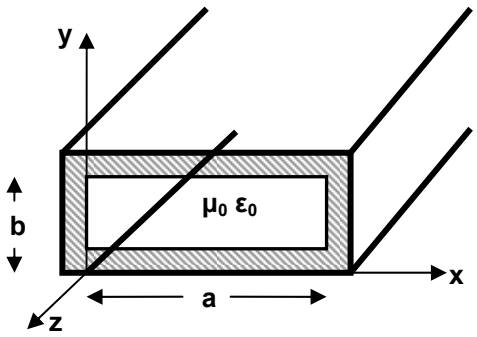

Figure 2-1 Schematic of rectangular waveguide geometry.

In free-space (absence of matter) the dispersion relation of an electromagnetic wave is given by,

$$\omega = ck \qquad \textbf{Equation 2-9}$$

where c, is the speed of the electromagnetic wave in free-space and k, is the wave number in free-space where,

$$k = 2\pi/\lambda \qquad \textbf{Equation 2-10}$$

Resolving k into it's transverse (k_x, k_y) and axial (k_z) components,

$$k = \sqrt{k_x^2 + k_y^2 + k_z^2} = \sqrt{k_\perp^2 + k_z^2} \qquad \textbf{Equation 2-11}$$

Substituting equation 2-11 into equation 2-9 for k,

$$\omega = c\sqrt{k_\perp^2 + k_z^2} \qquad \textbf{Equation 2-12}$$

The minimum frequency for propagation of an electromagnetic wave is ω_c, where,

$$\omega_c = ck_\perp \qquad \textbf{Equation 2-13}$$

and $k_\perp$ is the cut-off wave number and is given by,

$$k_\perp = \sqrt{\left(\frac{m\pi}{a}\right)^2 + \left(\frac{n\pi}{b}\right)^2} \qquad \textbf{Equation 2-14}$$

where 'm'and 'n'are the waveguide mode numbers i.e. the mode $TE_{1,0}$ has $m = 1$ and $n = 0$ which means there is one half wavelength variation across the width of the rectangular waveguide and no variation across the height of the waveguide. Substituting equation 2-14 into equation 2-12 for $k_\perp$,

$$\omega = c\sqrt{\left(\frac{m\pi}{a}\right)^2 + \left(\frac{n\pi}{b}\right)^2 + k_z^2} \qquad \textbf{Equation 2-15}$$

The wavelength of the electromagnetic wave inside the waveguide is different to that of the free-space wavelength and is known as the waveguide wavelength (λ_g). This wavelength is defined as the distance between two equal phase planes along the waveguide (Figure 2-2) and is given by,

$$\lambda_g = \frac{\lambda}{\cos\theta} \qquad \textbf{Equation 2-16}$$

The waveguide wavelength (λ_g) , is always greater than the free-space wavelength, (λ).

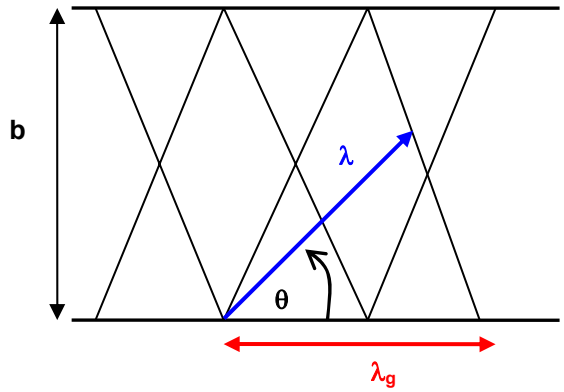

Figure 2-2 Schematic of electromagnetic wave propagating in rectangular waveguide.

The waveguide wavenumber, k_g is given by,

$$k_g = \frac{2\pi}{\lambda_g} \qquad \textbf{Equation 2-17}$$

As the electromagnetic wave propagates through the waveguide the electric field is in the y-direction only and has a maximum intensity at the mid-plane of the waveguide ($x = a/2$), [Feynman 1977]. The electric field must go to zero at the sides parallel to the y-axis due to boundary conditions because the currents and charges in a conductor always adjust themselves so that there is no tangential component of the electric field at the surface of a conductor ($E_{//} = 0$), resulting in the maximum electric field being located at the centre of the guide. The electric field E_y varies as an arch across the waveguide as shown in Figure 2-3 below.

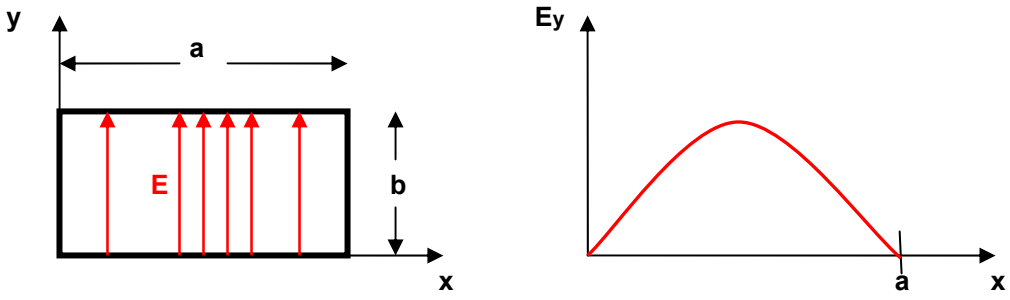

Figure 2-3 The electric field in the rectangular waveguide at some value z.

As the electromagnetic waves propagate inside the waveguide the field will alternate between positive and negative values along the z direction and the oscillations will

travel along the waveguide with some velocity v as shown in Figure 2-4. The oscillations will have an angular frequency ω, the variation will be $e^{i(k_z z-\omega t)}$. This results in the wave taking the form of equation 2-18.

$$E_y = E_0 \sin k_x x e^{i(k_z z-\omega t)} \qquad \textbf{Equation 2-18}$$

The equation for E_y satisfies the boundary conditions imposed by the waveguide structure; that the electric field should have no tangential components at the walls, $\underline{E}_{//} = 0$; the field is perpendicular to the top and bottom faces and its zero at the two side faces of the waveguide.

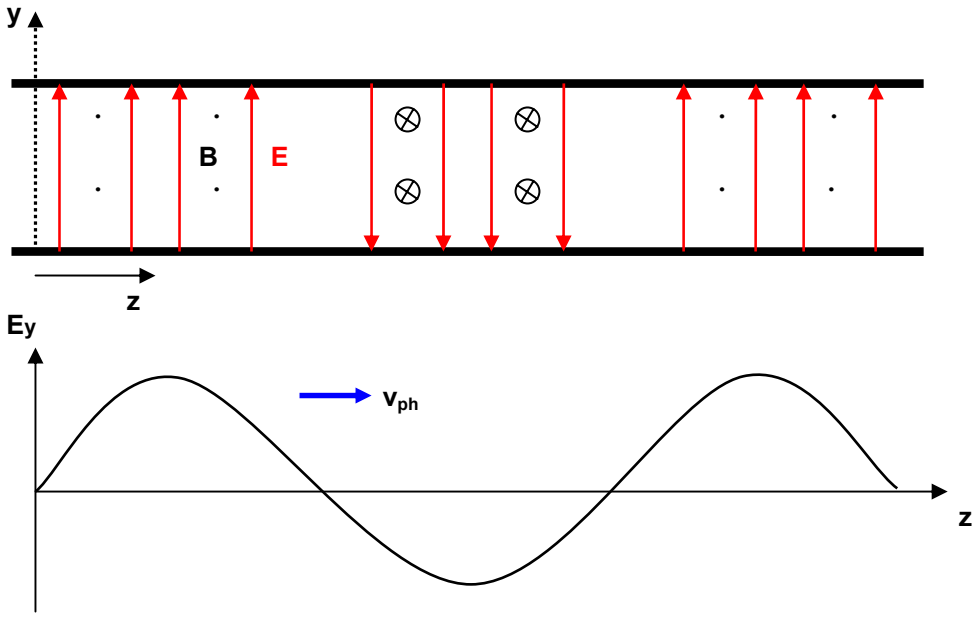

Figure 2-4 The z-dependence of the field in the rectangular waveguide; E is the electric field (red arrows) and B is the magnetic field (black dots and crosses).

k_x is chosen so that one-half wave variation of $\sin k_x x$ just fits in the width of the guide then $k_x a = \pi$. The divergence of the electric field must be zero in the free space inside the waveguide, since there are no charges in the waveguide ($\underline{\nabla} \circ \underline{E} = 0$).

The electromagnetic field distribution equations for rectangular waveguide are defined [Benford 2007, Phelps 1997] as follows,

TE modes

$$B_x = i\frac{k_z}{k_\perp^2}\frac{\partial B_z}{\partial x}$$ **Equation 2-19**

$$B_y = i\frac{k_z}{k_\perp^2}\frac{\partial B_z}{\partial y}$$ **Equation 2-20**

$$E_x = i\frac{\omega}{k_\perp^2}\frac{\partial B_z}{\partial y}$$ **Equation 2-21**

$$E_y = -i\frac{\omega}{k_\perp^2}\frac{\partial B_z}{\partial x}$$ **Equation 2-22**

TM modes

$$B_x = -i\frac{\omega}{\omega_c^2}\frac{\partial E_z}{\partial y}$$ **Equation 2-23**

$$B_y = i\frac{\omega}{\omega_c^2}\frac{\partial E_z}{\partial x}$$ **Equation 2-24**

$$E_x = i\frac{k_z}{k_\perp^2}\frac{\partial E_z}{\partial x}$$ **Equation 2-25**

$$E_y = -i\frac{k_z}{k_\perp^2}\frac{\partial E_z}{\partial y}$$ **Equation 2-26**

The above components in equations 2-19 thru 2-26 can be found for the TE and TM fields using equations 2-27 and 2-28 which satisfy the boundary conditions for the rectangular waveguide.

$$E_z = A\sin\left(\frac{m\pi}{a}x\right)\sin\left(\frac{n\pi}{b}y\right)e^{i(k_z z-\omega t)}$$ **Equation 2-27**

$$B_z = D\cos\left(\frac{m\pi}{a}x\right)\cos\left(\frac{n\pi}{b}y\right)e^{i(k_z z-\omega t)} \qquad \textbf{Equation 2-28}$$

where A and D are amplitude constants

The electric and magnetic field are related by the equation $\underline{\nabla} \times \underline{B} = \frac{1}{c^2}\frac{\partial \underline{E}}{dt}$. The lines of magnetic field $\underline{B}$ circulate around the regions in which $\partial \underline{E}/\partial t$ is largest, that is, half way between the maximum and minimum of the electric field $\underline{E}$. The magnetic loops of $\underline{B}$ lie parallel to the plane and between the crest and troughs of the electric field $\underline{E}$. This satisfies the boundary conditions where a magnetic field cannot be perpendicular to a conductor. The electric and magnetic field lines are shown in Figure 2-5 below.

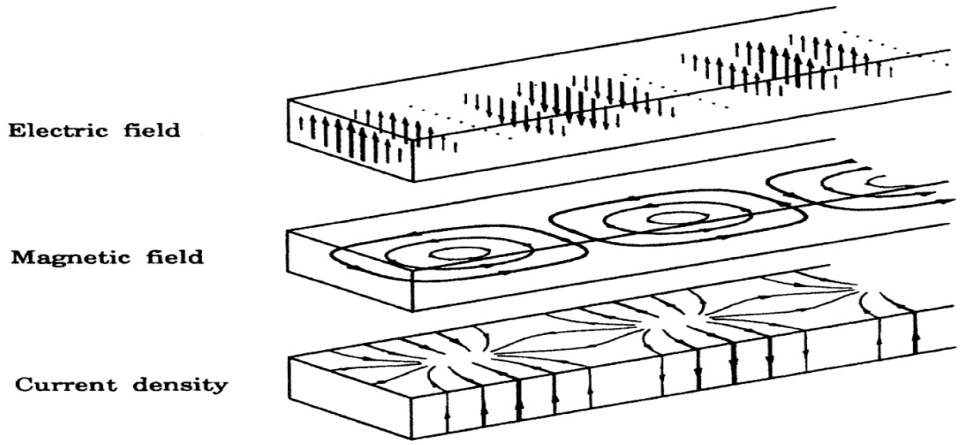

Figure 2-5 Electric, magnetic and current field patterns of the $TE_{1,0}$ mode of a rectangular waveguide, [Dobbs 1985].

2.4 CIRCULAR WAVEGUIDE THEORY

The circular waveguide is a hollow metal tube of circular cross section. Cylindrical co-ordinates, $(\mathrm{r}, \phi, \mathrm{z})$ are used to define the geometry of the waveguide. A schematic of the circular waveguide is shown in Figure 2-6. To solve Maxwell's equations and the wave equations in cylindrical coordinates Bessel functions are required, [Pozar 1998].

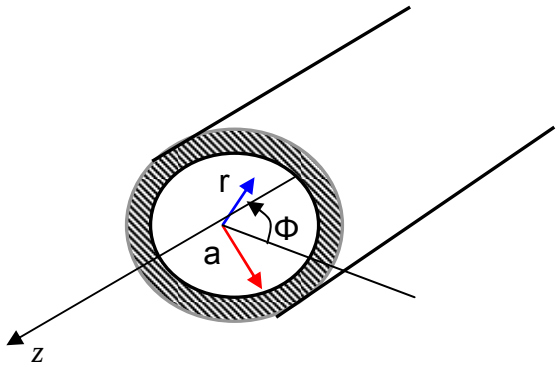

Figure 2-6 Schematic of circular waveguide where 'a' is radius of the waveguide.

The general wave equation for cylindrical waveguide is given by,

$$\left(\nabla_t^2 + \varepsilon\mu\omega^2 - k_z^2\right)\begin{bmatrix}\underline{E}\\ \underline{B}\end{bmatrix} = 0 \qquad \textbf{Equation 2-29}$$

Where the transverse gradient operator, ∇_t is given by,

$$\nabla_t^2 = \nabla^2 - \frac{\partial^2}{\partial z^2} \qquad \textbf{Equation 2-30}$$

The transverse Laplacian, ∇_t^2 in cylindrical co-ordinates gives,

$$\left[\frac{1}{r}\cdot\frac{\partial}{\partial r}\left(r\frac{\partial}{\partial r}\right) + \frac{1}{r^2}\cdot\frac{\partial^2}{\partial \phi^2} + \varepsilon\mu\omega^2 - k_z^2\right]\psi = 0 \qquad \textbf{Equation 2-31}$$

where r is the radial co-ordinate, ϕ is the azimuthal co-ordinate and ψ represents E_z for TM modes and B_z for TE modes. The solution of equation 2-31 has the form

$$\psi = [AJ_m(k_t r) + BY_m(k_t r)][C\cos m\phi + D\sin m\phi] \qquad \textbf{Equation 2-32}$$

Where $J_m(\nu)$ and $Y_m(\nu)$ are Bessel functions of the first and second kind respectively. By applying the appropriate boundary conditions (B = 0 in equation 2-32), and where 'm' is an integer the solution is given by,

$$\psi = AJ_m(k_t r)e^{\pm im\phi} \qquad \textbf{Equation 2-33}$$

TM modes

For the $TM_{m,n}$ modes, the boundary conditions at the waveguide surface (r = a) require that $E_{//} = 0$ which results in the following equation,

$$J_m(k_t a) = 0 \qquad \textbf{Equation 2-34}$$

Where $k_t a$ is a root of J_m. This occurs a number of times n =1,2,3,…Letting ζ_{mn} be the n^{th} zero of $J_m(k_t a) = 0$, the $TM_{m,n}$ modes are specified by values of m and n, such that

$$\zeta_{mn} = k_t a \qquad \textbf{Equation 2-35}$$

Cut-off frequencies are given by,

$$f_c = \frac{\zeta_{mn}}{2\pi a\sqrt{\mu\varepsilon}} \qquad \textbf{Equation 2-36}$$

where μ is the permeability and ε is the permittivity of the material filling the guide.

Values of ζ_{mn} for some $TM_{m,n}$ modes are given in Table 2-1 below.

n \ m	0	1	2	3	4
1	2.405	3.832	5.136	6.380	7.588
2	5.520	7.106	8.417	9.761	11.065
3	8.653	10.173	11.620	13.015	14.372
4	11.795	13.324	14.796	16.223	17.616

Table 2-1 Zeros for Bessel functions of the first kind $J_m(\nu) = 0$ for TM modes.

The lowest order mode for the TM modes is the $TM_{0,1}$ where $\zeta_{01} = 2.405$ from Table 2-1

TE modes

For the TE modes $E_z = 0$ and $\partial B_z / \partial r = 0$ at $r = a$, the boundary conditions are satisfied for

$$J_m'(k_t a) = 0 \qquad \textbf{Equation 2-37}$$

where J_m' is the derivative of the Bessel function with respect to r. Let ζ_{mn}' be the n[th] root of $J_m'(k_t a) = 0$ .The TE modes are specified by,

$$\zeta_{mn}' = k_t\, a \qquad \textbf{Equation 2-38}$$

Table 2-2 gives values of ζ_{mn}' for some of the TE modes. The cut-off frequencies are given by,

$$f_c(TE_{mn}) = \frac{\zeta_{mn}'}{2\pi a\sqrt{\mu\varepsilon}} \qquad \textbf{Equation 2-39}$$

n \ m	0	1	2	3	4
1	3.832	1.841	3.054	4.201	5.318
2	7.016	5.331	6.706	8.015	9.282
3	12.173	8.536	9.969	11.346	12.682
4	13.324	11.706	13.170	14.586	15.964

Table 2-2 Zeros for derivatives of Bessel functions of the first kind $dJ_m(\nu)/d\nu$ for TE modes.

The lowest order mode for a circular waveguide is the $TE_{1,1}$ mode where $\zeta_{1,1}' = 1.841$ from Table 2-2.

The electromagnetic field distributions in the circular waveguide are found by solving equation 2-31 and applying the boundary conditions. The solutions of the equation give the electromagnetic field distributions for the TE and TM modes and are shown below [Phelps 1997],

TE modes

$$E_r = -\frac{m\omega}{k_c^2 r} B_z$$ **Equation 2-40**

$$E_\phi = -i\frac{\omega}{k_c^2}\frac{\partial B_z}{\partial r}$$ **Equation 2-41**

$$B_r = i\frac{k_z}{k_c^2}\frac{\partial B_z}{\partial r}$$ **Equation 2-42**

$$B_\phi = -\frac{mk_z}{k_c^2 r} B_z$$ **Equation 2-43**

TM modes

$$E_r = i\frac{k_z}{k_c^2}\frac{\partial E_z}{\partial r}$$ **Equation 2-44**

$$E_\phi = -\frac{mk_z}{k_c^2 r} E_z$$ **Equation 2-45**

$$B_r = \frac{m\omega}{\omega_c^2 r} E_z$$ **Equation 2-46**

$$B_\phi = i\frac{\omega}{\omega_c^2}\frac{\partial E_z}{\partial r}$$ **Equation 2-47**

Where

$$E_z = AJ_m\left(k_c r\right)e^{i(m\phi + k_z z - \omega t)}$$ **Equation 2-48**

$$B_z = DJ_m\left(k_c r\right)e^{i(m\phi + k_z z - \omega t)}$$ **Equation 2-49**

and A and D are amplitude constants.

2.5 ELECTROMAGNETIC WAVE VELOCITY

The speed of an electromagnetic wave can be determined from the dispersion relationship, [Feynman 1977, Grant 2004]. The dispersion relationship relates to the angular frequency ω and axial wavenumber k_z and is given by,

$$\omega^2 = \omega_c^2 + c^2 k_z^2 = \omega_c^2 + \frac{k_z^2}{\mu\varepsilon} \qquad \textbf{Equation 2-50}$$

The dispersion curve for a circular waveguide is shown below in Figure 2-7.

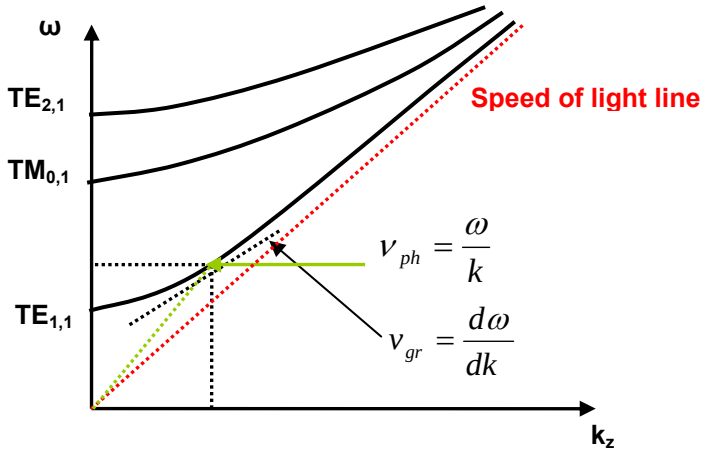

Figure 2-7 Schematic of dispersion diagram for modes in circular waveguide showing phase velocity (v_{ph}) and group velocity (v_{gr}).

Phase velocity

The phase velocity (v_{ph}) of the wave is the rate at which the phase of the wave propagates. This is the speed at which the phase of any one frequency component of the wave travels. The phase velocity is given by,

$$v_{ph} = \frac{\omega}{k} \qquad \textbf{Equation 2-51}$$

or alternatively by,

$$v_{ph} = \frac{c}{\sqrt{1-\left(\frac{\omega_c}{\omega}\right)^2}}$$ **Equation 2-52**

For frequencies above cut-off then ω_c/ω is less than one and v_{ph} is real and greater than the speed of light. This is entirely possible because it is the nodes of the wave which are travelling and not the energy or information.

Group velocity

The energy in the group of waves travels with the group velocity, (v_{gr}). This depends on the dispersion of the different frequencies in the group, i.e. on the variation of the speed of the waves with frequency. The group velocity is given by,

$$v_{gr} = \frac{d\omega}{dk}$$ **Equation 2-53**

or alternatively,

$$v_{gr} = c\sqrt{1-\left(\frac{\omega_c}{\omega}\right)^2}$$ **Equation 2-54**

The geometric mean of the phase velocity and the group velocity is the speed of light c, given by,

$$v_{ph} \cdot v_{gr} = c^2$$ **Equation 2-55**

2.6 POWER DENSITY OF ELECTROMAGNETIC WAVE

An electromagnetic wave will propagate along the waveguide with an energy flow where the electric and magnetic fields are transverse and orthogonal to the direction of wave propagation, [Grant 2004]. The energy in the electric field is given by,

$$u_e = \frac{1}{2}\varepsilon_0 E^2 \qquad \textbf{Equation 2-56}$$

The energy within the magnetic field is given by,

$$u_m = \frac{B^2}{2\mu_0} \qquad \textbf{Equation 2-57}$$

The total electromagnetic energy density is the sum of the electric and magnetic field contributions, u_e and u_m

$$u_{tot} = u_e + u_m = \frac{1}{2}\left[\varepsilon_0 E^2 + \frac{B^2}{\mu_0}\right] \qquad \textbf{Equation 2-58}$$

Power density is defined as the power carried by an electromagnetic wave and is equal to the electric field $\underline{E}$ vector multiplied with the magnetic field $\underline{H}$ [Scott 2005] and is known as the Poynting vector $\underline{S}$ as shown in equation 2-59.

$$\underline{S} = \left(\underline{E} \times \underline{H}\right) \qquad \textbf{Equation 2-59}$$

where $\underline{H} = \underline{B}/\mu_0$.

The time-averaged Poynting vector is given by,

$$\underline{S}_{av} = \frac{1}{2}\mathrm{Re}\left(\underline{E} \times \underline{H}^*\right) \qquad \textbf{Equation 2-60}$$

where $\underline{H}^*$ is the complex conjugate

Integrating the Poynting vector across a cross section of the waveguide gives the total power flowing out the cross section as follows,

$$P = \int_S \left(\underline{E} \times \underline{H}\right) \cdot dA \qquad \textbf{Equation 2-61}$$

2.7 WAVEGUIDE LOSSES

As an electromagnetic wave propagates through the waveguide there will be a continuous loss of power due to ohmic losses on the inner waveguide walls, [Lorrain 1985]. At an atomic level some of the electrons within the waveguide metal have no binding force holding them to a particular atom. These 'free' electrons are responsible for the conductivity of a metal. Electromagnetic waves impinging a waveguide conductor will produce a current in the walls of the waveguide. The skin depth (δ) is a measure of the depth at which the current density falls to 1/e of its value near the surface and is given by,

$$\delta = \sqrt{\frac{2}{\omega\sigma\mu}} \qquad \textbf{Equation 2-62}$$

where ω is the angular frequency of the wave and σ is the electrical conductivity of the metal. For example at a frequency of 10 GHz the skin depth of copper is around 0.65 μm which is very small thus most of the current flows in an extremely thin region near the surface.

The losses associated with the transportation of an electromagnetic wave in a waveguide are dependent on the following:

i. cross-sectional area
ii. length of the waveguide structure
iii. group velocity of the electromagnetic wave
iv. ratio of the operating frequency to the cut-off frequency of the waveguide
v. waveguide conductivity

Any additional losses within the waveguide structure would be minimal and could be attributed to waveguide leakage and negligible radiation losses to free space.

2.8 HELICALLY CORRUGATED WAVEGUIDE THEORY

The helically corrugated waveguide profile is represented in a cylindrical coordinate system (r, ϕ, z) by,

$$r(\phi, z) = r_0 + l\cos(m_B\phi + k_B z) \qquad \textbf{Equation 2-63}$$

where r_0 is the mean radius of the waveguide, l is the corrugation amplitude, m_B is the azimuthal number of the Bragg periodicity vector and k_B is the axial component of the Bragg periodicity vector where k_B is defined as,

$$k_B = \frac{2\pi}{d} \qquad \textbf{Equation 2-64}$$

where d is the corrugation period.

In a periodically corrugated waveguide the electromagnetic field can be represented as a superposition of the spatial harmonics, which, at negligibly small corrugation amplitude, as in the case of the helically corrugated waveguide, possess dispersion characteristics of the smooth cylindrical waveguide modes shifted along the axial-wavenumber axis, k_z, by an integer number of the Bragg periodicity vector k_B.

Resonant coupling between the circularly polarised modes occurs when their axial and azimuthal wavenumber satisfy the Bragg conditions which are given by,

$$m_B = m_1 - m_2; \quad k_B = k_{z1} - k_{z2} \qquad \textbf{Equation 2-65}$$

where m_1 and m_2 are the azimuthal numbers and k_{z1} and k_{z2} are the axial wave numbers. This coupling results in the appearance of eigenwaves whose dispersions can be represented as splitting of the partial mode dispersions near the frequencies of their intersections with dispersions of the spatial harmonics, [Burt 2004, 2005]. The 3-fold helically corrugated waveguide used in the compression experiments had a

right-handed helical corrugation where $m_B = -3$, the structure resonantly coupled in the lowest frequency region a forward propagating left-circularly polarised $TE_{-1,1}$ mode $(m_1 = -1)$ and a near cut-off right-circularly polarised $TE_{2,1}$ mode $(m_2 = 2)$.

The 5-fold helically corrugated waveguide structure was represented in the same manner as that for the 3-fold case by using equation 2-63. In the case of the 5-fold helically corrugated waveguide the azimuthal number of the Bragg periodicity vector is five, $m_B = -5$. The 5-fold helically corrugated waveguide resonantly coupled a forward propagating counter-rotating right-circularly polarised $TE_{-3,1}$ mode $(m_1 = -3)$ and a near cut-off co-rotating left-circularly polarised $TE_{2,2}$ mode $(m_2 = 2)$, resulting in the appearance of eigenwaves.

When the corrugation amplitude l is small compared to the wavelength, the modes of the helically corrugated waveguide can be found using the method of perturbation and the coupled-mode theory leading to the eigenmode dispersion equation, [Burt 2004].

$$\left(k^2 - k_z^2 - k_{\perp 1}^2\right)\left(k^2 - \left(k_z - k_B\right)^2 - k_{\perp 2}^2\right) = 4\kappa^2 k_0^4 \qquad \textbf{Equation 2-66}$$

where κ is the coupling coefficient and is given by,

$$\kappa = \frac{l}{2r_0^3 k_0^2} \frac{S_1^2 S_2^2 - m_1 m_2 r_0^2 \left(k_0^2 + k_{z1} k_{z2}\right)}{\sqrt{\left(S_1^2 - m_1^2\right)\left(S_2^2 - m_2^2\right)}} \qquad \textbf{Equation 2-67}$$

and κ is normalised to the value of the wave vector k_0 of exact Bragg resonance, i.e. $k_0 = \sqrt{k_{\perp 2}^2 + k_{z1}^2}$

2.9 PHYSICS OF MICROWAVE PULSE COMPRESSION

An input pulse with pulse duration τ propagating in a waveguide will have an energy (E) given by,

$$E = \int_0^{\tau} P_{inst}.dt \qquad \textbf{Equation 2-68}$$

where P_{inst} is the instantaneous power of the input pulse, [Burt 2004]. By compressing the long duration input pulse (τ) to a much shorter pulse duration (τ_c) there will be an increase in the power of the compressed pulse due to the reduction in the pulse duration.

The time compression ratio (C_t) is the ratio of the input pulse duration to the compressed pulse duration and is given by,

$$C_t = \frac{\tau}{\tau_c} \qquad \textbf{Equation 2-69}$$

The peak power compression ratio (C_p) is the ratio of the peak values for the compressed pulse and the input pulse and is given by,

$$C_p = \frac{P_{peakc}}{P_{peak}} \qquad \textbf{Equation 2-70}$$

where P_{peakc} and P_{peak} are the values of the peak power for the compressed and input pulses respectively.

The compression efficiency (η_c) is a ratio of the energy contained in the main body of the compressed pulse (E_{out}) to the input energy (E_{in}) and is given by,

$$\eta_c = \frac{E_{out}}{E_{in}}$$ **Equation 2-71**

The actual efficiency of the system (η) is given by,

$$\eta = \frac{\int_0^{\tau_c} P_{instc}\, dt}{\int_0^{\tau} P_{inst}\, dt}$$ **Equation 2-72**

where P_{instc} is the instantaneous power of the compressed pulse.

2.10 THEORETICAL COMPRESSION OF A FREQUENCY-SWEPT PULSE

The principle of microwave pulse compression in a helically corrugated waveguide using a frequency dispersive medium relies on the leading edge of the pulse having a lower group velocity than the tail of the pulse resulting in the compression of microwave radiation and an increase in the peak power. For sweep-frequency based microwave pulse compression the frequency is swept from a start frequency (ω_1) with low group velocity (v_{gr1}) to a stop frequency (ω_2) with a higher group velocity (v_{gr2}).

Estimation and optimisation of the pulse compressor length and input pulse can be performed using a kinematic approach [Samsonov 2004]. Consider a rectangular input pulse given by $u_o(t) = A_0 \exp[-i\varphi(t)]$ where $t \in (0, \tau)$ as a train of 'particles' having different velocities and entry times according to the dependence of the group velocity on the time where $v_{gr} = (dk/d\omega)^{-1}$ and the frequency modulation of the input pulse is given by,

$$\omega(t) = \frac{d\varphi}{dt} \qquad \textbf{Equation 2-73}$$

Adopting this approach the maximum pulse compression occurs when all particles meet each other at the same distance. Therefore the inverse group velocity of a particle should be a linear function of its entry time given by,

$$\frac{1}{v_{gr}} = \frac{1}{v_1} - \left(\frac{1}{v_1} - \frac{1}{v_2}\right)\frac{t}{\tau} \qquad \textbf{Equation 2-74}$$

The meeting point distance of the particles is $L = V\tau$ where, $V = \frac{v_1 v_2}{(v_2 - v_1)}$. The corresponding pulse width at this point is zero and the minimum achievable width is approximated to,

$$\tau_{\min} \cong \frac{1}{\Delta f} \qquad \textbf{Equation 2-75}$$

where $\Delta f = \frac{|\omega_2 - \omega_1|}{2\pi}$.

In the case of a lossless medium the maximum power compression (C_p) is given by,

$$C_p = \frac{|u_{\max}|^2}{A_0^2} = \Delta f \tau \qquad \textbf{Equation 2-76}$$

In the case where the medium losses are incorporated,

$$C_p = \frac{|u_{\max}|^2}{A_0^2} = \Delta f \tau e^{(-\bar{\gamma}L)} \qquad \textbf{Equation 2-77}$$

where $\bar{\gamma}$ is the average attenuation co-efficient in the interval $[f_1, f_2]$.

Re-arranging equation 2-77 and substituting pulse width as L/V for τ the maximum compression factor as a function of length is given by,

$$C_{p\max} = \frac{\Delta f e^{-1}}{\bar{\gamma} V} \qquad \textbf{Equation 2-78}$$

at the length $L_{opt} = \frac{1}{\bar{\gamma}}$.

Chapter 3

The 3-Fold Helically Corrugated Waveguide

The chapter begins with a brief review of the design and physics of the 3-fold helically corrugated waveguide as a microwave pulse compressor at X-band frequencies. This is followed by a comprehensive dispersion analysis of the 3-fold helically corrugated waveguide using analytical (coupled wave theory), numerical (CST MWS) and experimental techniques (VNA) to establish the eigenwave and group velocity dispersion characteristics. The ohmic losses measured using the scalar network analyzer (SNA) and vector network analyzer (VNA) for the 3-fold helically corrugated waveguide compressor are reported. To conclude the chapter the calculated optimum power compression factor is given by way of a Fourier optics approach.

3.1 PHYSICS OF A 3-FOLD HELICALLY CORRUGATED WAVEGUIDE

The helically corrugated waveguide is a transformation and adaptation of a typical smooth-cylindrical waveguide by the introduction of periodic corrugations to the waveguide's inner surface. The helical profile of its inner surface is represented as $r(\phi, z) = r_0 + l\cos(m_B\phi + k_B z)$. A schematic of such a 3-fold helically corrugated waveguide is shown below in Figure 3-1,

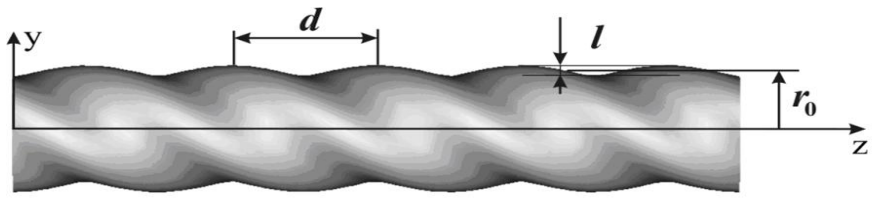

Figure 3-1 Schematic of a 3-fold helically corrugated waveguide.

where r_0 is the mean radius of the helical waveguide l is the amplitude of the corrugated grooves m_B and $k_B = 2\pi/d$ define the azimuthal and axial component of the Bragg periodicity vector $\mathrm{k_B}$, respectively and d is the corrugation period.

The dimensions of the 3-fold helically corrugated waveguide are listed in Table 3-1 below,

Waveguide parameter	Value
r_0	1.47 cm
l	0.14 cm
d	2.89 cm
m_B	-3
$k_B = 2\pi/d = 2\pi/2.89$	2.17 $\mathrm{cm^{-1}}$

Table 3-1 The 3-fold helically corrugated waveguide parameters.

The 3-fold helically corrugated waveguide was constructed in sections. Each section had a length of 23.12 cm which corresponded to 8 corrugation periods (2.89 cm) in length, (Figure 3-2). The main body of the compressor was comprised of 9 sections

(72 corrugation periods) which totalled 2.08 m. The 3-fold helically corrugated waveguide was made of copper which had an electrical conductivity of 5.88×10^{7} mho/m which made it an ideal metal for the transportation of microwave radiation, [Laverghetta 1991].

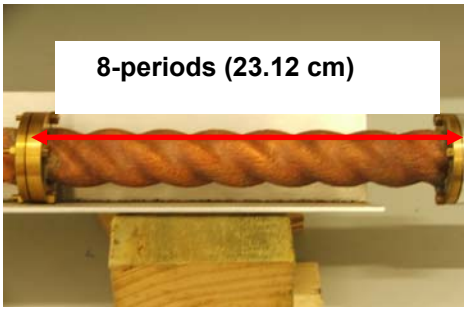

Figure 3-2 Digital photograph of a section of copper 3-fold helically corrugated waveguide.

The electromagnetic field within the waveguide can be described as a superposition of the spatial harmonics, which at very small corrugation amplitude $l << d$, the dispersion characteristics of the circular waveguide modes (partial modes) are shifted along the z axis by an integer number of k_B. At non-zero amplitude of corrugation, resonant coupling between the modes occurs when their axial and azimuthal wave numbers satisfy the Bragg conditions of equation 2-65. The azimuthal component of the Bragg periodicity vector is given by $m_B = -3$ which in the lowest frequency region resonantly coupled a near cut-off right-circularly polarised $TE_{2,1}$ mode with a forward propagating left-circularly polarised $TE_{-1,1}$ mode, resulting in the operating eigenmode (W_1) as shown in Figure 3-3 below,

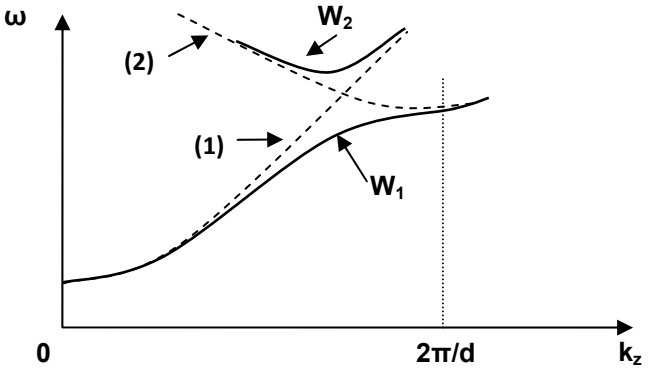

Figure 3-3 Dispersion diagram: (1) is a lower partial mode of a smooth circular waveguide, (2) is a spatial harmonic of near-cutoff mode; W_1 and W_2 are the eigenmodes of the helical waveguide.

3.2 EIGENWAVE DISPERSION CALCULATED ANALYTICALLY

The dispersion of the eigenwave can be described using a coupled-wave theory approach [Cooke 1998, Denisov 1998]. A matlab code (Appendix D) was created to solve for the dispersion equation of equation 2-66,

$$\left(k^2 - k_z^2 - k_{\perp 1}^2\right)\left(k^2 - \left(k_z - k_B\right)^2 - k_{\perp 2}^2\right) = 4\kappa^2 k_0^4$$

Expanding equation 2-66 out results in a fourth order polynomial given by,

$$k^4 - k^2\left[\left(k_z + k_B\right) + k_{\perp 2}^{\ 2} + k_{\perp 1}^{\ 2} + k_z^2\right] + \left(k_z^2 + k_{\perp 1}^{\ 2}\right)\left[k_{\perp 2}^{\ 2} + \left(k_z + k_B\right)^2 - \kappa^2\right] = 0$$

Using the Matlab code of appendix D the expanded equation was solved to find the roots of the coupling coefficient (κ). The 3-fold helically corrugated waveguide parameters were inserted into the code for the average radius, corrugation depth and period of the helically corrugated waveguide. In the matlab code mode 1 corresponded to the $TE_{2,1}$ mode and mode 2 corresponded to the $TE_{1,1}$ mode. The azimuthal and Bessel function roots were inserted into the code for the $TE_{1,1}$ and $TE_{2,1}$ modes. An extract from the code is shown immediately below

```
% Waveguide geometry
r0 = 1.47*cm;       % average radius of waveguide
r1 = 0.14*cm;       % corrugation depth of waveguide
d = 2.89*cm;        % period

% Azimuthal components of waveguide modes
m1 = 2;             % azimuthal component for TE2,1 wave
m2 = -1;            % azimuthal component for TE1,1 wave

% Roots of Bessel functions
Z1 = 3.054;         % Bessel function root for TE2,1 wave
Z2 = 1.841;         % Bessel function root for TE1,1 wave
```

The cut-off wave number for mode 1, the $TE_{2,1}$ mode, is calculated as

$$k_{\perp 1} = \frac{3.054}{1.47} = 2.08 \text{ cm}^{-1}$$

Similarly, the cutoff wave number for mode 2, the $TE_{1,1}$ mode is calculated as

$$k_{\perp 2} = \frac{1.841}{1.47} = 1.25 \text{ cm}^{-1}$$

The axial Bragg periodicity vector (k_B) was calculated using the value for the longtitudinal period of the helical corrugation d = 2.89 cm,

$$k_B = \frac{2\pi}{2.89} = 2.17 \text{ cm}^{-1}$$

The coupling coefficient κ, was calculated from equation 2-67,

$$\kappa = \frac{1}{2r_0^3 k_0^2} \frac{S_1^2 S_2^2 - m_1 m_2 r_0^2 \left(k_0^2 + k_{z1} k_{z2}\right)}{\sqrt{\left(S_1^2 - m_1^2\right)\left(S_2^2 - m_2^2\right)}}$$

Where S_1 and S_2 are the normalised coupling coefficients of the two modes. The corrugation amplitude in the code is given by l = 0.14 cm, m_1 and m_2 are the azimuthal components.The axial wavenumbers k_{z1} and k_{z2} are the axial wavenumbers of the $TE_{2,1}$ and $TE_{1,1}$ modes, respectively.These are calculated as follows:

$$k^2 = k_{\perp 1}^2 + k_z^2$$

$$k^2 = k_{\perp 2}^2 + \left(k_z + k_B\right)^2$$

$$k_{z1} = -\left(\frac{k_{\perp 1}^2 - k_{\perp 2}^2 - k_B^2}{2k_B}\right)$$

$$k_{z2} = k_B - k_{z1}$$

k_0 is the wavevector of exact Bragg resonance and is the intersection point of the coupled waves. It was calculated from $k_0 = \sqrt{k_{\perp 2}^2 + k_{z1}^2}$

The eigenwave dispersion results from the Matlab code are shown in Figure 3-4.

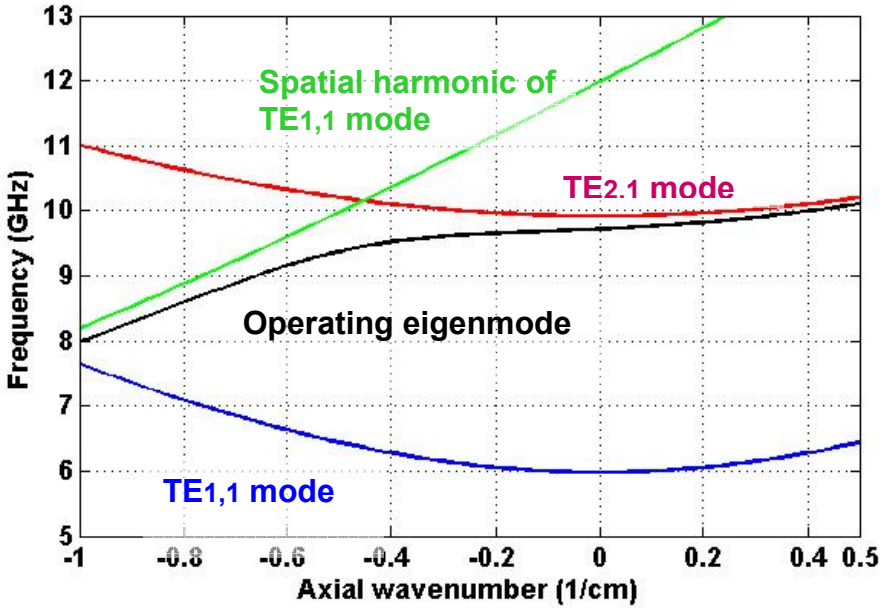

Figure 3-4 Dispersion of 3-fold helically corrugated waveguide calculated using coupled wave theory in Matlab code.

Exporting the data from Matlab [Hanselman 2005] as a text file to Microsoft Excel the operating eigenmode dispersion was charted as shown in Figure 3-5.

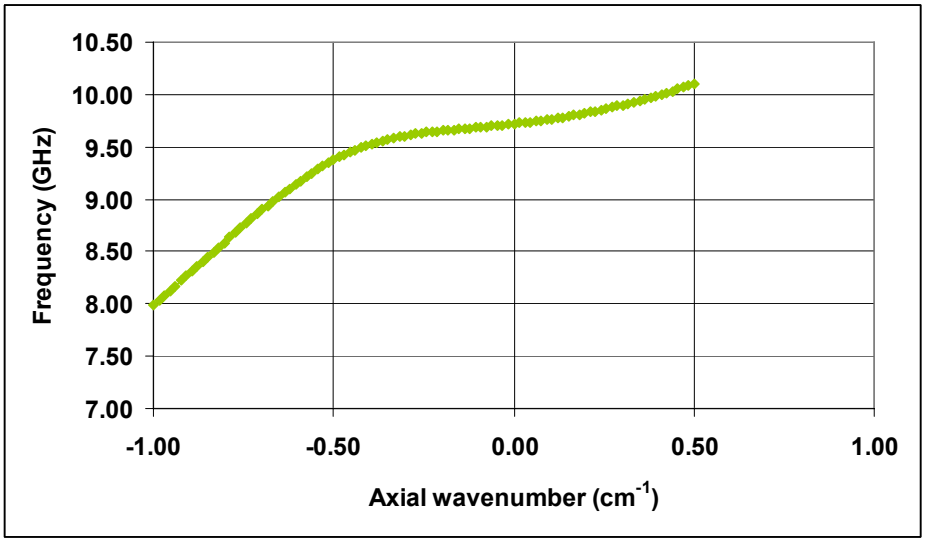

Figure 3-5 Eigenmode dispersion diagram from coupled wave theory data.

The corresponding group velocity dispersion was calculated using the data from the eigenwave dispersion curve of Figure 3-5. By applying a best fit trend line on top of

the curve the resultant 6th order polynomial could be differentiated in order to calculate the group velocity dispersion, the result of which is shown in Figure 3-6.

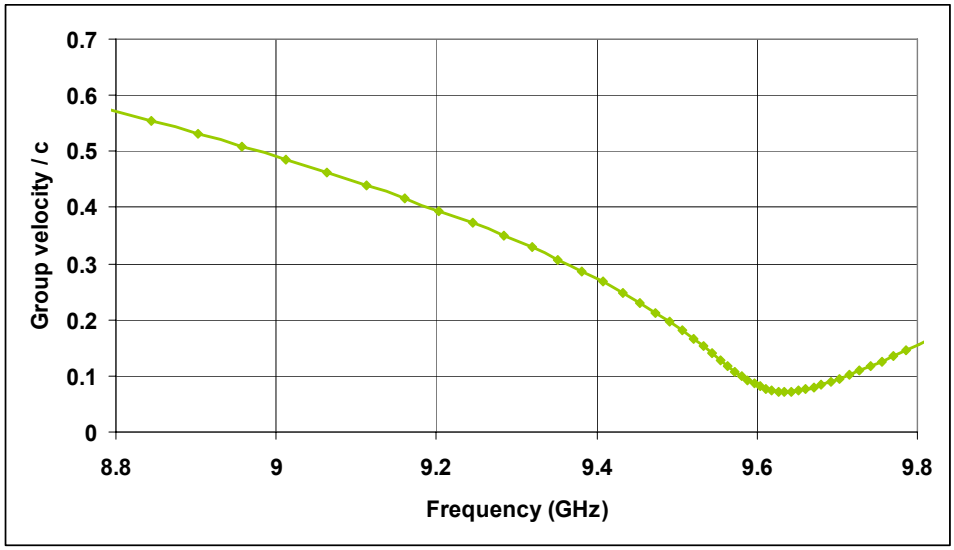

Figure 3-6 Group velocity dispersion plot calculated from coupled wave theory eigenwave dispersion data.

From Figure 3-6 the minimum group velocity was 0.07c at 9.65 GHz to a maximum group velocity of 0.57c at 8.8 GHz.

3.3 EIGENWAVE DISPERSION CALCULATED NUMERICALLY

The eigenwave dispersion properties of the 3-fold helically corrugated were determined numerically using CST MWS. The eigenmode solver in the CST MWS can simulate the electromagnetic behaviour of closed resonant structures. In this case it was used to build a computational model of the 3-fold helically corrugated waveguide to show the field distribution of the modes as well as the eigen-frequencies. The eigenwave equation shown below in equation 3-1 was used by the program to determine the eigen-frequencies and electromagnetic field patterns (eigenmodes) using the technique of finite element analysis (FEA), [Eastwood 1997].

$$\nabla^2 \underline{E} = -\omega^2 \mu\varepsilon E \qquad \textbf{Equation 3-1}$$

FEA is a system whereby the solutions to a partial differential equation (PDE) are found by approximating the PDE to a system of ordinary differential equations and integrating these equations. The Advanced Krylov Subspace (AKS) method was chosen as the most suitable eigenmode solver, [CST MWS 2009]. To obtain the eigenmode dispersion different input values of the axial wavenumber were calculated from the varying boundary phase angle (θ).

A single period (2.89 cm) of the 3-fold helical waveguide shape was created in CST MWS. Using a visual basic application (VBA) macro (Appendix E) an outline of the front-face of the helical guide was generated as show in Figure 3-7 below,

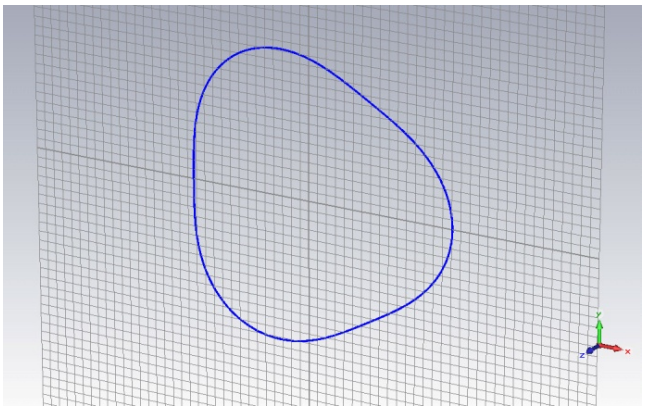

Figure 3-7 Curve outline of 3-fold helical face created using VBA macro.

Using the graphical user interface (GUI) within CST MWS the curve outline produced from the VBA macro was extruded to 2.89 cm and the helical shape twisted by 120˚. The angle of twist was calculated from 360˚ divided by the number of helical folds i.e. for the 3-fold this was $360^{\circ}/3$. The 120˚ angle of twist is input as a positive number in CST MWS to give the twist in the clockwise direction which is representative of the 3-fold helically corrugated waveguide, (Figure 3-8).

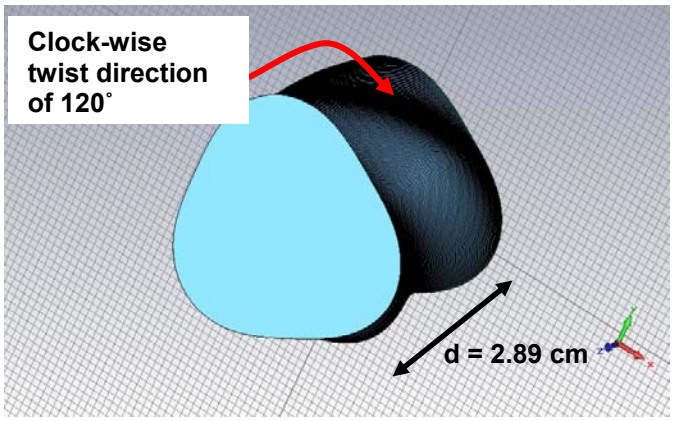

Figure 3-8 CST MWS model of single period of 3-fold helically corrugated waveguide.

The eigenmode solver was set to find the eigen-frequencies within the frequency range 8.0 GHz to 10.0 GHz. The output from the numerical findings is shown in Figure 3-9; an eigenmode contour plot showing both the electric (Figure 3-9a) and magnetic field (Figure 3-9b) contour profiles of the eigenmode.

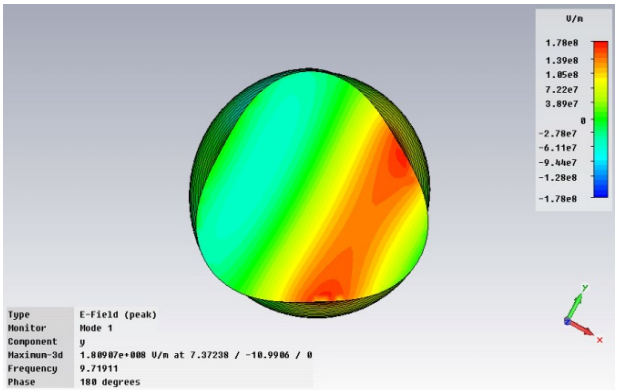

(a)

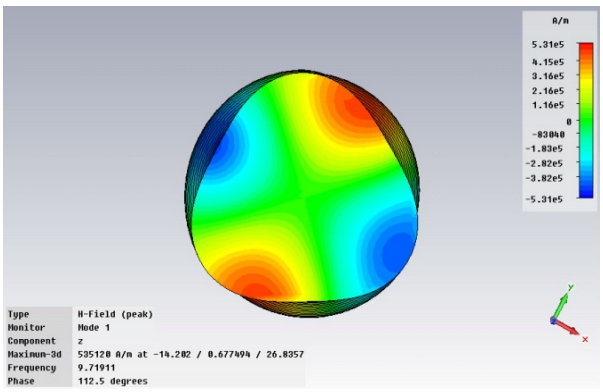

(b)

Figure 3-9 Eigenmode contour plots of (a) electric field and (b) magnetic field; red is region of larger amplitude and blue is lower amplitude region.

The boundary phase angle (θ) was varied from -180˚ to 180˚ degrees at 5˚ intervals and for each eigen-frequency detected the corresponding axial wavenumber k_z, was calculated using equation 3-2 below,

$$k_z = \frac{\theta}{d}$$ **Equation 3-2**

where d is the corrugation period.

The results from the CST MWS findings where plotted to show the eigenmode dispersion, Figure 3-10 below,

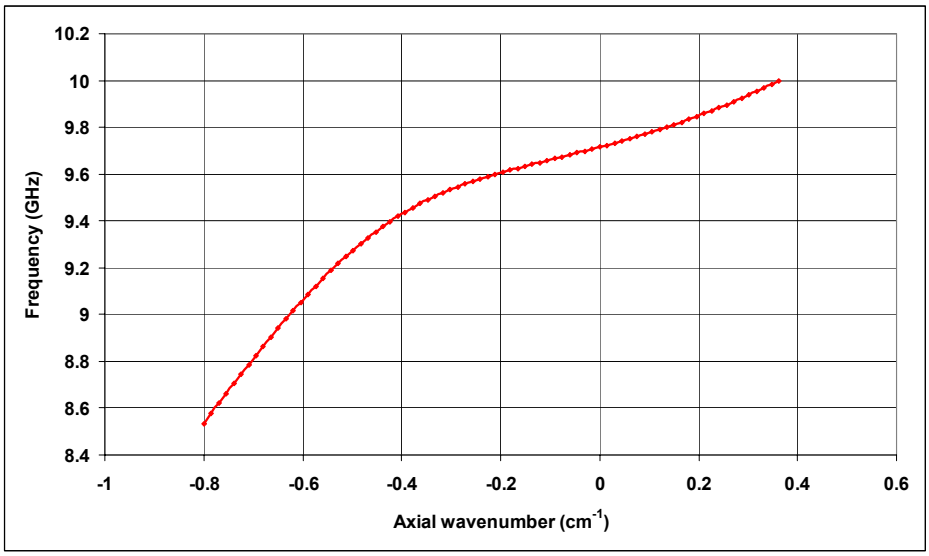

Figure 3-10 Eigenmode dispersion plot using CST MWS data.

The corresponding group velocity dispersion for the eigenmode was calculated in Microsoft Excel. The eigenmode curve of Figure 3-10 had a best-fit polynomial trend line applied to the data. From the derivative of the polynomial the group velocity dispersion was calculated as shown in Figure 3-11.

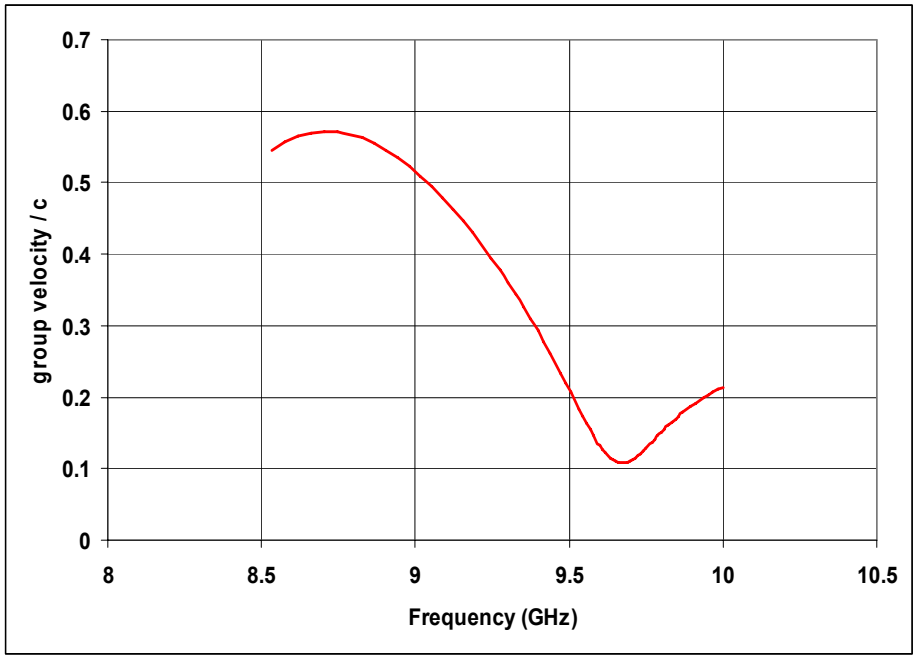

Figure 3-11 Group velocity dispersion calculated from CST MWS eigenwave dispersion data.

Figure 3-11 shows the group velocity extends at its minimum point from 0.11c at 9.66 GHz to a maximum value 0.56c at 8.8 GHz.

3.4 EIGENWAVE DISPERSION CALCULATED EXPERIMENTALLY

The experimental method used to measure the dispersion was based on the use of a vector network analyzer (VNA) to directly measure the difference between the phases of the signal at the input and output calibration planes as a function of frequency, [Burt 2004]. By measuring the phase difference ($\Delta\varphi$) the axial wavenumber (k_z) for the operating eigenwave was determined in a length of helically corrugated waveguide (L) using equation 3-3 below,

$$\Delta\varphi = k_z L \qquad \textbf{Equation 3-3}$$

In the VNA experiment the excitation of an eigenwave was ensured by introducing a circularly polarised $TE_{1,1}$ mode to a regularly corrugated section of 3-fold helical waveguide through a helical taper. The helical taper had a gradual increase in corrugation amplitude to allow the $TE_{1,1}$ to be transformed into the operating eigenmode. Using an elliptical polariser the linearly polarised $TE_{1,1}$ was converted to a left-circularly circularly polarised $TE_{1,1}$ wave, [Appendix F, Cornbleet 1976, Hecht 1987]. The measured structure was bound on each side by a helical taper, elliptical polariser and circular-to-rectangular adapter connected to port 1 and port 2 of the Anritsu VNA, (Figure 3-12).

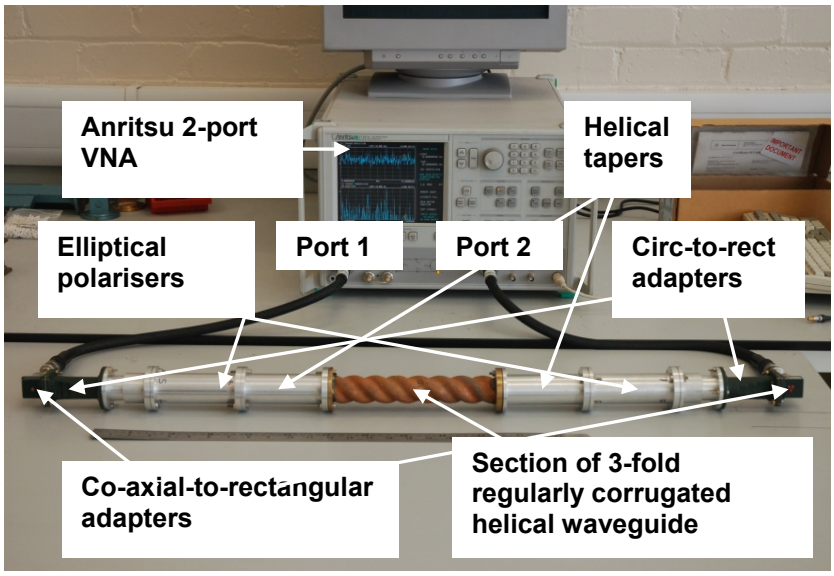

Figure 3-12 Experimental set-up in RF laboratory for 3-fold helically corrugated waveguide dispersion measurement using VNA.

The 2-port Anritsu VNA was calibrated using a 12-term, line-reflect-line (LRL) calibration that excluded isolation, [Anritsu 2007]. The frequency range of the calibration was taken from 8.2 GHz to 10.2 GHz and using the maximum data points of 1601 on the VNA. The calibration planes were each set to be at the connection ends between the co-axial-to-rectangular adapters at each end of the experimental set-up. The first measurement was with the device under test (DUT) in place, which was the section of 3-fold regularly corrugated helical waveguide. The phase difference as a function of frequency was recorded. Second, the measurement was repeated with the DUT removed. The measured phase as a function of frequency data from the VNA was analysed using Microsoft Excel. Figure 3-13 (a) shows the raw VNA data and (b) shows the VNA digitally processed data resulting in continuous functions i.e. without the 360˚ jumps.

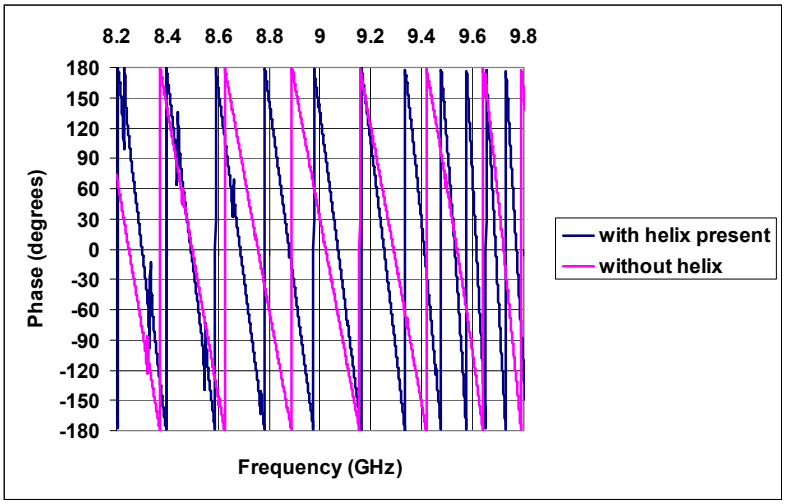

(a)

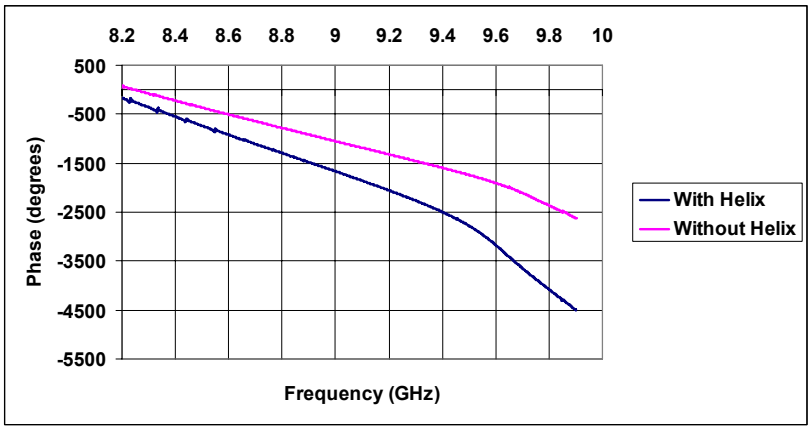

(b)

Figure 3-13 VNA phase measurement: (a) raw data from experiment and (b) after digital processing to remove 360˚ phase jumps.

The measured phases of Figure 3-13 were subtracted from one another which enabled the impact of the DUT to be selected. Taking the length of the DUT to be 23.12 cm and using the data calculated to get the axial wavenumber k_z the eigenmode dispersion was found as shown below in Figure 3-14.

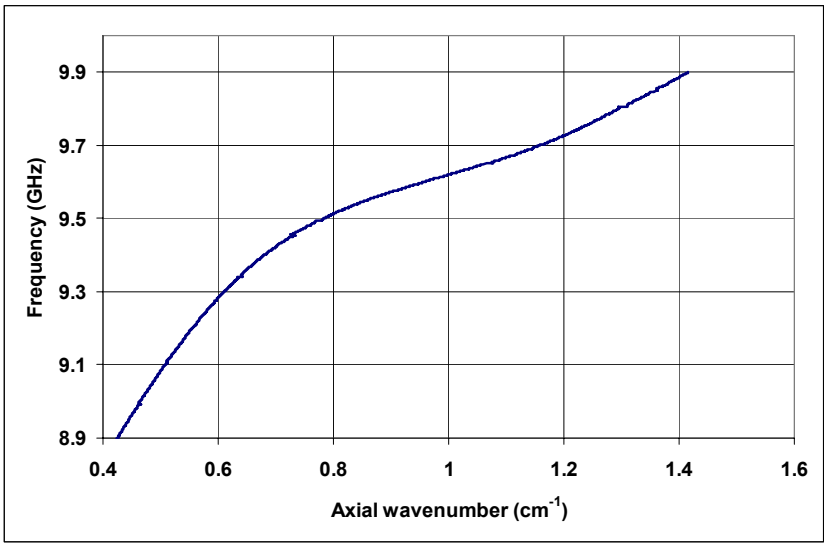

Figure 3-14 Eigenmode dispersion plot from VNA measurement data.

The group velocity dispersion was calculated from the above eigenwave dispersion plot of Figure 3-14 using the derivative of the best fit polynomial. The corresponding group velocity dispersion is shown in Figure 3-15

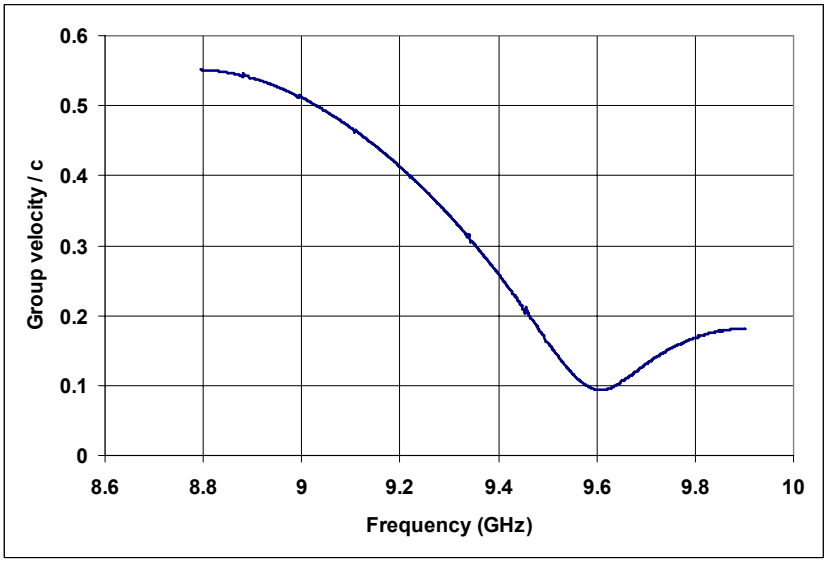

Figure 3-15 Group velocity dispersion plot using VNA eigenwave dispersion data.

From Figure 3-15 the minimum group velocity was measured to be 0.09c at 9.6 GHz and a maximum group velocity of 0.55c at 8.8 GHz.

3.5 ANALYSIS OF EIGENWAVE DISPERSION RESULTS

The results from the eigenwave dispersion measurements; analytical, numerical and experimental were compared on a single chart in Microsoft Excel, (Figure 3-16). It was found that in the frequency range of 9.0 GHz to 9.45 GHz the eigenwave dispersions calculated from the three methods are in very good agreement with one another. From 9.45 GHz to 9.8 GHz there is a deviation of the measurements. The experimental and analytical dispersion results agree well with each other from 8.8 GHz to 9.62 GHz.

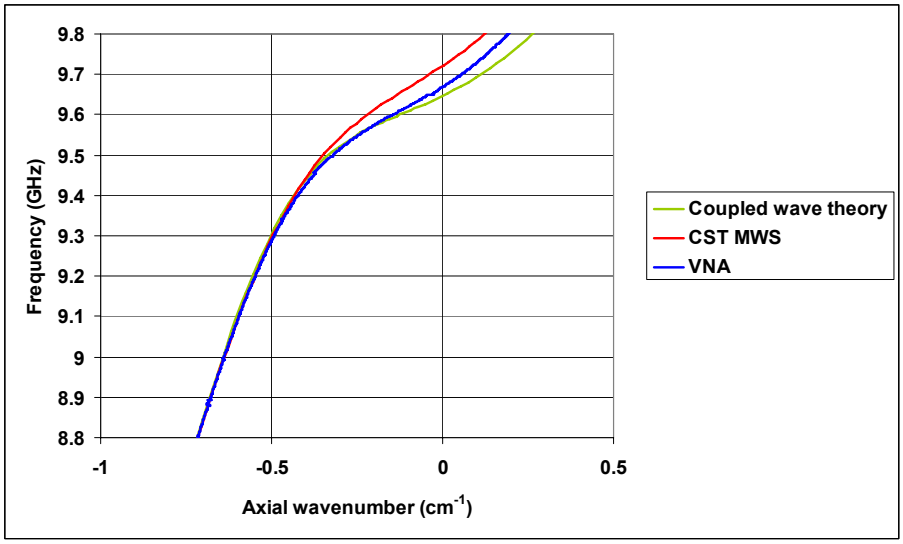

Figure 3-16 Chart of of eigenwave dispersion results.

The group velocity dispersions are collated in a single chart (Figure 3-17)

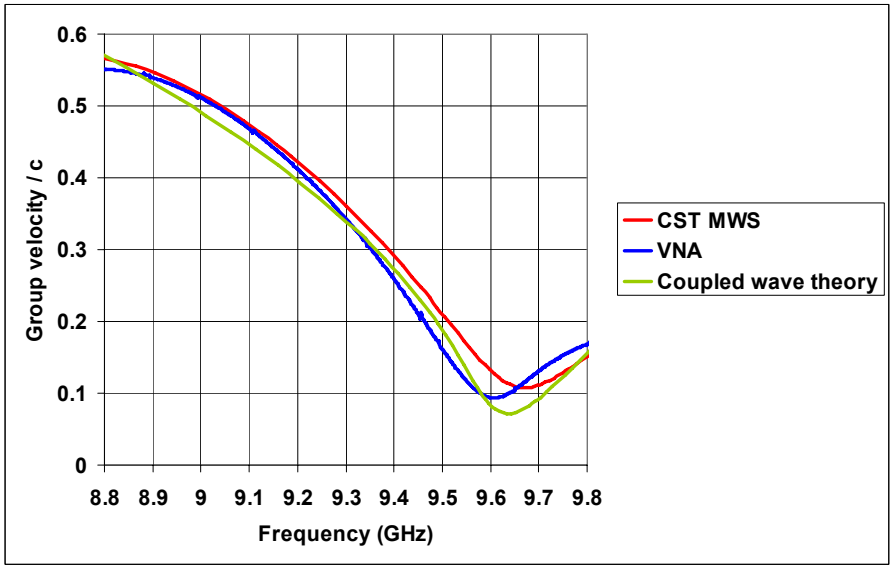

Figure 3-17 Chart of group velocity dispersion results.

A table was constructed (Table 3-2) to show the pertinent findings from the group velocity chart

	Minimum v_{gr}/c	Maximum v_{gr}/c
Numerical (CST MWS)	0.11	0.56
Experimental (VNA)	0.09	0.55
Analytical(coupled waves)	0.07	0.57

Table 3-2 Group velocity results for 3-fold helically corrugated waveguide.

It was established from the numerical findings the minimum group velocity was 0.11c at 9.66 GHz and had maximum group velocity of 0.56c at 8.8 GHz. From the experimental findings the minimum group velocity was 0.09c at 9.61 GHz and had maximum group velocity of 0.55c at 8.8 GHz. From the analytical findings, the minimum group velocity was 0.07c at 9.65 GHz and had maximum group velocity of 0.57c at 8.8 GHz. The average minimum group velocity was 0.09c and the average maximum group velocity was 0.56c

3.6 LOSSES MEASUREMENT USING SNA

To establish the ohmic losses of the 3-fold helically corrugated waveguide a measurement of the S_{21} scattering parameter was performed using the scalar network analyzer (SNA). In the RF laboratory a Hewlett Packard (HP) 8757D SNA and HP 83752B frequency-sweeper (Figure 3-18) were used to measure the transmitted S_{21} signal as a function of frequency and magnitude. The frequency-sweeper was set to a start frequency of 8.8 GHz and stop frequency of 10.2 GHz giving a 1.4 GHz frequency-sweep range.

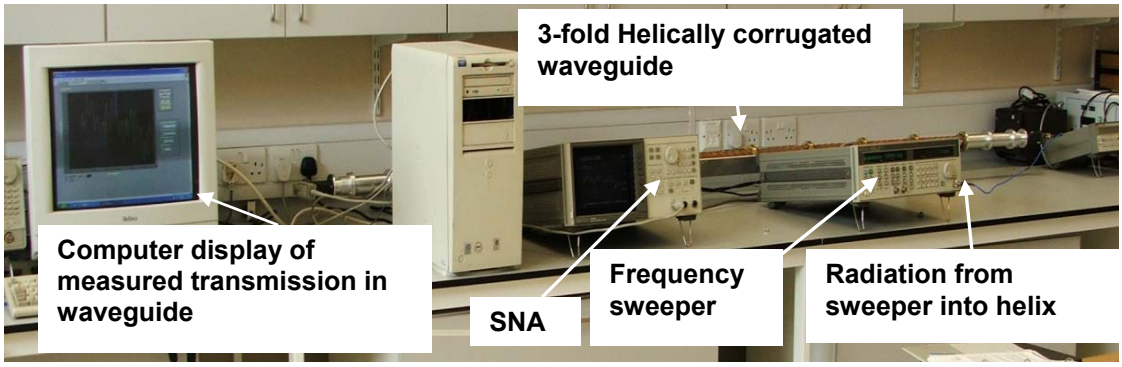

(a)

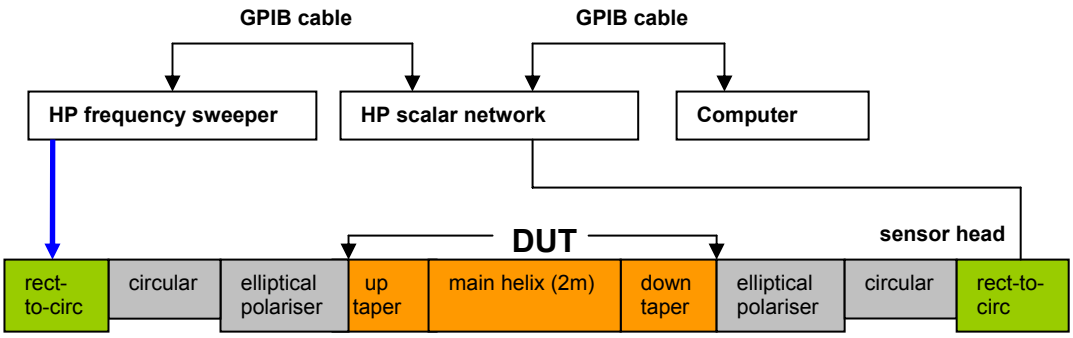

(b)

Figure 3-18 SNA losses measurement: (a) Digital photograph of experimental set-up in the RF laboratory and (b) schematic of set-up for measurement.

A 'thru' calibration was performed on the SNA, [Hewlett Packard 1992]. The calibration planes were up-to-and including the ends of the elliptical polarisers. The measurement of the S_{21} scattering parameter was measured for the 76 period helically corrugated waveguide inclusive of the up- and down-helical waveguide tapers. The microwave radiation from the frequency-sweeper was transmitted

through the 3-fold helically corrugated waveguide and the measured transmission data from the SNA was captured on the computer in order to export the data for analysis. The exported data of the measured transmission (S_{21}) result is shown in Figure 3-19 below,

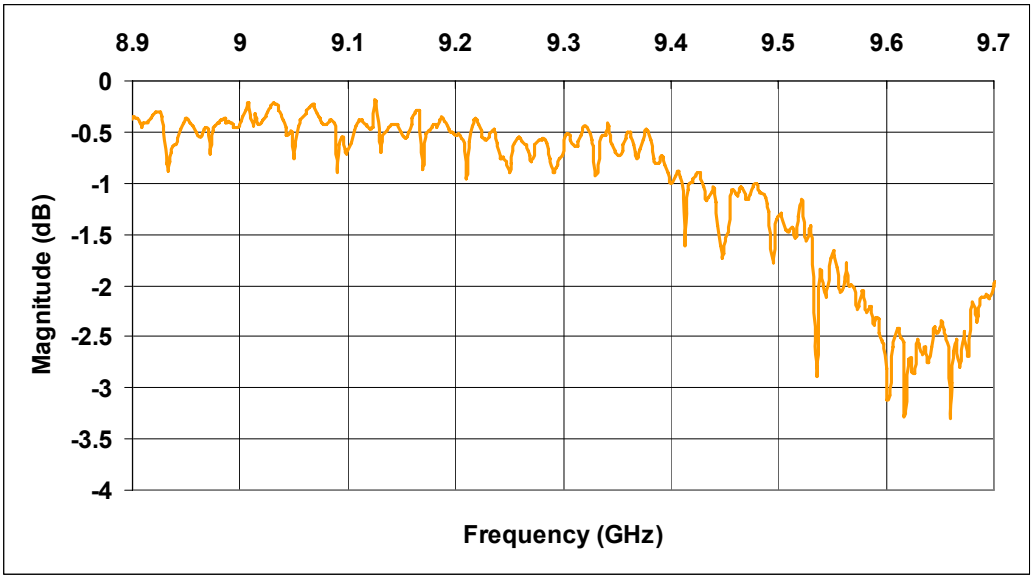

Figure 3-19 SNA transmission (S_{21}) measurement 8.8 GHz – 9.8 GHz.

Using the cursor facility on the SNA the magnitude of the microwave signal was measured at several points on the SNA screen and the results are shown in Table 3-3 below,

Frequency (GHz)	Loss (dB)
9.0	0.44
9.1	0.66
9.2	0.52
9.3	0.62
9.4	1.00
9.5	1.32
9.6	2.81

Table 3-3 Loss measurements for 3-fold compressor using SNA.

From Table 3-3 the losses were measured to be lowest at 0.44 dB at 9.0 GHz and highest at 9.6 GHz where the losses were measured to be at 2.81 dB.

3.7 LOSSES MEASUREMENT USING VNA

The VNA was calibrated [Anritsu 2007] using a line-reflect line technique (LRL) and the losses measured by measuring the transmission scattering parameter S_{21} through the 3-fold helically corrugated waveguide. The experimental set-up is shown below in Figure 3-20.

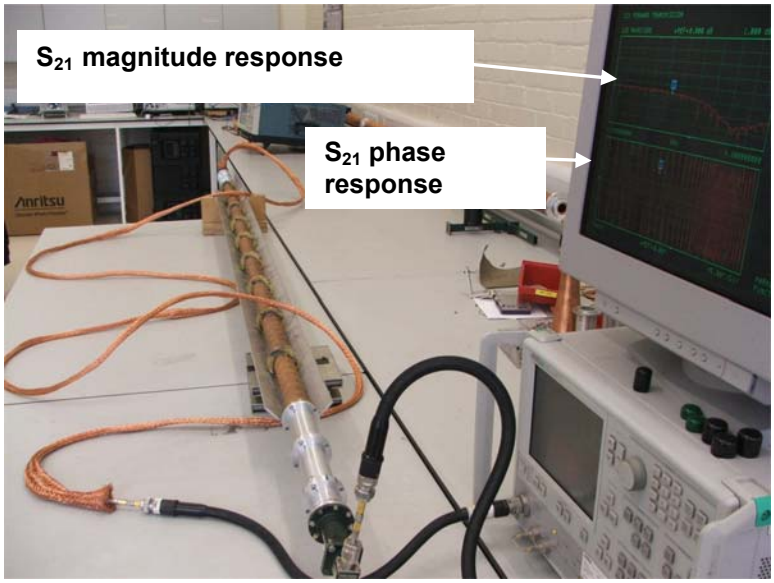

Figure 3-20 Digital photograph of experimental set-up in RF laboratory for transmission (S_{21}) measurement using VNA.

Measurement of the S_{21} parameter was recorded from the VNA and the data exported to Microsoft Excel where a chart was produced, (Figure 3-21).

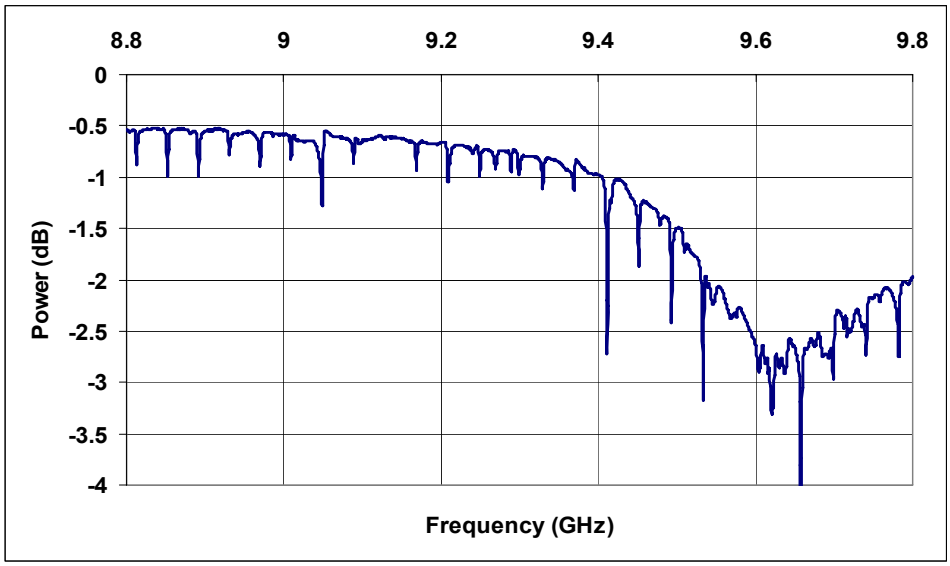

Figure 3-21 VNA transmission (S_{21}) measurement from 8.8 GHz – 9.8 GHz.

A series of magnitude values were measured at specified frequencies from 9.0 GHz to 9.6 GHz using the cursor facility on the VNA to locate the point of interest. The recorded values for the magnitude at such frequencies are shown in Table 3-4 below,

Frequency (GHz)	Loss (dB)
9.0	0.59
9.1	0.65
9.2	0.66
9.3	0.92
9.4	0.98
9.5	1.50
9.6	2.64

Table 3-4 Loss measurements for 3-fold compressor using VNA.

From Table 3-4 the lowest loss of 0.59 dB was measured at 9.0 GHz and the largest losses of 2.64 dB were measured at 9.6 GHz.

3.8 ANALYSIS OF LOSSES MEASUREMENTS

The measured results from the SNA and VNA loss measurements of the 3-fold helically corrugated waveguide were plotted on a single chart for comparison as shown in Figure 3-22,

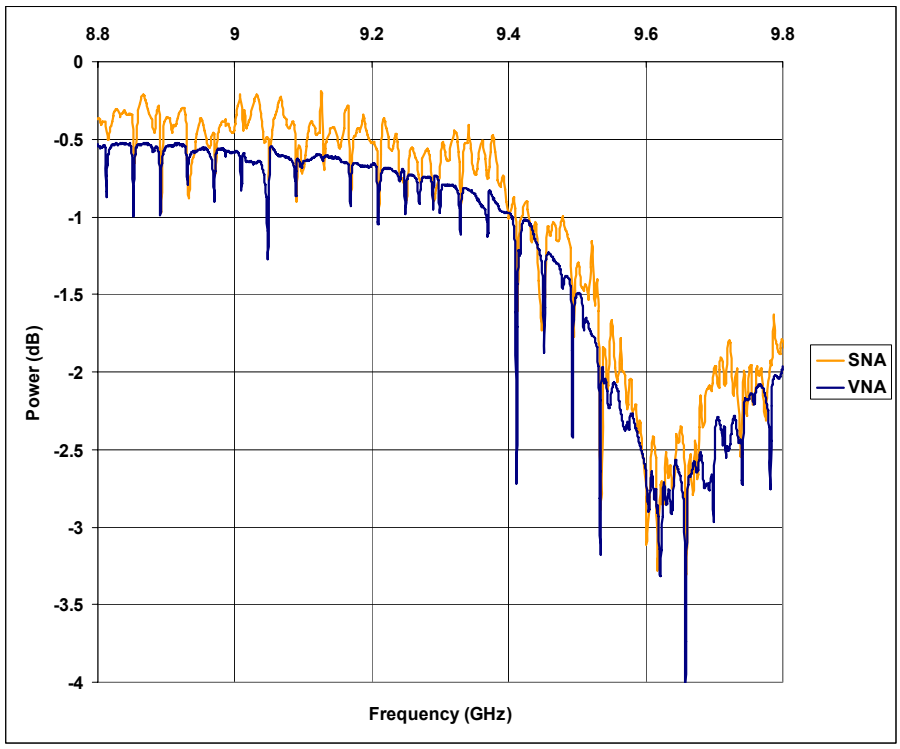

Figure 3-22 Chart of 3-fold helically corrugated waveguide transmission from SNA and VNA measurements.

Table 3-5, below, shows the difference in loss between the two measurement devices (SNA and VNA) for specific frequencies from 9.0 GHz to 9.6 GHz.

Frequency (GHz)	Difference in loss measurements (dB)
9.0	0.15
9.1	0.01
9.2	0.14
9.3	0.30
9.4	0.02
9.5	0.18
9.6	0.17

Table 3-5 Comparison of loss measurements for SNA and VNA.

From Table 3-5 at 9.3 GHz the maximum difference between the SNA result and the VNA result was 0.30 dB and the minimum difference was 0.01 dB at 9.1 GHz. The average value in difference is 0.12 dB with a median value of 0.15 dB.

3.9 SIMULATION OF MICROWAVE PULSE COMPRESSION

A simulation to determine the microwave pulse compression factor was achieved using a Matlab code which used Fourier transforms and a 1-D Fourier optics approach as outlined in Burt 2004 and Samsonov 2004. The evolution of a plane wave is given by equation 3-4 below,

$$u(z,t) = A(z,t)\exp(-i\omega t + ikz) \qquad \textbf{Equation 3-4}$$

where in a linear dispersive medium, $k = k(\omega)$.

The resultant wave propagating through the medium can be represented in the form of equation 3-5 given by,

$$u(z,t) = \frac{1}{2\pi}\int_{-\infty}^{\infty}\int_{-\infty}^{\infty} u_o(t')\exp[-i\omega(t-t') + ik(\omega)z]dt'd\omega \qquad \textbf{Equation 3-5}$$

where $u_0(t) = u(z=0,t)$ is the input signal.

The simulation used the optimum dispersion for the 3-fold copper helically corrugated waveguide shown in Figure 3-23 and using a numerical integration technique the integral of equation 3-5 was solved to give the output (compressed) microwave pulse. From this output pulse the compression factor for the 3-fold helically corrugated waveguide was calculated using the ratio of the peak value of the compressed pulse and the peak value of the input pulse. The ohmic losses in the waveguide are accounted for by way of the imaginary component of the axial wave number k_z in the equations. The input pulse was simulated for the given optimum frequency-sweep for the 3-fold pulse compressor of 9.61 – 9.1 GHz over a pulse duration of 100 ns.

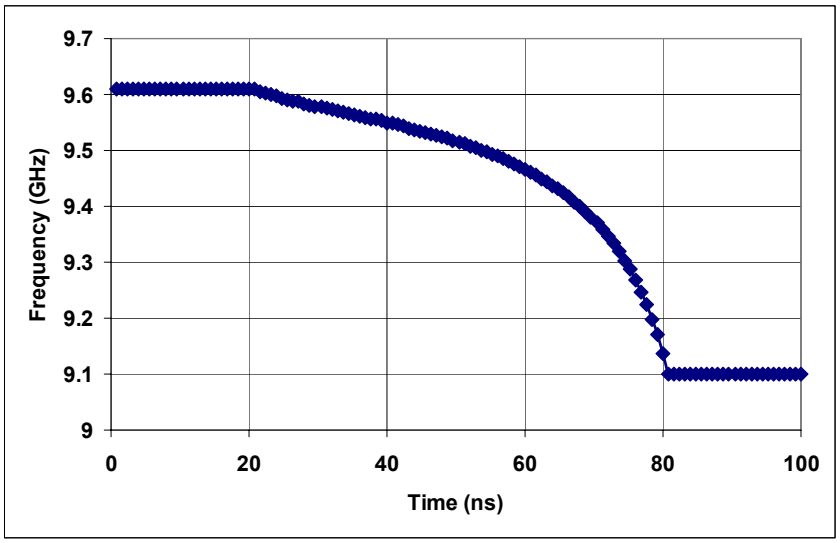

Figure 3-23 Optimum frequency sweep for 3-fold helically corrugated waveguide compressor.

The simulation normalises the input pulse amplitude to unity. The simulated compressed pulse is calculated and using the peak value of the compressed pulse the peak-power compression ratio is determined from the Matlab code. The compression factor was calculated to be 26 as shown in Figure 3-24 below,

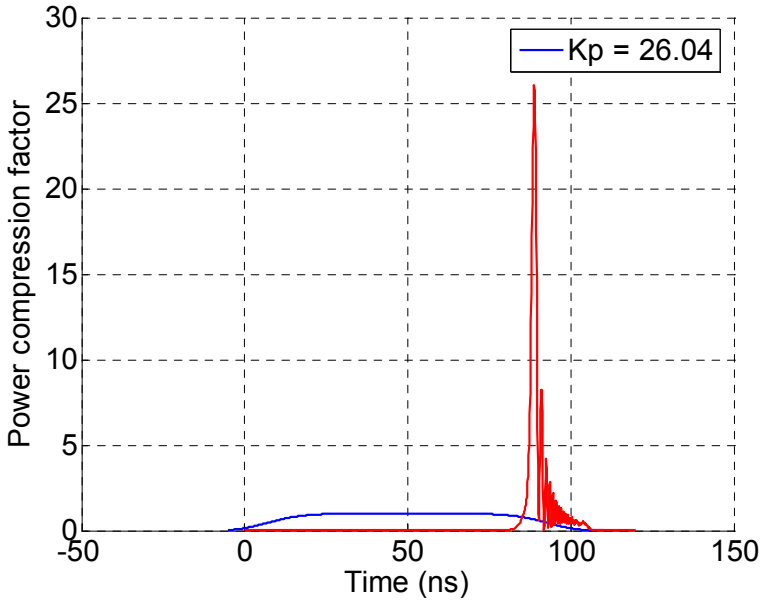

Figure 3-24 Simulation of input pulse and corresponding compressed pulse.

Chapter 4

The 3-Fold Microwave Pulse Compression Experiments

The chapter details the X-band sweep-frequency based microwave pulse compression experiments at low (mW) and medium (kW) powers using a 3-fold helically corrugated waveguide with arbitrary waveform generator (AWG) and vector signal generator (VSG). Results and analysis of the experimental findings are presented such as the peak power compression ratio and energy compression efficiency.

4.1 INTRODUCTION TO PULSE COMPRESSION EXPERIMENTS

X-band sweep-frequency based microwave pulse compression experiments using a 3-fold helically corrugated waveguide were carried out at both mW and kW power levels. The experiments use an input pulse where the dispersion characteristics of the input pulse were synthesized in a digital reconstruction using an Agilent arbitrary waveform generator (AWG) and an Agilent vector signal generator (VSG). The incorporation of this technology allowed for better control and performance of the input pulse to the microwave pulse compressor. Microwave measurements [Bryant 1993, Lance 1964] were performed for the a.c. input microwave pulses and a.c. output (compressed) microwave pulses. From the data of the microwave pulses the peak-power compression ratios and compression efficiencies were calculated. Furthermore, the rectified input and compressed microwave pulses were measured to also obtain the peak-power compression ratio.

4.2 PULSE COMPRESSION EXPERIMENTS AT mW POWERS

4.2.1 Measurement of a.c. microwave input pulse

From the eigenwave dispersion analysis of the 3-fold helically corrugated waveguide structure using analytical, numerical and experimental techniques as detailed in chapter 3, the necessary frequency-modulation of the input microwave pulse to obtain optimum values for microwave pulse compression was in the region of 9.61 GHz to 9.10 GHz. The frequency-modulated input pulse was created digitally and programmed within the AWG using a text file containing information on the pulse duration and frequency composition of the frequency-modulated input pulse. The text file was used as part of the Matlab code which created the input pulse within the AWG software, [Appendix G]. The AWG [Agilent 2006] sampled an input data point every 0.8 ns resulting in a reconstructed input pulse of 125 data points in length for a 100 ns second input pulse duration. The input microwave pulse was constructed with a 20 ns rise time, 60 ns continuous and a fall time of 20 ns (Figure 4-1 a), with the optimum frequency-modulation shown in (Figure 4-1 b) below,

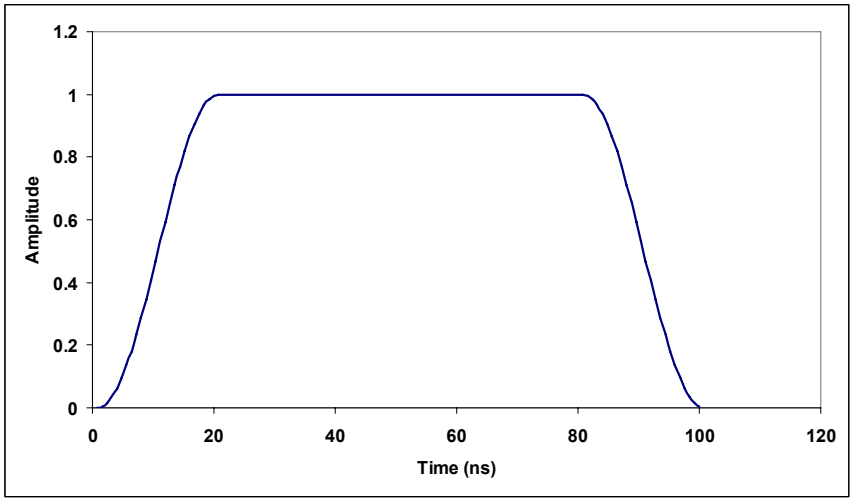

(a)

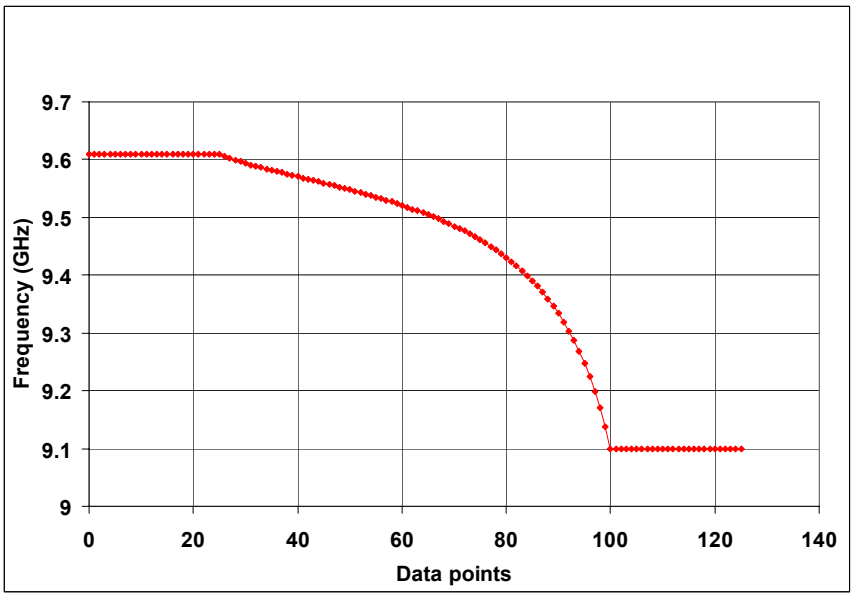

(b)

Figure 4-1 Input (a) pulse shape and (b) optimum frequency-sweep for AWG.

When the Matlab script from the AWG was executed the script outputs binary files. These binary files are outputs to channel 1 and channel 2 of the AWG. Through the control utility window of the GUI within the AWG computer interface the IQ (In-phase and Quadrature) data of the binary files was fed from the AWG to the IQ inputs of the VSG [Agilent 2006] where the VSG uses this IQ data to produce the microwave pulse to be used as the input microwave pulse to the pulse compressor. The experiments were carried out in the RF laboratory and the experimental set-up for measuring the input microwave pulse is shown in Figure 4-2,

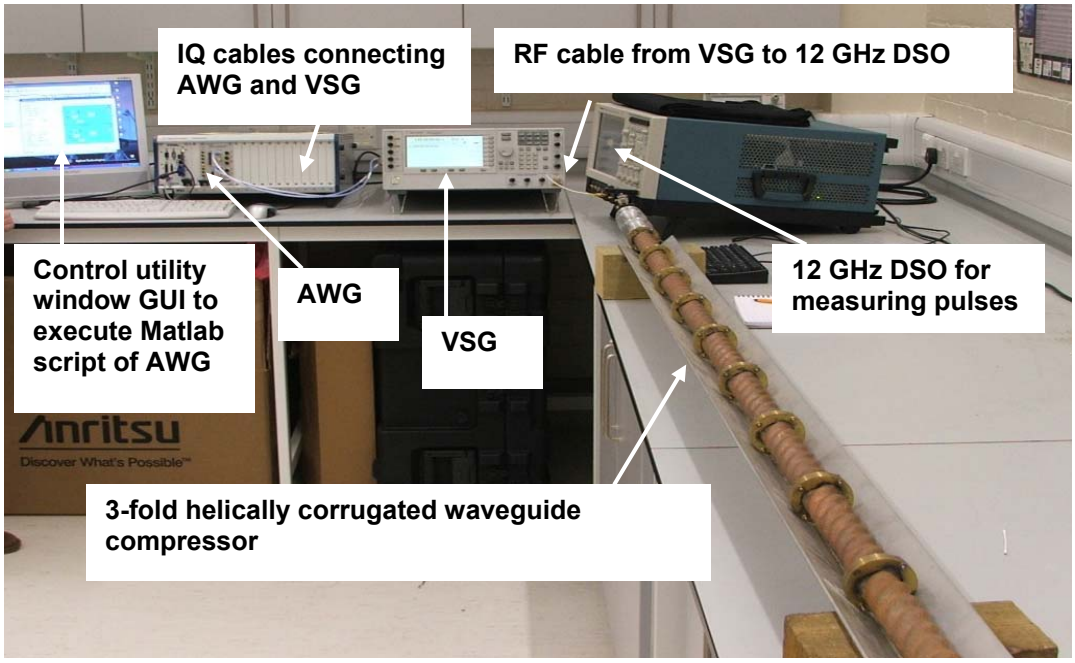

Figure 4-2 Experimental set-up in RF laboratory for 3-fold microwave pulse compression experiments at mW powers.

The a.c. microwave pulse from the output of the VSG directly fed into a co-axial-to-rectangular waveguide adapter via a RF cable connected to the input channel of the 12 GHz Tektronix Digital Storage Oscilloscope (DSO). The measured input pulse on the DSO is shown in Figure 4-3 (a).

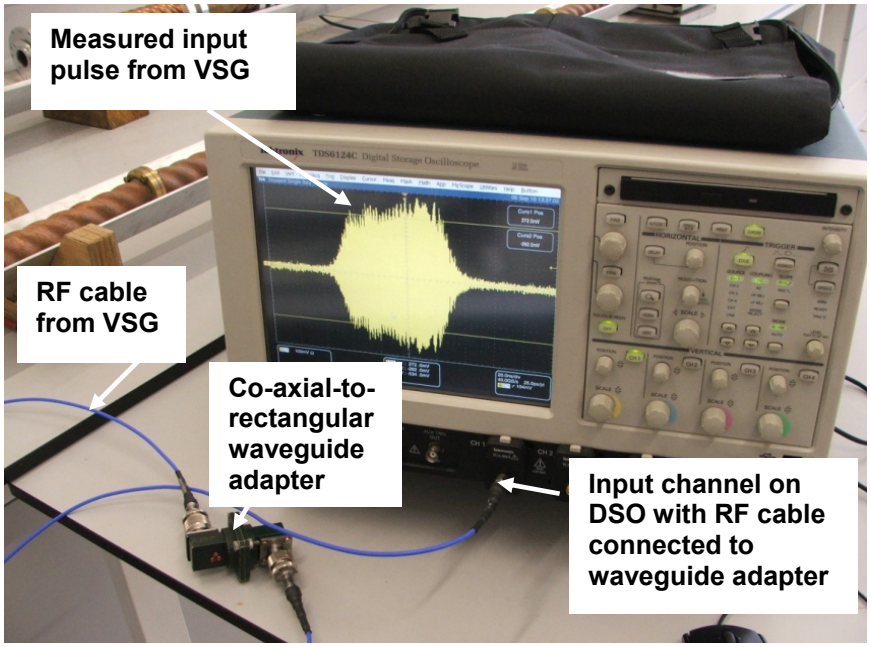

(a)

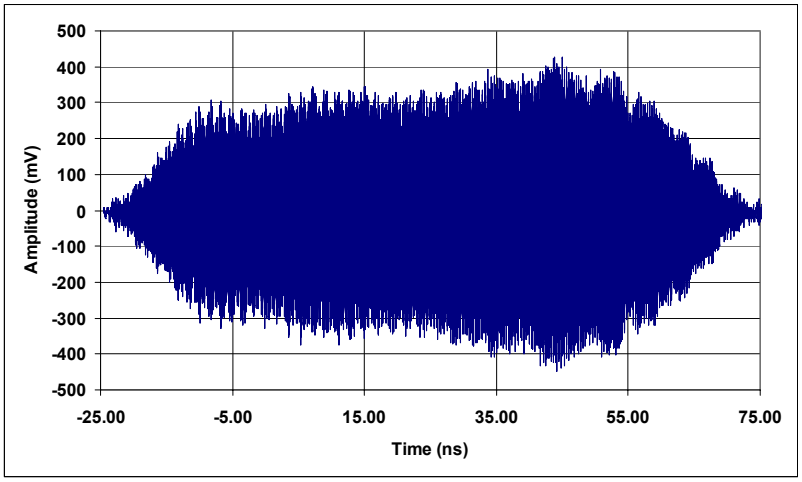

(b)

Figure 4-3 Input pulse measurement: (a) a.c. microwave input pulse on DSO and (b) chart of measured input pulse using Microsoft Excel.

The a.c. input microwave pulse shows the amplitude (mV) of the microwave as a function of time (ns). The power envelope of the input pulse was calculated using Microsoft Excel from V^2/R where R was the 50Ω input impedance of the DSO, (Figure 4-4).

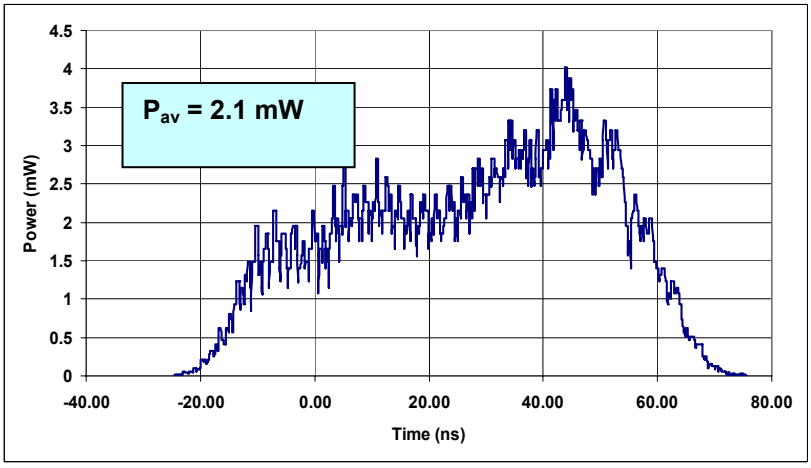

Figure 4-4 Power envelope of measured microwave input pulse.

The envelope shows there is a variation in the power of the microwave pulse over the duration of the pulse. The variation in power ranges from around 1.5 mW at the top of the pulse after 20 ns to a peak of 4 mW after 80 ns. The average power of the input pulse was calculated in Microsoft Excel to be 2.1 mW.

The measured time-domain input pulse on the DSO was analysed in the frequency-domain using a Matlab code in Appendix H, to calculate from the measured pulse data the frequency response for that pulse. Conversion of the waveform from the time-domain $f(t)$ to the frequency domain $f(\omega)$ was performed using a Fourier transform, [Kreyszig 2006]. The measured pulse sweep was compared with that of the programmed optimum sweep of the AWG, (Figure 4-5).

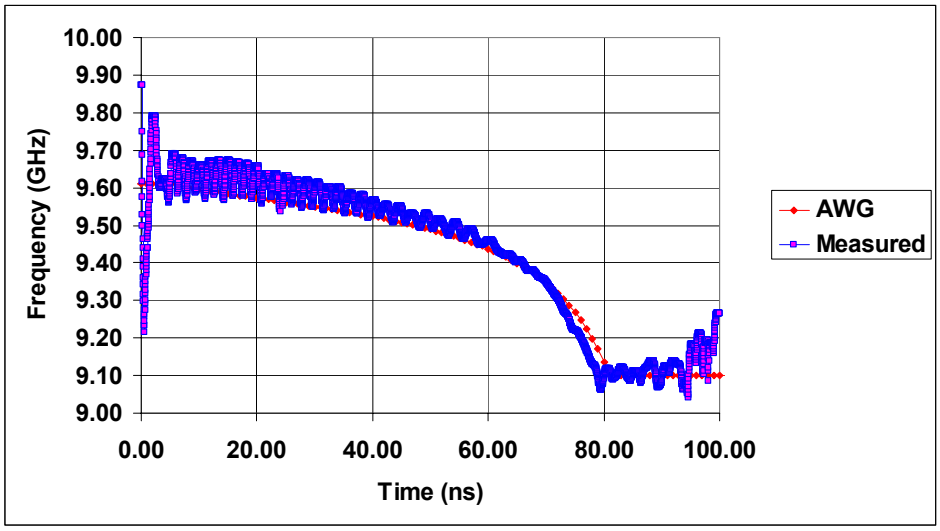

Figure 4-5 Frequency sweep: Measured (blue) and AWG programmed sweep (red).

From Figure 4-5 it can be seen that the frequency-sweep from the measured data from the input pulse is in good agreement with that of the frequency-sweep programmed into the Matlab script of the AWG.

4.2.2 Measurement of a.c. microwave output pulse

The output (compressed) microwave pulse was measured at the output end of the 3-fold helically corrugated waveguide pulse compressor. Figure 4-6 illustrates the transport of the microwave radiation within the 3-fold pulse compressor. In order to achieve microwave pulse compression the input microwave radiation from the VSG was launched from a WG16 waveguide as a $TE_{1,0}$ mode and passed through a rectangular-to-circular waveguide adapter where a linearly polarised $TE_{1,1}$ electromagnetic mode exits. This $TE_{1,1}$ mode travels through an elliptical polarizer which converts the linearly polarized $TE_{1,1}$ mode to a left circularly polarized $TE_{1,1}$

mode [Appendix F] that enters an up-taper which slowly converts the circular waveguide to that of the 3-fold helical waveguide structure. On entering the helically corrugated waveguide the left-handed circularly polarised $TE_{1,1}$ mode is scattered into the $TE_{2,1}$ mode resulting in an operating eigenwave which undergoes frequency-swept microwave pulse compression due to the dispersive properties of the waveguide.

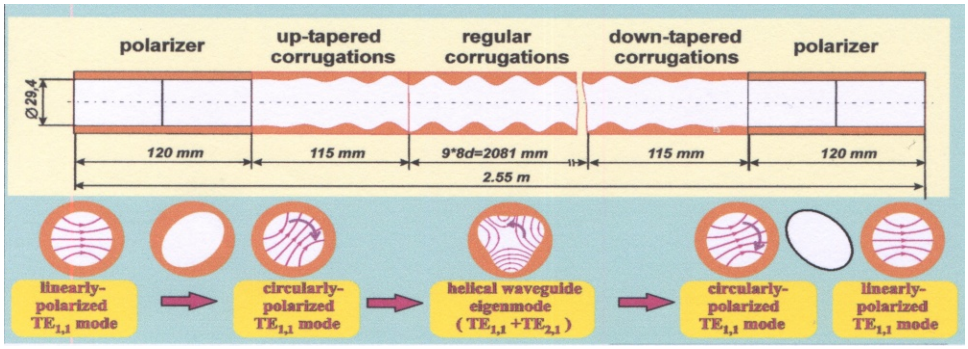

Figure 4-6 Schematic of mode transformation from input-to-output in 3-fold helically corrugated waveguide compressor.

At the output of the helically corrugated waveguide the opposite transitions occur which restore the pulse to the $TE_{1,0}$ mode where it is directly measured from the output section of the WG16 waveguide using the DSO. The a.c. compressed microwave pulse was measured on the DSO as shown in Figure 4-7 (a) and the chart of the input pulse from the measured pulse data is shown in Figure 4-7 (b).

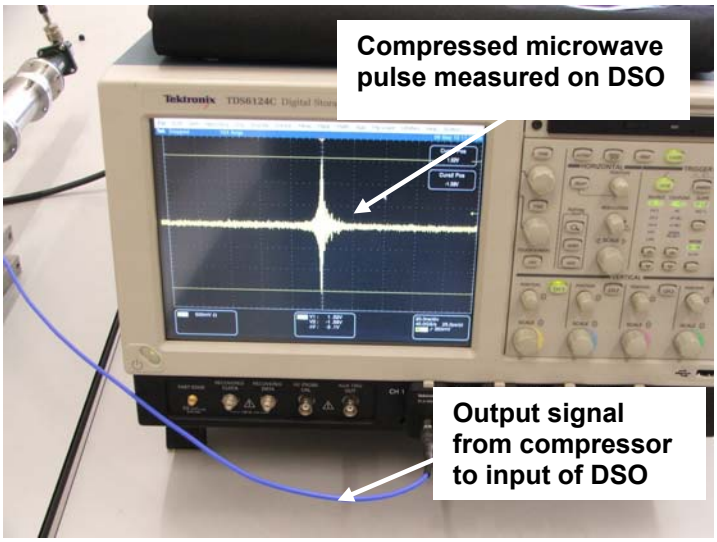

(a)

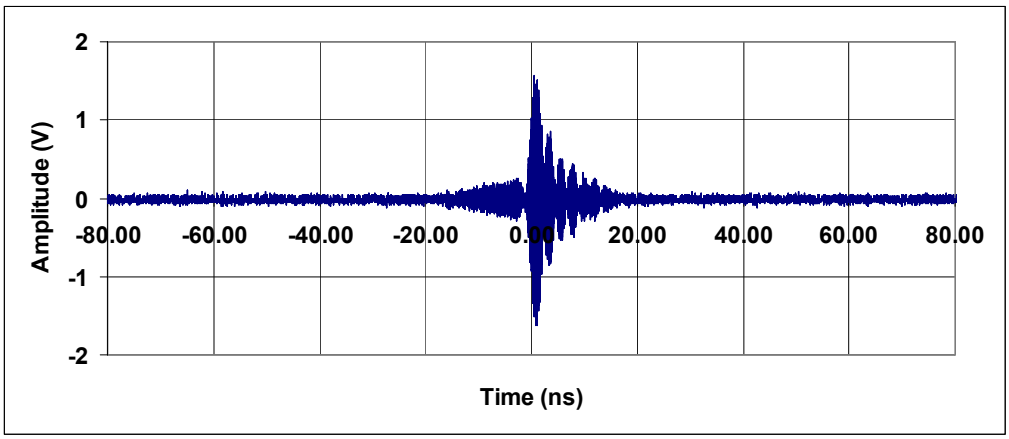

(b)

Figure 4-7 (a) Measurement of compressed microwave pulse on 12 GHz DSO and (b) chart of compressed microwave pulse.

In the same manner as for the input pulse the compressed pulse data from the DSO measurement was converted to a power envelope of the compressed pulse using Microsoft Excel as shown in Figure 4-8. The peak power was calculated to be 52.4mW and the full width half maximum (FWHM) duration calculated from the compressed pulse data to be 1.5 ns.

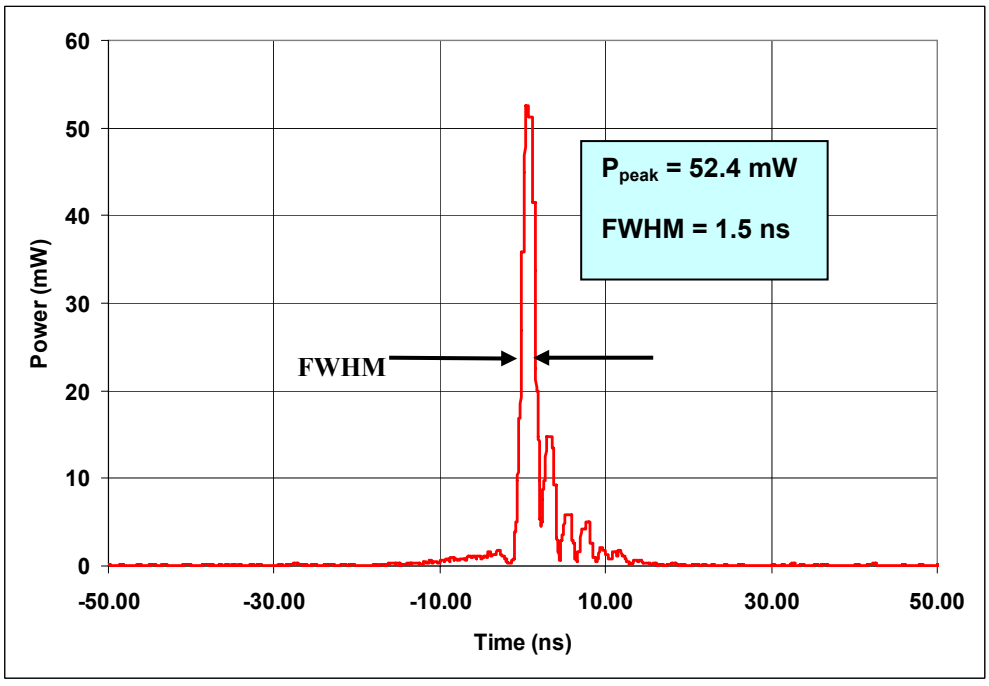

Figure 4-8 Power envelope of measured compressed microwave pulse.

The peak-power compression ratio was calculated from the power envelopes for the measured input and output (compressed) microwave pulses. Using the peak power (P_{peak}) for the compressed pulse to be 52.4 mW and the average power (P_{av}) in the input pulse to be 2.1 mW the power compression ratio was calculated to be 24.9 (25). The time compression ratio was calculated from the ratio of input pulse duration of 80 ns and the compressed pulse duration at FWHM of 1.5 ns to be around 53.

From the calculated power and the pulse duration the energy in the pulses was calculated for the input and output microwave pulses. The ratio of these two energies gave a pulse compression energy efficiency of 42 ± 5 %.

4.3 METHOD OF ATTENUATION EXPERIMENT AT mW POWERS

In section 4.2 measurement of the a.c. input and output microwave pulses lead to a calculated value for the peak-power compression ratio. In this section a different technique was used to establish the peak-power compression ratio for the pulse compressor. This technique is called the 'method-of-attenuation' within this thesis and involved measuring the rectified input and output microwave pulses and aligning their peaks by adjusting a microwave variable attenuator. From the variable attenuator reading taken from the barrel the compression factor was calculated using the calibration chart for the variable attenuator.

4.3.1 Measurement of rectified input microwave pulse

The rectified microwave input and compressed pulses were measured using a Hewlett Packard (HP) co-axial microwave crystal detector and a Flann microwave sliding vane variable attenuator. The input microwave pulse from the VSG propagates through the RF cable and into the co-axial microwave crystal detector and is measured on the 12 GHz Tektronix DSO. The trace of this input pulse was saved into the memory of the DSO to be compared with the output rectified pulse. The input pulse data was processed in Microsoft Excel and a chart of the measured rectified input microwave pulse is shown below in Figure 4-9.

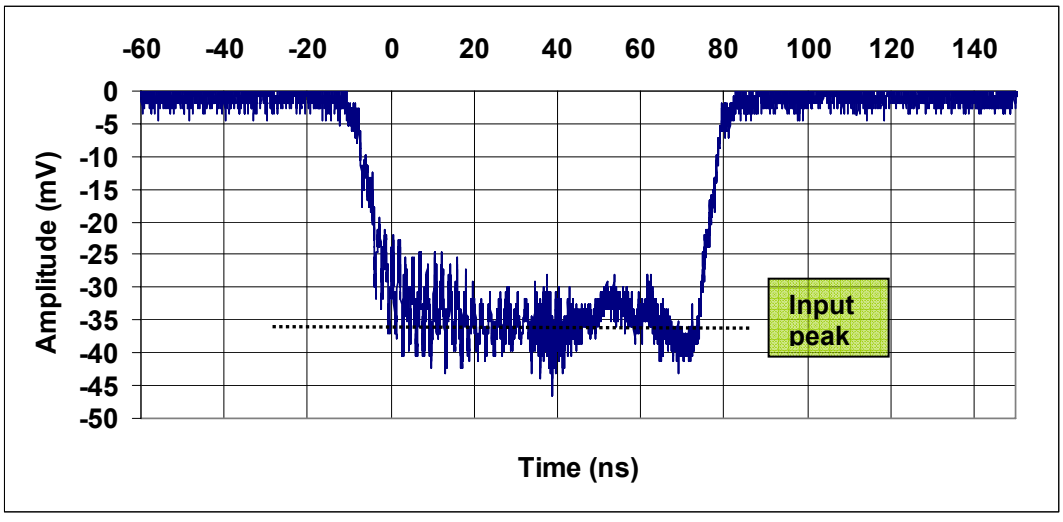

Figure 4-9 Measured rectified input microwave pulse using co-axial microwave crystal detector.

4.3.2 Measurement of rectified output microwave pulse

The co-axial microwave crystal detector was moved to the output end of the helically corrugated waveguide pulse compressor. The crystal detector was connected in series with a calibrated sliding vane variable attenuator, (Figure 4-10).

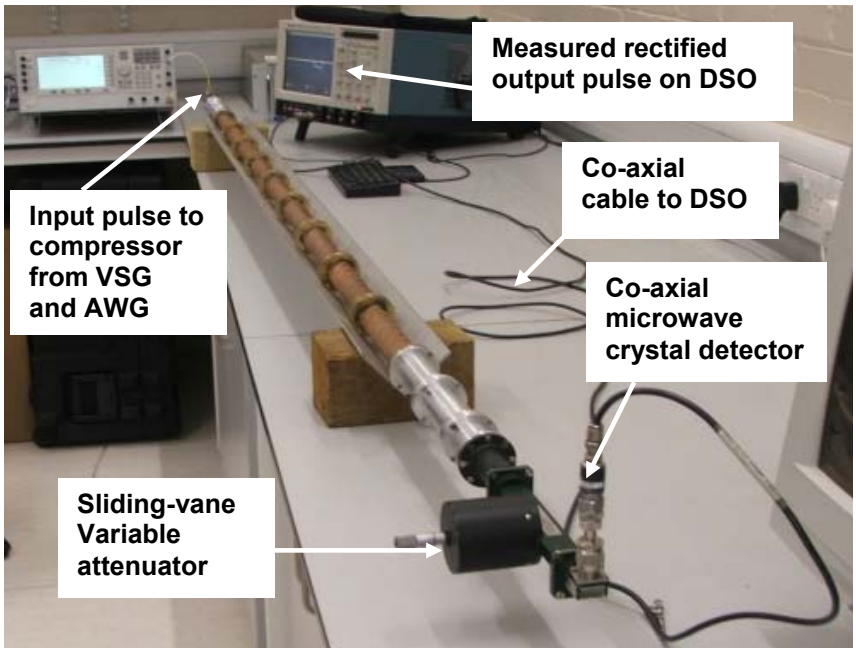

Figure 4-10 Digital photograph of experimental set-up to measure rectified compressed pulse.

The saved trace [Tektronix User Manual] of the rectified input pulse was loaded on the 'active' screen of the DSO where the compressed pulse was visible. The compressed pulse was larger than that of the input pulse. To resolve the signals so that the input and compressed are the same value on the DSO the compressed pulse was attenuated. By using the sliding vane microwave attenuator the barrel on the attenuator was adjusted as to attenuate the microwave signal so that the peak of the compressed pulse was matched to the peak of the input pulse. With the two pulses matched in amplitude the reading from the variable attenuator barrel was noted, [Squires 1997]. Using the calibration chart for the sliding vane microwave variable attenuator the power corresponding to the reading from the barrel of the attenuator was calculated. A chart of the compressed pulse is shown in Figure 4-11.

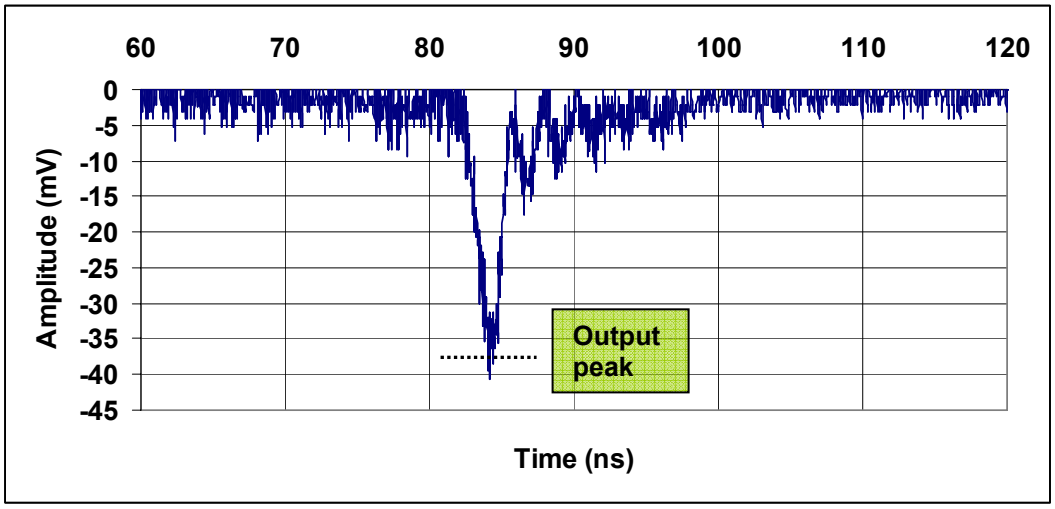

Figure 4-11 Measured rectified microwave compressed pulse.

The degree of adjustment on the variable attenuator corresponded to 14 dB. Converting from decibels (dB) to a power ratio the compression factor was calculated to be approximately 25. Location of the correct alignment position of the peak of the output pulse to the flat part of the input pulse on the DSO screen results in a reading error. The peak of the output pulse is fairly well defined however due to the power fluctuation of the RF input pulse establishing the measuring point was difficult. This resulted in an error associated with the adjustment of the variable attenuator of ± one half of the smallest division on the Barrel, [Squires 1997]. From the calibration chart of the variable attenuator this equates to an error of ± 0.49 dB (i.e. approx. 1dB).

4.4 PULSE COMPRESSION EXPERIMENTS AT kW POWERS

A schematic of the experimental set-up is shown in Figure 4-12 below for the kW power level microwave pulse compression experiments. A 7 kW conventional travelling wave tube amplifier (TWT) was used as the input to the 3-fold helically corrugated waveguide microwave pulse compressor. Additional instrumentation was required such as a bipolar pulse generator, a four channel digitising oscilloscope (Tektronix TDS 640A, 500 MHZ), a power isolator and a 10 dB directional waveguide coupling arm.

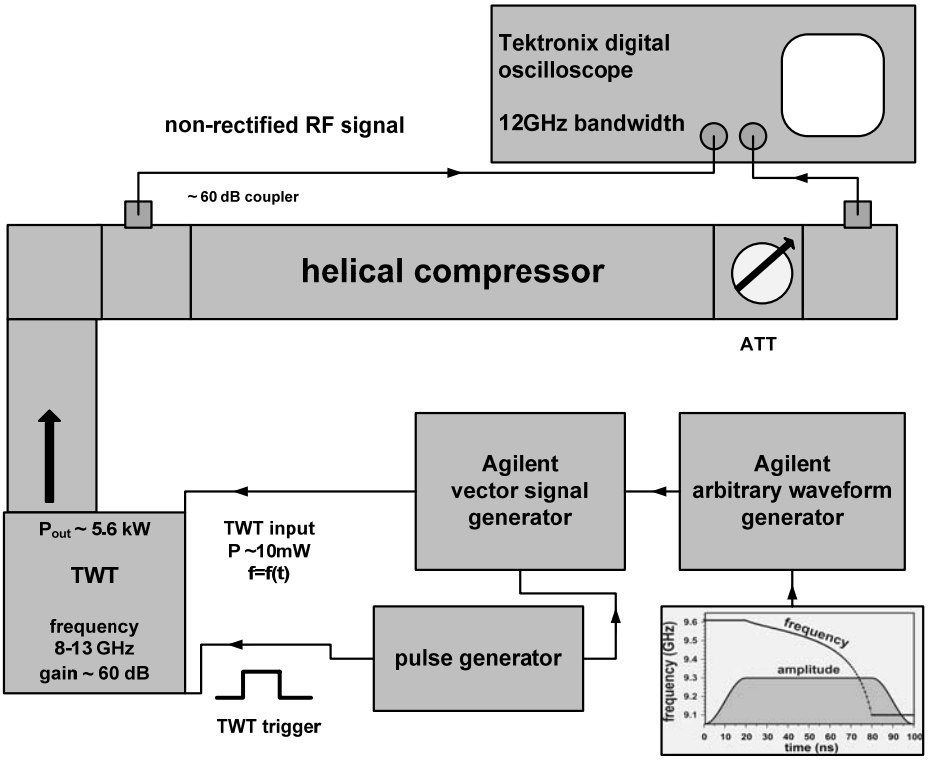

Figure 4-12 Schematic of experimental set-up for kW power level compression experiments.

The TWT is the device which provides the amplification of the low-power microwave signal from the VSG. The TWT was set to be active for a period of 1 μs and after 500 ns delay the frequency-swept microwave pulse was triggered from the AWG using the bipolar pulse generator, (Figure 4-13).

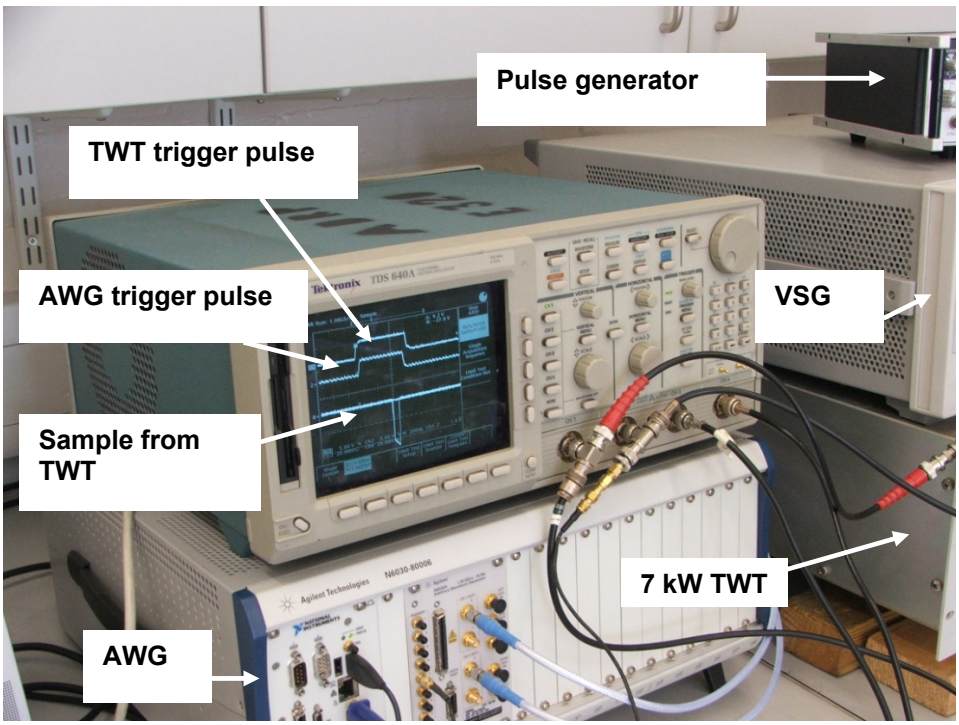

Figure 4-13 Digital photograph of trigger set-up for TWT to produce microwave kW microwave pulse for compressor.

Following this the VSG produced a 100 ns frequency-swept microwave pulse for compression which was the input to the TWT. The microwave pulse was amplified within the TWT due to a beam-wave interaction where energy is extracted from the electron beam within the TWT, [Benford 1992]. The amplified input microwave pulse to the 3-fold pulse compressor from the TWT was coupled through a series of waveguide connections to prevent any unwanted oscillations entering the TWT output port via reflections. Such waveguide connections included a power isolator which acted as a one way valve preventing any backward wave oscillations from entering the TWT driver instrumentation as shown in Figure 4-14.

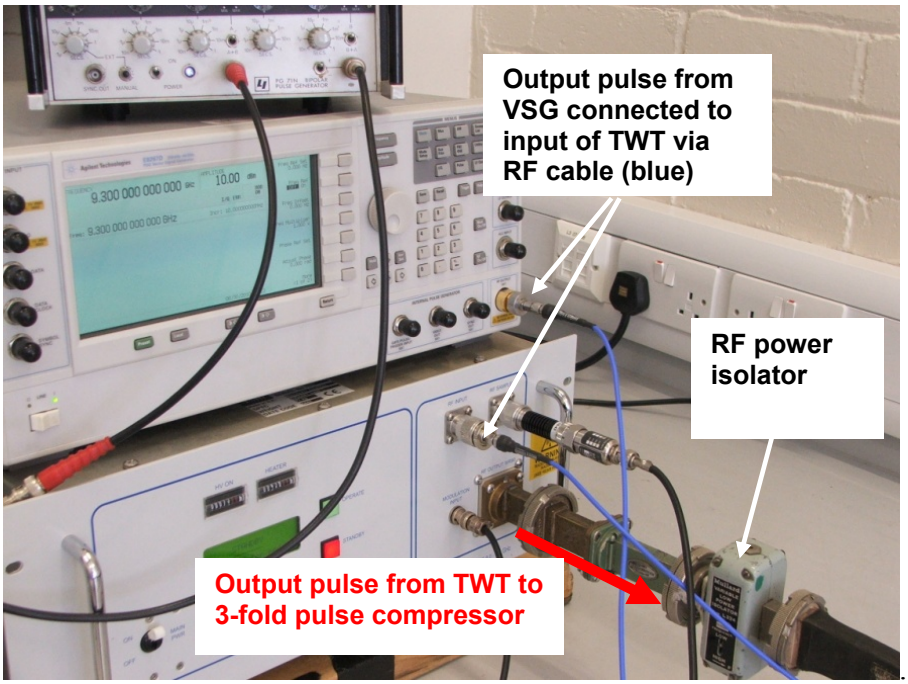

Figure 4-14 Digital photograph of TWT and RF isolator.

The complete experimental set-up for the 3-fold microwave pulse compression experiments is shown in Figure 4-15. The output pulse from the TWT which is the input pulse to the 3-fold microwave pulse compressor was propagated along the microwave compressor structure. By using a 10 dB directional waveguide coupler and a combination of attenuators (fixed and variable) the kW power levels of microwave pulses were attenuated to be safely measured on the 12 GHz Tektronix DSO.

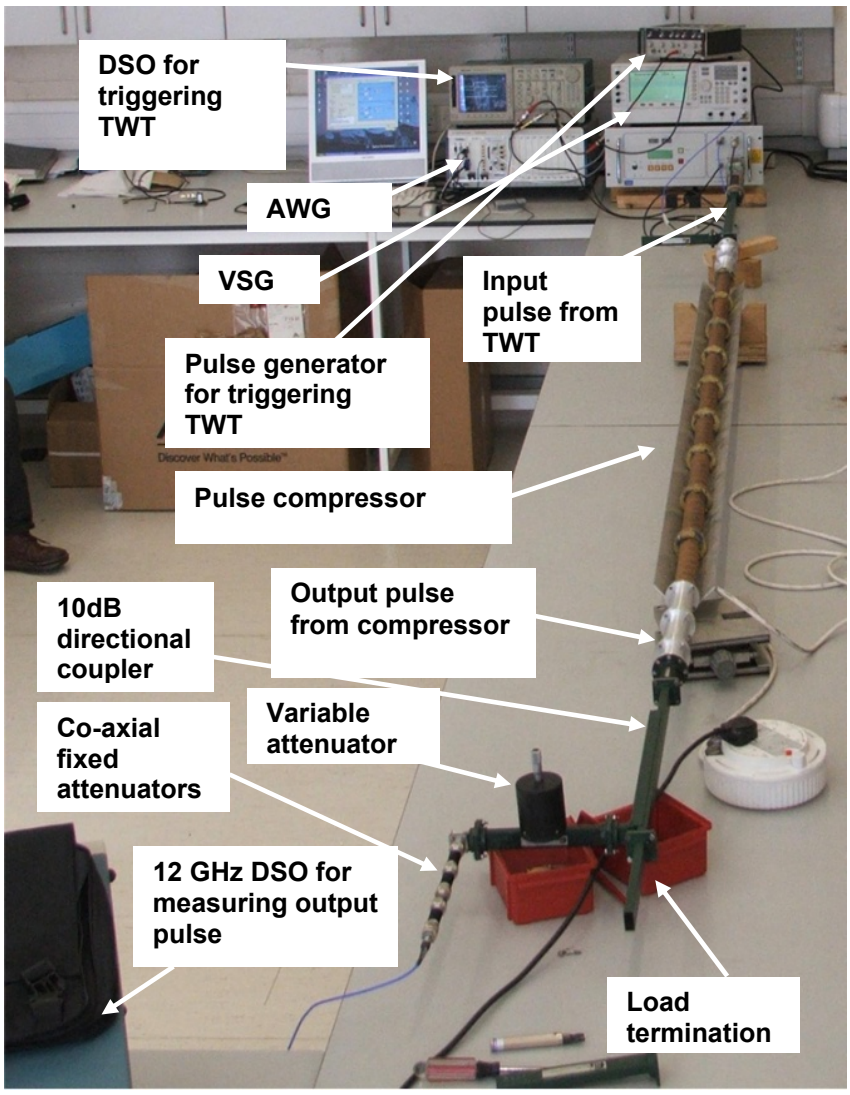

Figure 4-15 Digital photograph of experimental set-up in RF laboratory for kW pulse compression experiments.

4.4.1 Measurement of kW input and output (compressed) microwave pulses

The input pulse to the 3-fold microwave pulse compressor was measured on the 12 GHz DSO. As the pulse was in the kW power levels the signal had to be attenuated before entering the DSO. To achieve this, a 10 dB directional waveguide was used to couple 10 % of the signal power. This coupling arm was connected in series with fixed N-type co-axial attenuators and a calibrated sliding-vane microwave variable attenuator to have optimum control over the microwave signal to the DSO. The input microwave pulse was measured on the DSO (Figure 4-16 (top)) and the measured data of the pulse was used in a Matlab code [Appendix H] to measure the

frequency-sweep of the pulse, (Figure 4-16 (middle)). The input pulse data was also used to convert the a.c. pulse into a power envelope of the input pulse, (Figure 4-16 (bottom)).

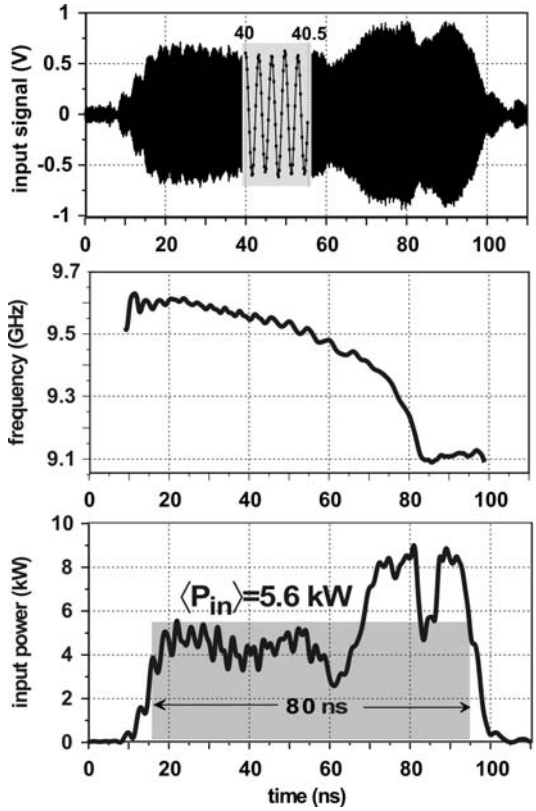

Figure 4-16 Input pulse details for kW microwave pulse compression experiment.

Although the TWT is a 7 kW travelling wave tube, the power output of the TWT is highly frequency dependent. The input pulse to the TWT has a frequency modulation which resulted in the variation of power distribution within the input pulse as it exits the TWT. The input pulse from the TWT was attenuated and measured on an Anritsu peak power meter, (Figure 4-17).

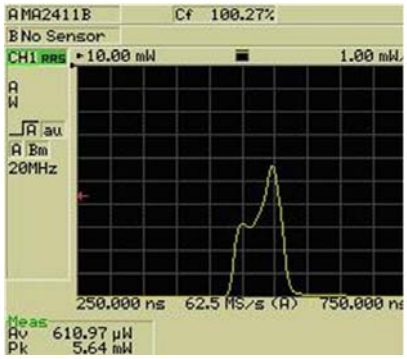

Figure 4-17 Measured input pulse from TWT using peak power meter.

The output microwave pulse from the compressor was measured on the 12 GHz DSO by attenuating down the compressed signal from the 3-fold helically corrugated waveguide output using a 10 dB directional coupler and load termination in conjunction with a series of co-axial attenuators and sliding-vane variable attenuator. The measured output pulse was converted to a power envelope as shown below in Figure 4-18.

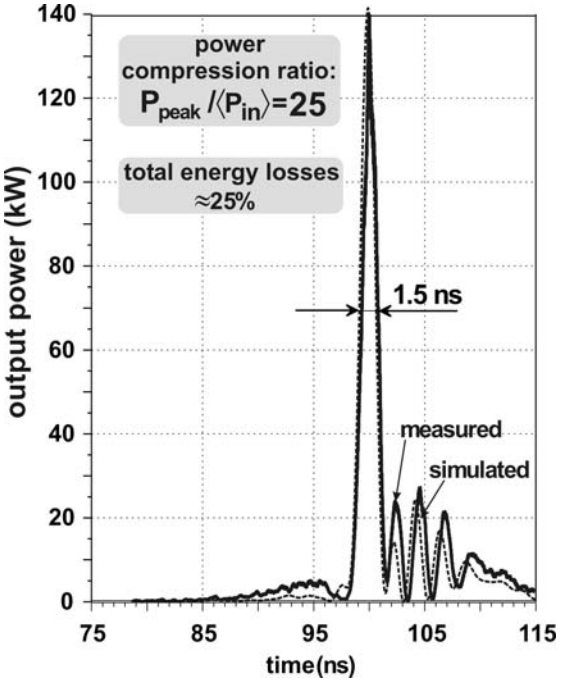

Figure 4-18 Power envelope of measured compressed pulse.

The peak output power (P_{peak}) was calculated to be 140 kW using the measured pulse data. The average power of the input pulse was calculated to be 5.6 kW from the measured input pulse data. The maximum peak power compression ratio was calculated to be 25, [McStravick 2010]. The time compression ratio was calculated as the ratio of the input pulse duration, 80 ns, to the compressed pulse duration at FWHM, 1.5 ns. This gives a time compression ratio of 53. Calculation of the ratio of the energy contained within the main body of the input pulse to the energy contained within the main body of the compressed pulse resulted in a compression efficiency of 42 ± 5 %.

4.5 METHOD OF ATTENUATION EXPERIMENT AT kW POWERS

In the same way as for the mW power level experiments the rectified input microwave pulse to the 3-fold pulse compressor and the rectified output (compressed) microwave pulse from the compressor were measured. Due to the kW power levels involved it was necessary for attenuation to be applied to control the signal entering the co-axial microwave crystal detector. The microwave signal from the crystal detector was fed into the input channel of the 12 GHz DSO. The rectified input pulse was measured as shown in Figure 4-19 below,

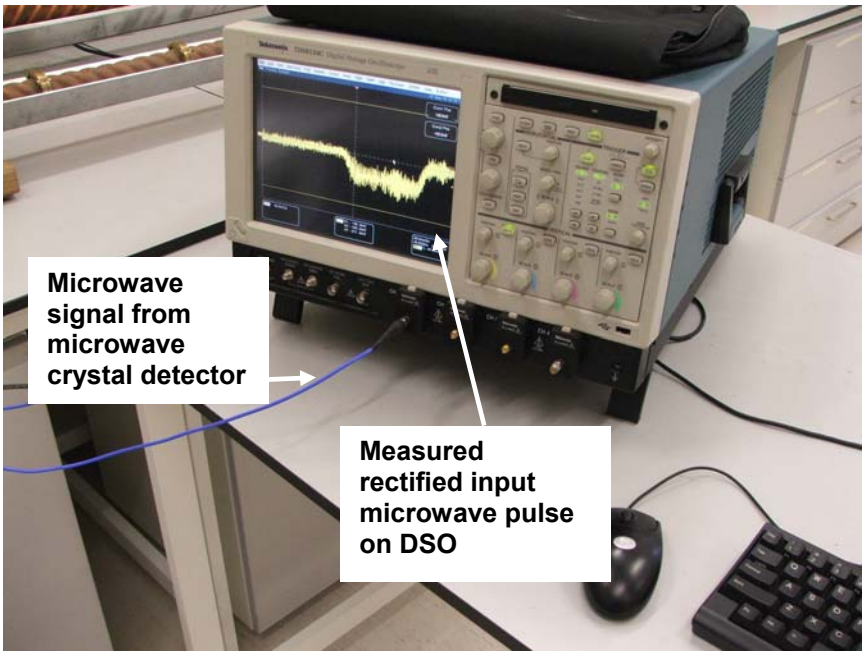

Figure 4-19 Digital photograph of a kW measured rectified input pulse from experiment using method of attenuation.

The measured input microwave pulse was saved into the memory of the DSO in order to align the peak of this input pulse with that of the compressed rectified microwave pulse using the calibrated sliding-vane microwave attenuator. The data of the rectified input pulse was transferred to Microsoft Excel. A plot of the rectified microwave input pulse is shown in Figure 4-20.

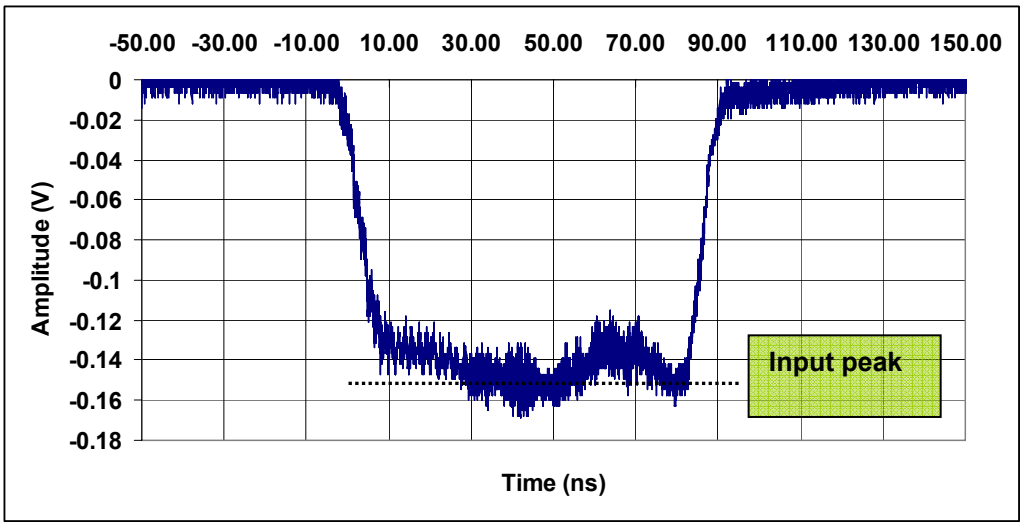

Figure 4-20 Measured rectified input pulse to compressor from TWT.

The microwave crystal detector was moved to the output of the compressor and positioned after a series of attenuators. The output signal (Figure 4-21) was measured on the DSO and the peak of the output aligned on the DSO screen with that of the input pulse. By adjustment of the barrel of the sliding-vane variable attenuator the peaks were aligned. The read-out from the barrel on the variable attenuator corresponded to a 14 dB change in attenuation using the calibration chart for the attenuator. This corresponds to a compression factor of approximately 25.

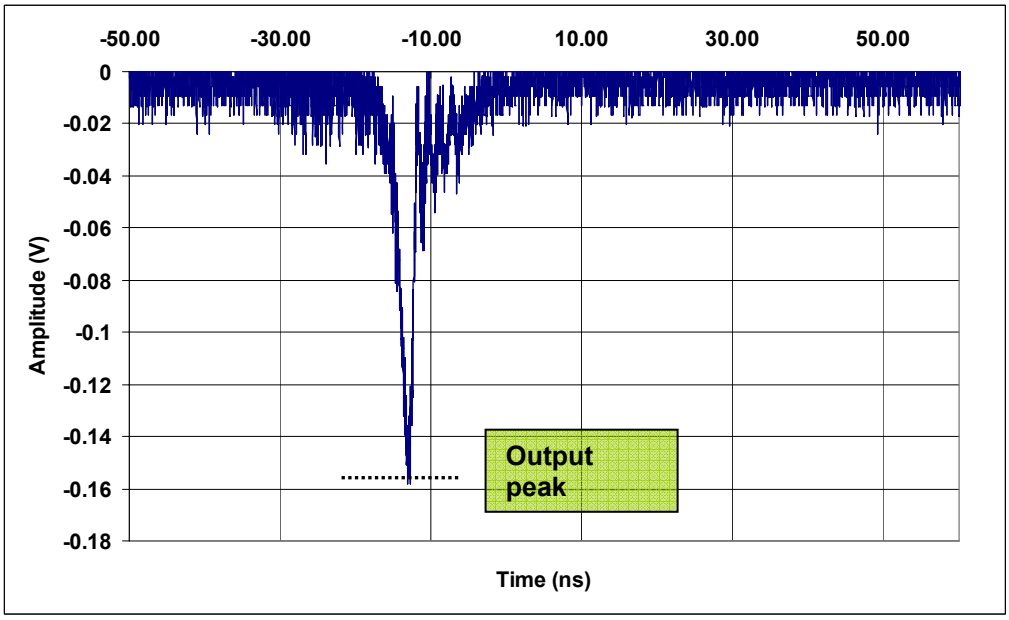

Figure 4-21 Measured rectified compressed microwave pulse.

From the low and high-power sweep-frequency microwave pulse compression experiments the pulse power compression factor matches well with the simulated results in terms of both the power compression factor and also the compressed pulse shape. The maximum power compression ratio measured was 25(13.5dB) ± 0.5dB. The losses within the waveguide can be attributed to ohmic losses, particularly in the upper range of the frequency sweep used for the input pulse in the compression experiments.

Chapter 5

The 5-Fold Helically Corrugated Waveguide

The chapter introduces the 5-fold copper helically corrugated waveguide. The design, manufacture and construction of a waveguide system based on a 5-fold helically corrugated waveguide geometry are presented. The dispersion characteristics of the 5-fold helically corrugated waveguide are reported using analytical, numerical and experimental techniques. The ohmic loss measurements of the 5-fold helically corrugated waveguide pulse compressor system are detailed. A simulation of the power compression ratio for an optimum frequency-sweep concludes the chapter.

5.1 INTRODUCTION

To achieve very high peak microwave powers the physical size of the waveguide transporting the microwave energy has to be large to prevent RF breakdown from occurring within the waveguide. A larger diameter waveguide based on a 5-fold helically corrugated structure was devised. The average diameter of the 5-fold helically corrugated waveguide (7.56 cm) was approximately 2 times larger than that of the 3-fold helically corrugated waveguide (2.94 cm) and as a result the waveguide can handle higher RF powers in the range of GW powers.

The 5-fold pulse compressor could be used in conjunction with a high-power amplifier such as a gyro-TWT or a relativistic BWO to achieve extremely high-power, short-duration (ns) microwave pulses.

5.2 DESIGN OF A 5-FOLD MICROWAVE PULSE COMPRESSOR

The 5-fold waveguide system was designed in collaboration with the Institute of Applied Physics in Russia. The system was designed to compress microwave pulses with frequency-modulation within the interval of 9.0 - 9.6 GHz and simultaneously provide low reflection of input radiation within frequency interval of 8 - 10 GHz. The waveguide system consists of an input cone to introduce the radiation from the input source, a mode converter to convert the input mode into the operating mode of the compressor [Thumm 1997], an intermediate cone to transport the radiation keeping acceptable mode purity and a 5-fold pulse compressor to compress the frequency-modulated radiation, (Figure 5-1).

The input microwave radiation entering the input cone will be in the form of a left-circularly polarised $TE_{1,1}$ mode. The output microwave radiation from the mode converter and entering the 5-fold compressor will be in the form of a right-circularly polarised $TE_{3,1}$ mode.

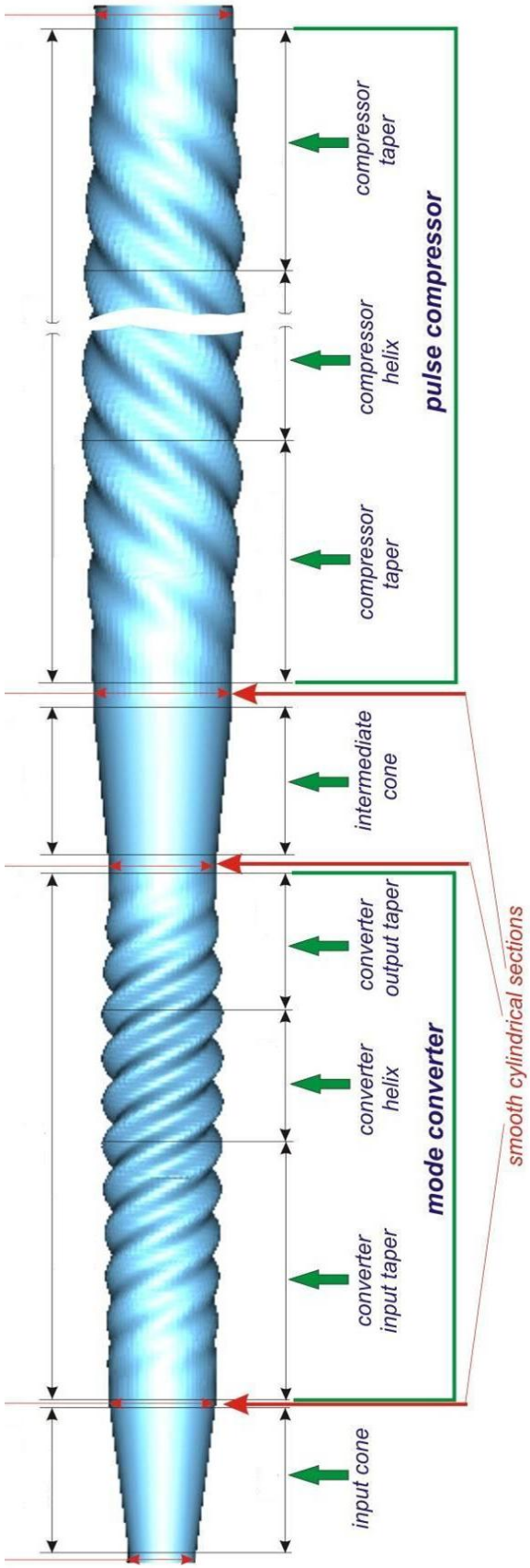

Figure 5-1 Schematic of 5-fold helically corrugated waveguide pulse compressor system.

Input Cone

The input cone was designed to transport the input $TE_{1,1}$ mode with high mode purity from the source to the mode converter and simultaneously serve as a cut-off microwave reflector for the $TE_{3,1}$ mode. The input cone has an input diameter of 3.0 cm, a larger output diameter of 4.76 cm and a length of 7.0 cm.

Mode Converter

The mode converter was designed to transform the microwave radiation from a left-circularly polarised $TE_{1,1}$ mode into a right circularly polarised $TE_{3,1}$ mode with sufficiently high-power conversion within the frequency band of 9.0 to 9.6 GHz and simultaneously possess low reflection for the $TE_{1,1}$ mode for frequencies in the region from 8 - 10 GHz.

The principle of the mode converter's operation was based on the resonant selective Bragg scattering by the periodic corrugation. In this case the helical corrugation provides scattering between the $TE_{1,1}$ and the $TE_{3,1}$ counter-propagating and counter-rotating modes. The incident $TE_{1,1}$ mode is resonantly (under Bragg conditions) reflected by the corrugation into the $TE_{3,1}$ circularly polarised mode. The backward propagated $TE_{3,1}$ mode is cut-off reflected from the input cone (without changing the direction of rotation) and radiates forward without resonant scattering on the corrugation.The mode converter consists of a converter input taper, a converter helix and a converter output taper. The equations for the corresponding surfaces in cylindrical co-ordinates are given by,

Mode converter input taper

$$r = r_0 + \frac{lz\sin\left(\frac{2\pi z}{d} - 4\phi\right)}{6d} \qquad \textbf{Equation 5-1}$$

Equation 5-1 gives a 4-fold right-handed helical corrugation with mean radius (r_0), period (d), amplitude of sinusoidal corrugation linearly increasing from zero to l and length of $6d$ for $z = 0 \rightarrow 6d$.

Mode converter helix

$$r = r_0 + l\sin\left(\frac{2\pi z}{d} - 4\phi\right) \qquad \textbf{Equation 5-2}$$

Equation 5-2 gives a 4-fold right-handed helical corrugation with mean radius (r_0), period (d), constant amplitude of sinusoidal corrugation of l and length of $3d$ for $\mathrm{z} = 0 \rightarrow 3\mathrm{d}$

Mode converter output taper

$$r = r_0 + \frac{lz\sin\left(\frac{2\pi z}{d} - 4\phi\right)}{3d} \qquad \textbf{Equation 5-3}$$

Equation 5-3 gives a 4-fold right-handed helical corrugation with mean radius (r_0), period (d), amplitude of sinusoidal corrugation linearly increasing from zero to l and length of $3d$ for $\mathrm{z} = 0 \rightarrow 3\mathrm{d}$.

The values for the mode converter input taper, the helix and the output taper where given by, $r_0 = 2.38$ cm, $d = 2.0$ cm and $l = 0.309$ cm.

Intermediate Cone

The Intermediate cone was designed to transport the $TE_{3,1}$ mode with high mode purity from the mode converter to the pulse compressor section. It has an input diameter of 4.76 cm, an output diameter of 6.146 cm and a length of 7.0 cm.

Input cone, Mode converter, and Intermediate cone

The input cone, mode converter and intermediate cone were constructed as a model in CST MWS using VBA macros for each section. The CST MWS model is shown in Figure 5-2,

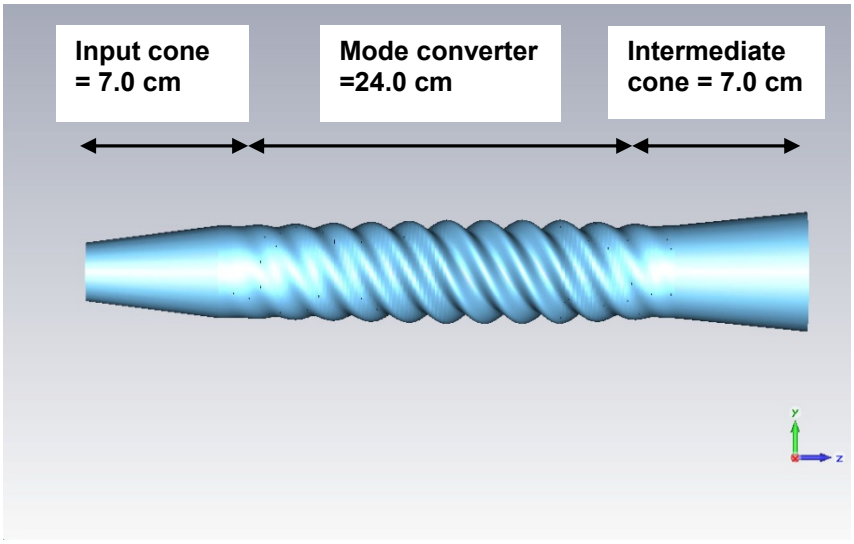

Figure 5-2 Model of input cone, mode converter and intermediate cone created using CST MWS.

To establish that the input section to the pulse compressor would operate properly a transient solver simulation was performed to measure the purity of the mode conversion. The transient solver within CST MWS allowed for a simulated linearly polarised $TE_{1,1}$ mode to be injected into the input port of the input cone. An elliptical polariser was created in CST MWS to transform the linearly polarized $TE_{1,1}$ mode into a left-circularly circularly polarised $TE_{1,1}$ mode, (Figure 5-3).

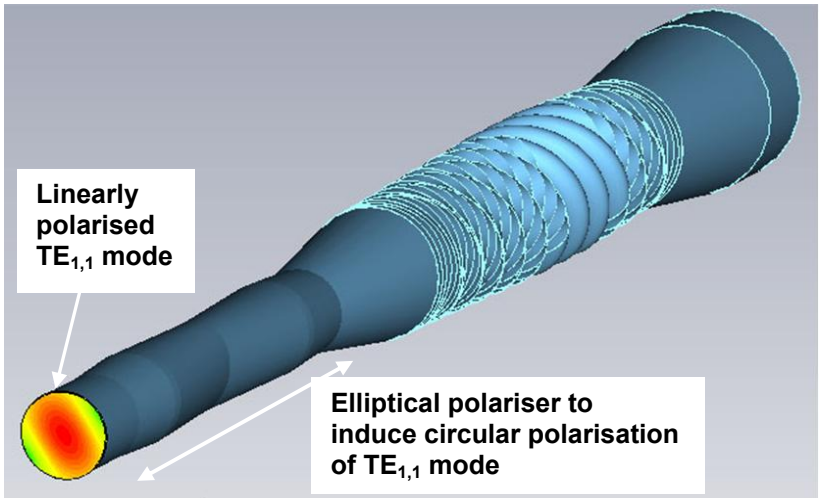

Figure 5-3 Simulation of input mode to the mode converter.

Field monitors were positioned through out the waveguide structure to monitor the transient mode, [CST MWS 2009]. The output port was positioned at the end of the intermediate cone. The field monitor showed the right-circularly polarised $TE_{3,1}$ mode (Figure 5-4).

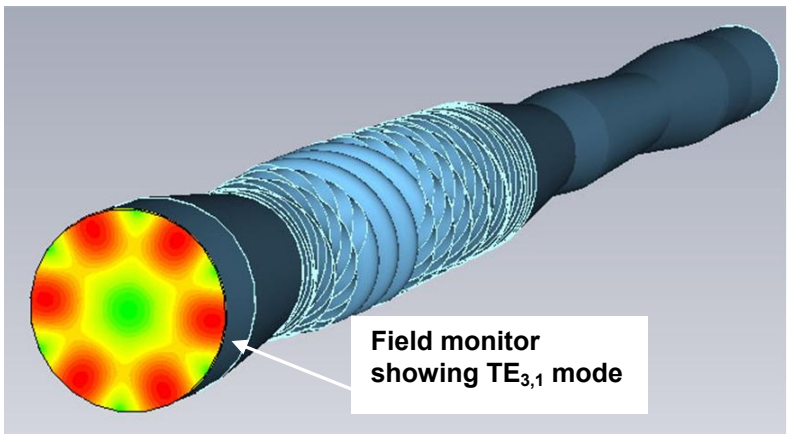

Figure 5-4 Simulation of the output mode from the mode converter.

The data from the field monitor, positioned at the output of the mode converter, was used to determine the forward-transmission (S_{21}) and reflection (S_{11}) properties for the modes. The $TE_{1,1}$ mode is successfully converted to the $TE_{3,1}$ mode within the mode converter. Approximately 99% of $TE_{3,1}$ mode being transmitted in the mode converter over the frequency band of 9.0 -10.0 GHz was converted. The reflection S_{11} parameter for the $TE_{1,1}$ mode is less than one percent, (Figure 5-5).

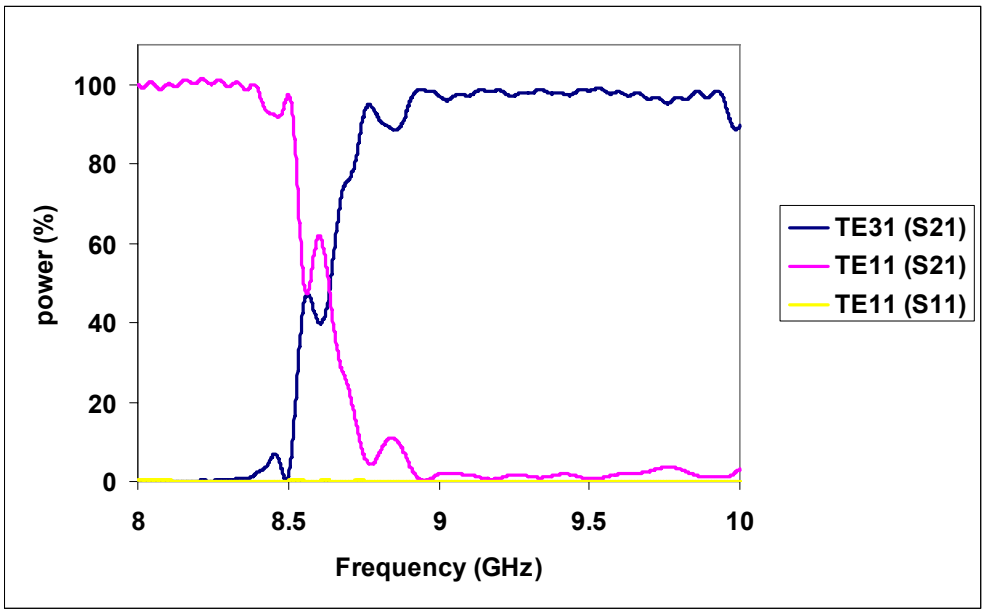

Figure 5-5 The S-parameters measured using CST MWS at output of the mode converter.

The 5-Fold Microwave Pulse Compressor

The principle of its operation is based on the resonant selective coupling of two waveguide modes by the periodic corrugation, [Burt 2004, Samsonov 2004]. In this case the 5-fold helical corrugation provides coupling between $TE_{2,2}$ near-cutoff mode and the $TE_{3,1}$ fast-travelling counter-rotating mode. As a result of this coupling an eigenmode of the periodically corrugated waveguide appears which has a strong dispersion of its group velocity and is used as an operating mode of the 5-fold compressor helix.

The compressor input taper was designed to transform incident radiation in the form a $TE_{3,1}$ circularly polarised mode into the operating mode of compressor helix while the compressor output taper transforms the output radiation back into the $TE_{3,1}$ circularly polarised mode of a circular waveguide. In this design both the compressor tapers are identical while their parameters (length and mean radius tapering) were optimised to ensure high conversion efficiency for frequencies 9.0 to 9.6 GHz and good matching with an input source (sufficiently low reflection) for frequencies in the region of 8.0 to 10.0 GHz.

The equations for the surfaces of the compressor components are given by,

Compressor helix

$$r = r_0 + l\sin\left(\frac{2\pi z}{d} + 5\phi\right) \qquad \textbf{Equation 5-4}$$

Equation 5-4 gives a 5-fold left-handed helical corrugation with constant mean radius (r_0), corrugation of period (d), constant amplitude of sinusoidal corrugation, (l) . The values for the 5-fold compressor helix are shown below in Table 5-1.

Waveguide parameter	Value
r_0	3.284 cm
l	0.243 cm
d	3.326 cm
m_B	-5
$k_B = 2\pi/d = 2\pi/3.326$	1.89 cm^{-1}

Table 5-1 The 5-fold helically corrugated waveguide parameters.

The compressor helix section has a length of N_c periods where $z = 0 \rightarrow N_c d$

Compressor taper

$$r = r_{in} + \frac{(r_0 - r_{in})z}{3d} + \frac{lz\sin\left(\frac{2\pi z}{d} + 5\phi\right)}{3d} \qquad \textbf{Equation 5-5}$$

Equation 5-5 gives a 5-fold left-handed helical corrugation with mean radius linearly increasing from r_{in} to r_0, period of d, amplitude of sinusoidal corrugation linearly increasing from zero to l and length of $3d$ for $z = 0 \rightarrow 3d$.

The values for the compressor helix and compressor taper are given by,
$r_{in} = 3.073$ cm $r_0 = 3.284$ cm, $d = 3.326$ cm, $l = 0.243$ cm.

5.3 MANUFACTURE AND CONSTRUCTION OF WAVEGUIDES

The starting point of the manufacturing process was to manufacture the waveguide compressor parts. Within the Atoms, Beams and Plasmas group at the University of Strathclyde a 4-axis computer numerically controlled (CNC) milling machine was used to cut the helical waveguide shapes. The 5-fold waveguide system was approximately 3 m in length and so each part of the system had to be made in turn on the CNC. The dimensions and parameters of the 5-fold helical profile were uploaded into the CNC software. An aluminium former was secured onto the CNC and the cutter followed the tool-path governed by the uploaded code. The 4-axis CNC machine allowed movement in the left-right, up-down, backwards-forwards directions and rotation about its axis. As the machine cut, the cutter-tip was being constantly cooled by a coolant fluid, Figure 5-6 below,

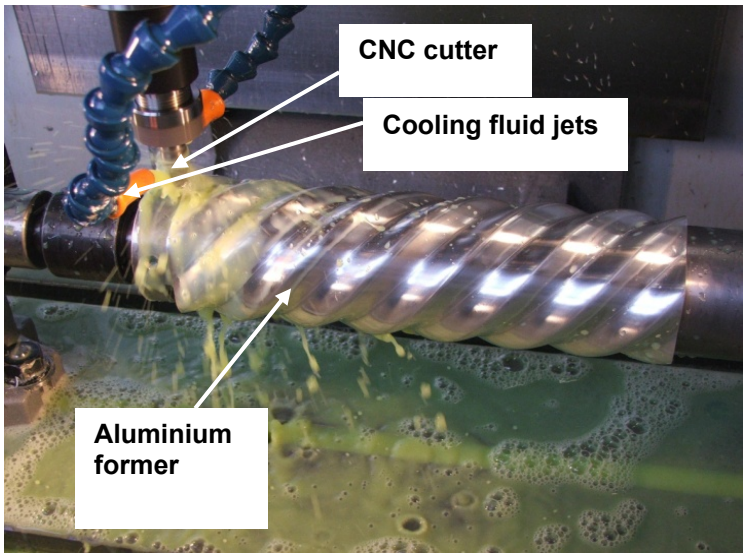

Figure 5-6 Digital photograph of CNC machine cutting 5-fold helical shape on aluminium former.

The cutting process started with a rough-cut and was repeated until the waveguide shape matched that of the specification of the finished-cut. The result was the aluminium mandrels. Below is the first set of aluminium mandrels of the waveguide compressor components having been machined on the CNC mill (Figure 5-7a). The next step in the manufacturing process was to have a thick layer (8 mm) of copper deposited on top of the aluminium mandrels by a process of electro-form deposition (Figure 5-7b). The electro-form deposition was performed at a specialist site.

(a)

(b)

Figure 5-7 Machined waveguide pieces: (a) aluminium mandrels and (b) after electroform copper deposition.

The aluminium mandrel was removed from the deposited copper by a dissolving process, which was carried out off-campus at the same site where the electroform deposition occurred. The resultant copper waveguide components are shown in (Figure 5-8).

(a)

(b)

(c)

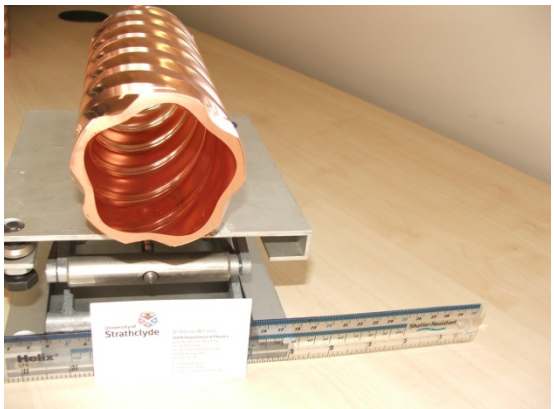

(d)

Figure 5-8 The finished waveguide pieces; (a) waveguide system components (b) intermediate cones and tapers (c) input cone and mode converter (d) regular 5-fold compressor section.

Due to the physical length of the 5-fold waveguide pulse compressor system the waveguide components had to be machined in parts. To connect each waveguide section a combination of waveguide flanges, collars and split-rings was devised, (Figure 5-9).

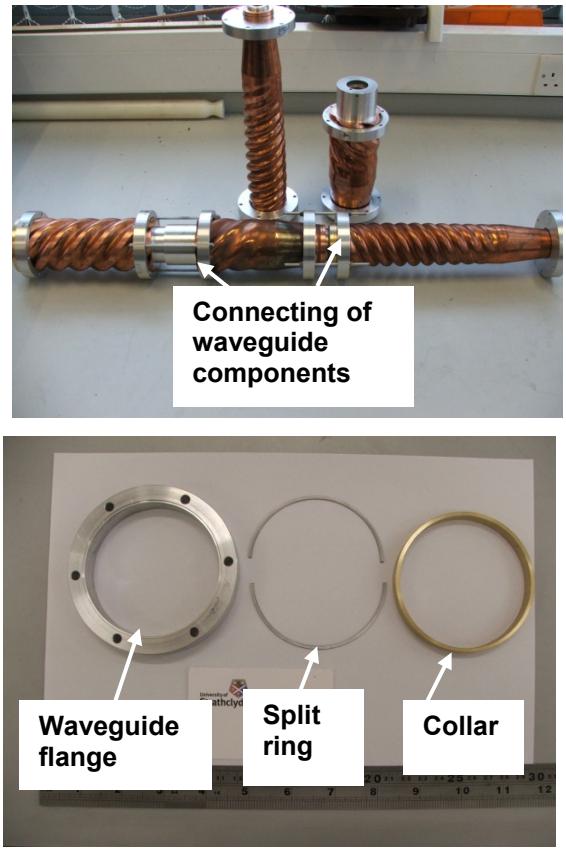

Figure 5-9 The 5-fold pulse compressor waveguide connection pieces.

5.4 EIGENWAVE DISPERSION CALCULATED ANALYTICALLY

The dispersion of the 5-fold helically corrugated waveguide eigenwave can be described using coupled wave theory, [Cooke 1998, Denisov 1998]. A Matlab code (Appendix D) based on the physics of coupled wave theory was constructed to solve for the dispersion equation of equation 2-66.

$$\left(k^2 - k_z^2 - k_{\perp 1}^2\right)\left(k^2 - \left(k_z - k_B\right)^2 - k_{\perp 2}^2\right) = 4\kappa^2 k_0^4$$

Expanding the dispersion equation results in a fourth order polynomial

$$k^4 - k^2\left[\left(k_z + k_B\right) + k_{\perp 2}^{\ 2} + k_{\perp 1}^{\ 2} + k_z^2\right] + \left(k_z^2 + k_{\perp 1}^{\ 2}\right)\left[k_{\perp 2}^{\ 2} + \left(k_z + k_B\right)^2 - \kappa^2\right] = 0$$

Using the Matlab code the equation was solved to find the roots of k. The appropriate waveguide parameters were inserted into the Matlab code. The values for the waveguide geomerty of the the 5-fold were taken from Table 5-1. The values for the Bessel function roots for the $TE_{2,2}$ wave and the $TE_{3,1}$ wave are 6.706 and 4.201. These values were taken from Table 2-2 in Chapter 2 of this thesis.

```
% Waveguide geometry
r0 = 3.284*cm;   % average radius of waveguide
r1 = 0.243*cm;   % corrugation depth of waveguide
 d = 3.326*cm;   % period

% Azimuthal components
m1 = 2;          % azimuthal component for TE2,2 wave
m2 = -3;         % azimuthal component for TE3,1 wave

% Roots of Bessel function
Z1 = 6.706;      % Bessel function root for TE2,2 wave
Z2 = 4.201;      % Bessel function root for TE3,1 wave
```

$k_{\perp 1}$ is the cut-off wave number of the $TE_{2,2}$ mode (In the Matlab code this is given by k1) and $k_{\perp 2}$ is the cut-off wave number for the $TE_{3,1}$ mode, (In the Matlab code this is given by k0). These cut-off values are calculated from the corresponding roots of the Bessel function and the average radius of the waveguide $r_0 = 3.284cm$, in the following relation:

$$k_{\perp 1} = \frac{6.706}{3.284} = 2.04 \text{ cm}^{-1}$$

$$k_{\perp 2} = \frac{4.201}{3.284} = 1.28 \text{ cm}^{-1}$$

The axial Bragg periodicity vector, k_B, was calculated using the value for the longtitudinal period of the corrugation $d = 3.326cm$, which resulted in a value for k_B given by

$$k_B = \frac{2\pi}{3.326} = 1.89 \text{ cm}^{-1}$$

The coupling coefficient κ was calculated using equation 2-67:

$$\kappa = \frac{l}{2r_0^3 k_0^2} \frac{S_1^2 S_2^2 - m_1 m_2 r_0^2 \left(k_0^2 + k_{z1} k_{z2}\right)}{\sqrt{\left(S_1^2 - m_1^2\right)\left(S_2^2 - m_2^2\right)}}$$

Where $S_1 = 6.706$, and $S_2 = 4.201$ which are the Bessel function roots for the $TE_{3,1}$ and $TE_{2,2}$ modes respectively, l is the corrugation amplitude, $l = 0.243cm$, m_1 is the azimuthal number of the $TE_{2,2}$ mode and m_2 is the azimuthal number of the $TE_{3,1}$

k_{z1} and k_{z2} are the axial wavenumbers of the $TE_{3,1}$ and $TE_{2,2}$ modes, respectively These are calculated as follows:

$$k^2 = k_{\perp 1}^{\ 2} + k_z^2$$

$$k^2 = k_{\perp 2}^{\ 2} + \left(k_z + k_B\right)^2$$

$$k_{z1} = -\left(\frac{k_{\perp 1}^{\ 2} - k_{\perp 2}^{\ 2} - k_B^2}{2k_B}\right)$$

$$k_{z2} = k_B - k_{z1}$$

k_0 is the wavevector of exact Bragg resonance. It is the intersection point of the coupled waves and is given by

$$k_0 = \sqrt{k_{\perp 2}^{\ 2} + k_{z1}^{\ 2}}$$

By executing the Matlab code of Appendix D a chart is produced of the frequency against axial wave number, Figure 5-10 below.

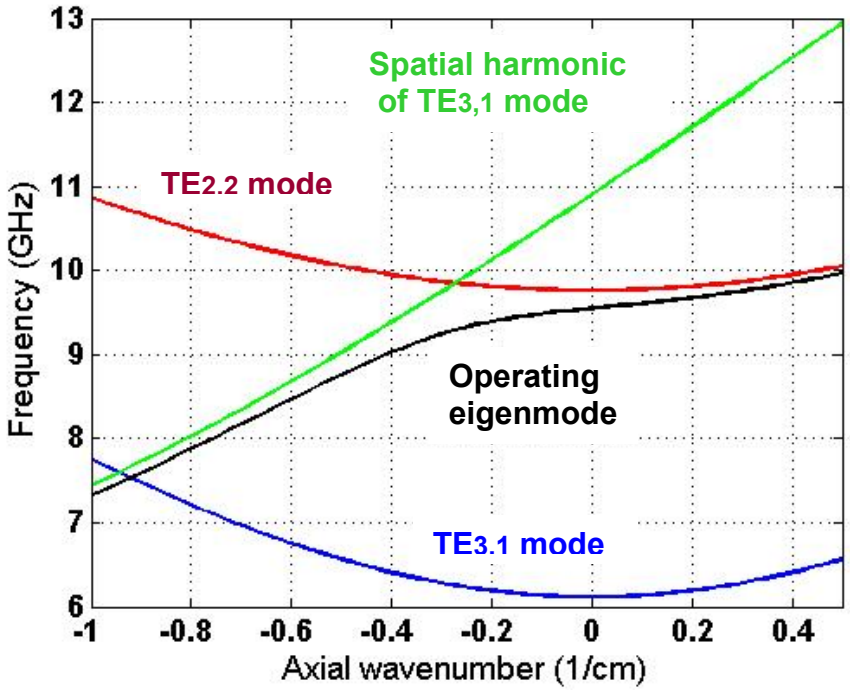

Figure 5-10 Dispersion diagram for 5-fold helically corrugated waveguide calculated by coupled wave theory using Matlab code.

From Figure 5-10 an operating eigenwave is produced which is the result of the resonant coupling of the first spatial harmonic of the $TE_{3,1}$ and the close to cut-off $TE_{2,2}$ mode. The data from the eigenwave was transferred from the Matlab program to Microsoft Excel, Figure 5-11.

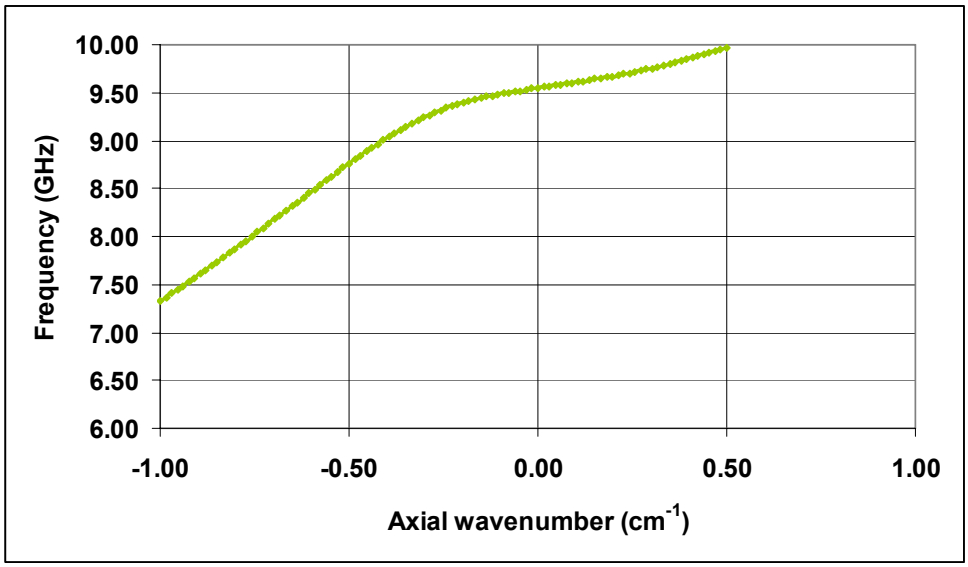

Figure 5-11 Eigenwave dispersion calculated analytically using coupled wave theory data.

The group velocity dispersion was calculated by taking the derivative of the best fit trend line, which was a 6th order polynomial function. The group velocity normalised to the speed of the electromagnetic wave in vacuum was plotted against the corresponding frequency, (Figure 5-12).

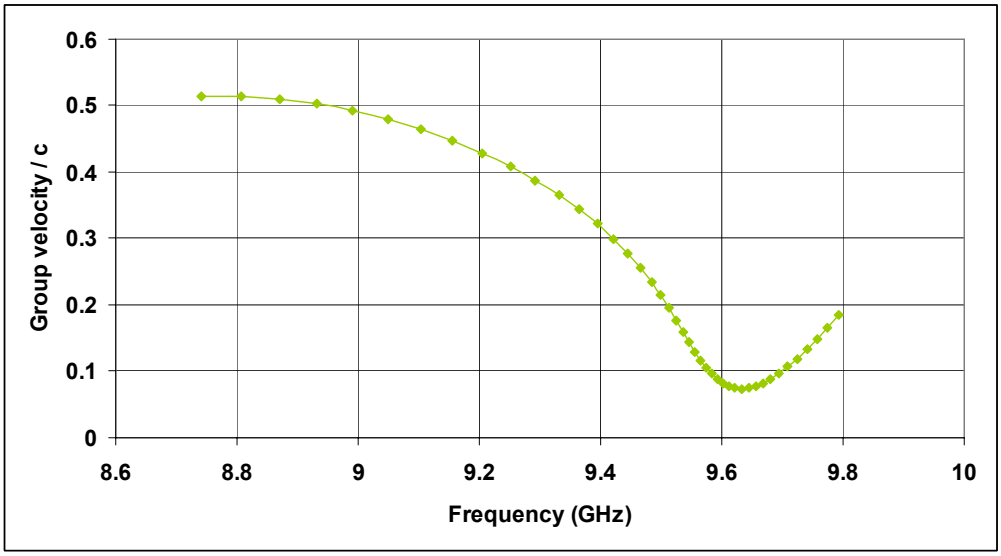

Figure 5-12 Group velocity chart calculated from analytical eigenwave dispersion data of coupled wave theory.

5.5 EIGENWAVE DISPERSION CALCULATED NUMERICALLY

Using the profile equation for the 5-fold geometry of regular helix (Equation 5-4) a single-period of helical corrugation of length $d = 3.326$ cm, was modelled in CST MWS. This was achieved by creating a macro in VBA (Appendix E) to outline the face of the 5-fold helical waveguide, (Figure 5-13a). Using the software tools within the GUI of CST MWS the face outline was twisted by 360˚/5 = -72˚ (the negative sign ensures a left-handed twist of the helical geometry) and extruded in length by 3.326 cm (Figure 5-13b).

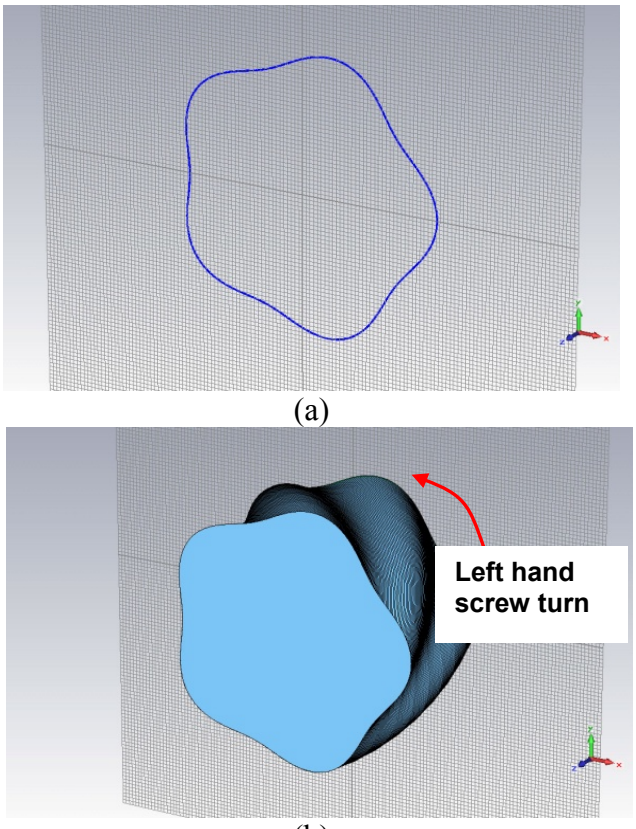

(a)

(b)

Figure 5-13 (a) 5-fold face outline and (b) single period of 5-fold helically corrugated waveguide created using CST MWS.

Using the dedicated eigenmode solver within CST MWS the boundary phase-shift angle (θ), was stepped in 5.0˚ intervals from -180˚ to 180˚ and the eigen-frequencies determined. The eigenwave was a coupling of $TE_{2,2}$ and $TE_{3,1}$ modes. The electric and magnetic field components of the eigenmode are shown in Figure 5-14

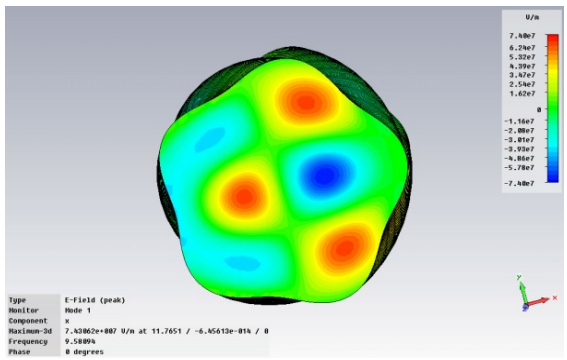

(a)

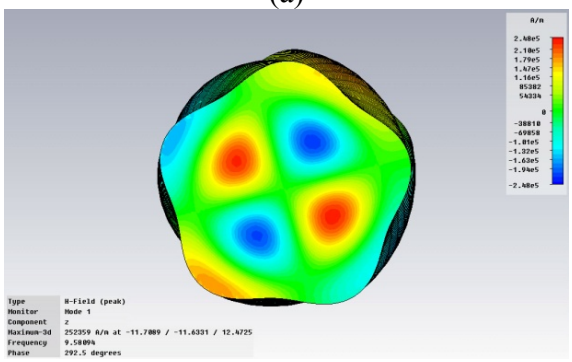

(b)

Figure 5-14 Eigenmode for 5-fold helix; (a) electric field and (b) axial magnetic field.

For each variation of the boundary phase shift angle, θ the corresponding axial wavenumber was calculated from $k_z = \theta/d$, where d is the corrugation period. A chart of the eigen-frequency with axial wavenumber was produced (Figure 5-15) giving the eigenwave dispersion for the 5-fold helically corrugated waveguide.

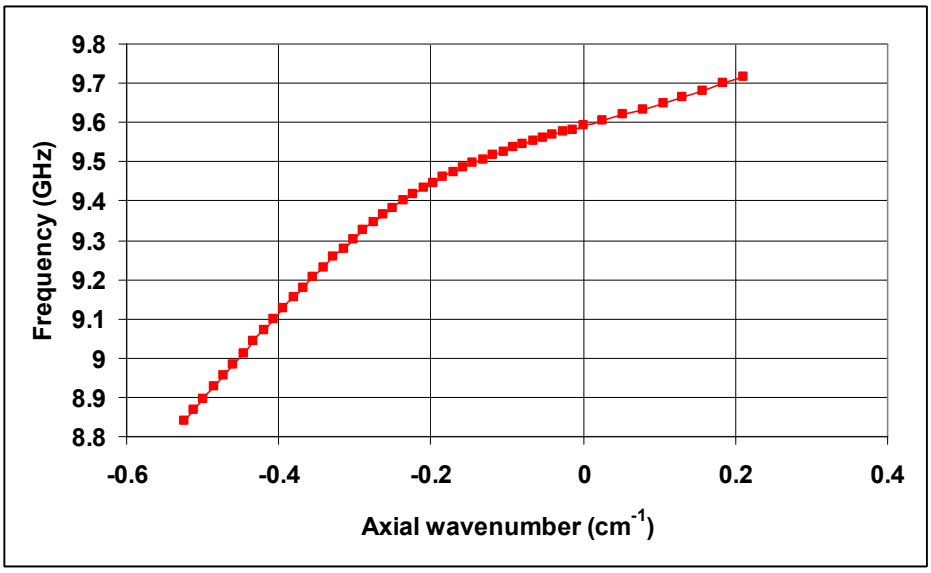

Figure 5-15 Eigenwave dispersion chart using CST MWS data.

From the eigenwave dispersion plot of Figure 5-15 the corresponding group velocity dispersion was calculated in Microsoft Excel, (Figure 5-16).

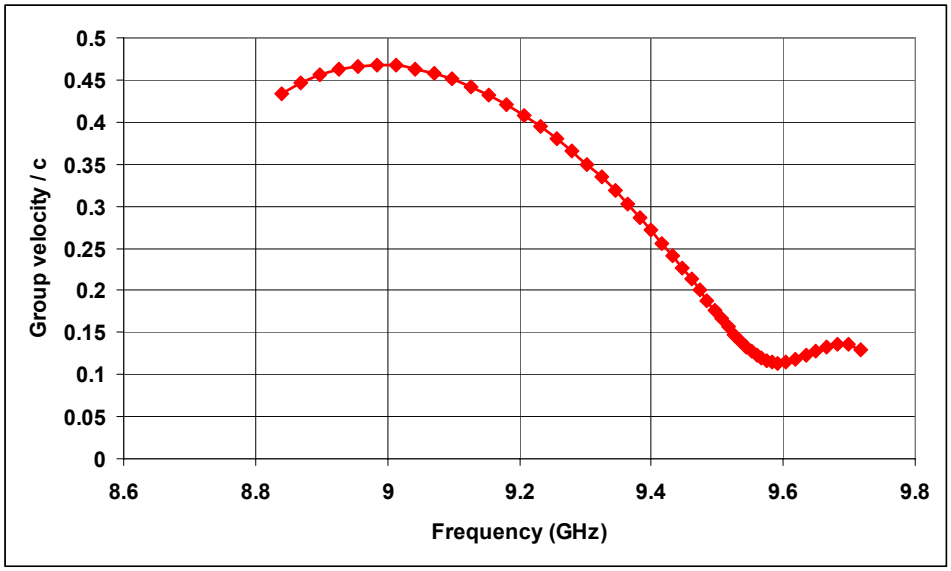

Figure 5-16 Eigenwave group velocity chart using CST MWS data.

5.6 EIGENWAVE DISPERSION CALCULATED EXPERIMENTALLY

In this experimental technique an Anritsu VNA was used to measure the phase response as a function of frequency [Anritsu 2007]. By measuring the phase difference $\Delta\varphi$ the axial wavenumber k_z for the operating eigenwave was determined in a length of helically corrugated waveguide L using $\Delta\varphi = k_z L$ The experimental set-up is shown in Figure 5-17. Due to the physical size of the compressor additional waveguide pieces were required for the connection to the VNA leads to be achieved.

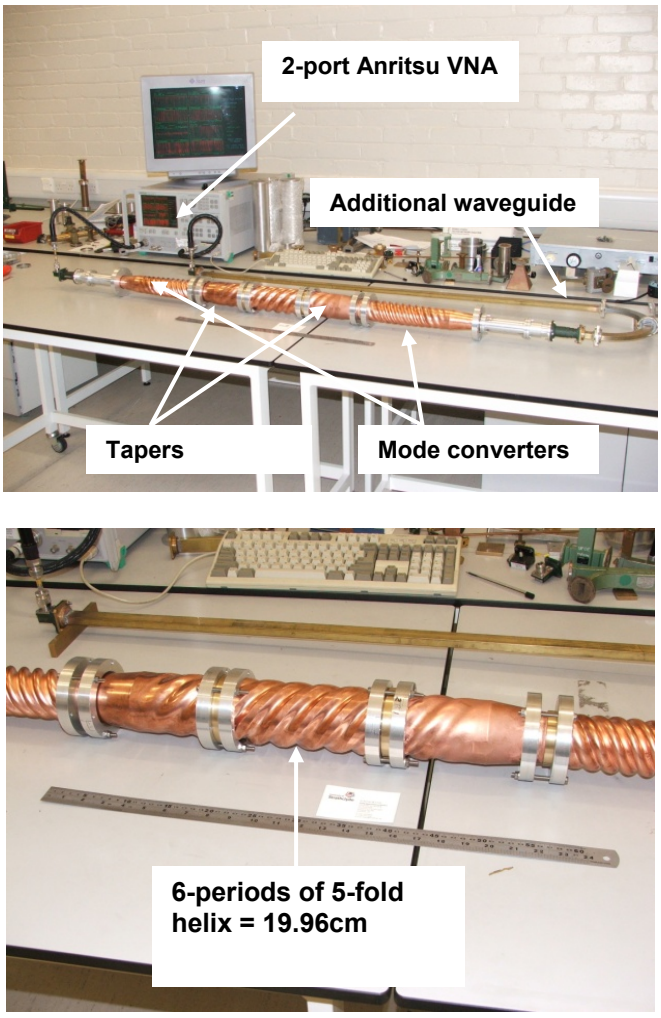

Figure 5-17 Digital photograph of experimental set-up in RF laboratory.

The 2-port VNA was calibrated using a line-reflect-line (LRL) calibration type with 12-terms excluding isolation, [Anritsu 2007]. The frequency range of the calibration was taken from 9GHz to 10 GHz and using the maximum data points of 1601. The

calibration planes were taken to be the ends of the co-axial-to-rectangular waveguide adapters. The DUT was a 6-period section of 5-fold compressor helix with a length of 19.96 cm. To excite the necessary parts of the waveguide system a $TE_{1,1}$ left circularly polarised wave was present by using the correct orientation of the elliptical polarisers. The $TE_{1,1}$ left-circularly polarised wave enters the mode converter and exits the converter as a $TE_{3,1}$ right-circularly polarised wave which then enters the intermediate cone and up-taper 5-fold helix and main body of the compressor helix.

With the 6-period section of compressor helix in place a measurement of the S_{21} transmission parameter was recorded. Another measurement was recorded with the 6-period section of compressor helix removed. From these two experimental measurements of the transmission properties with the helix in place and with it removed the dispersion characteristics of the 5-fold helix can be calculated by taking the difference of the two measurements. The raw phase data of the S_{21} measurements from the VNA is shown in Figure 5-18.

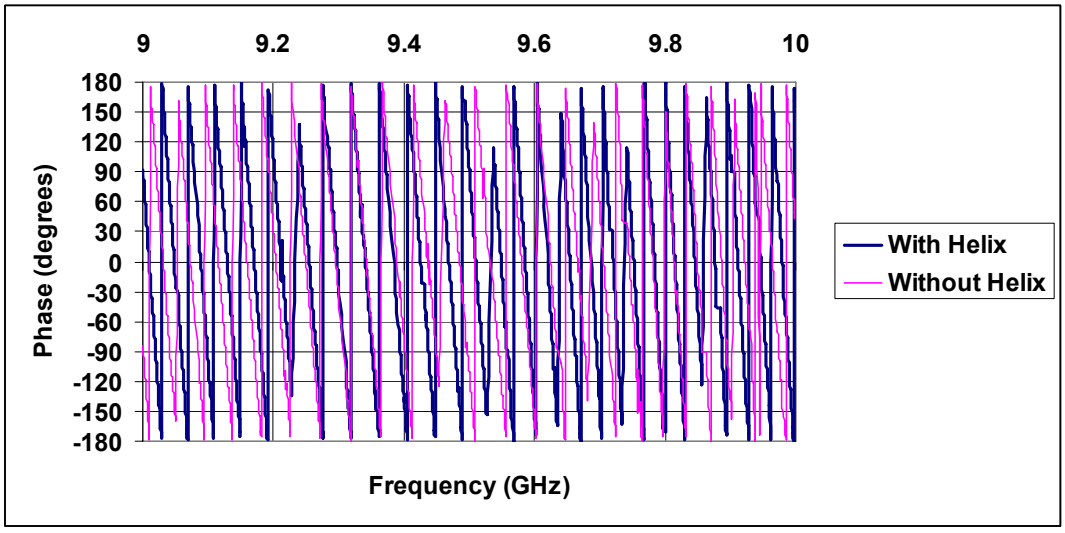

Figure 5-18 Chart of measured phase on VNA.

By digitally processing the data in Microsoft Excel the 360˚ phase jumps were removed, Figure 5-19.

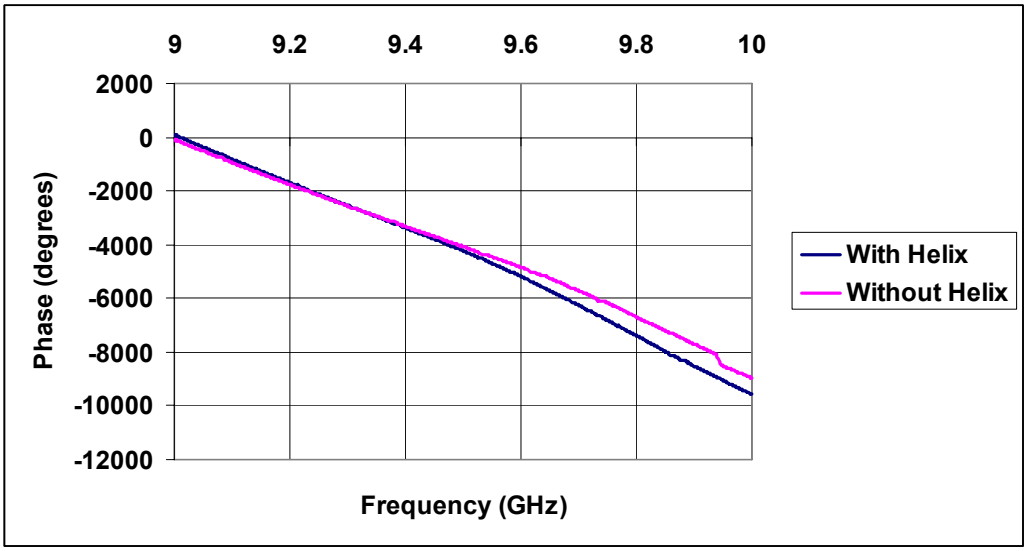

Figure 5-19 Chart of phase after digital processing to remove phase jumps.

Taking the length of 5-fold helically corrugated waveguide section to be 19.96 cm and using the transmission data the axial wave numbers k_z were calculated. The resultant dispersion curve is shown in Figure 5-20.

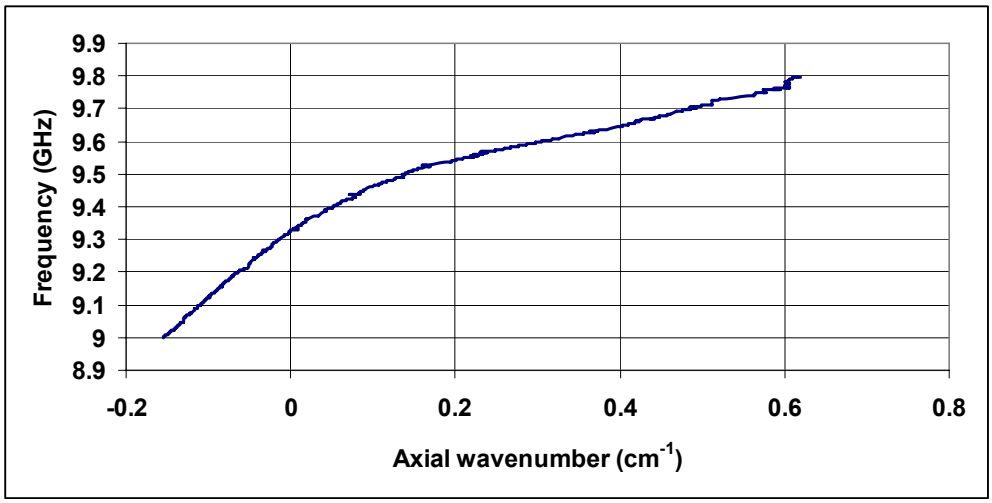

Figure 5-20 Eigenwave dispersion chart from measured VNA data.

A best-fit trend line was applied to the dispersion curve of Figure 5-20. This best-fit trend line is a polynomial. Taking the derivative of the polynomial allows for the group velocity dispersion to be calculated, Figure 5-21.

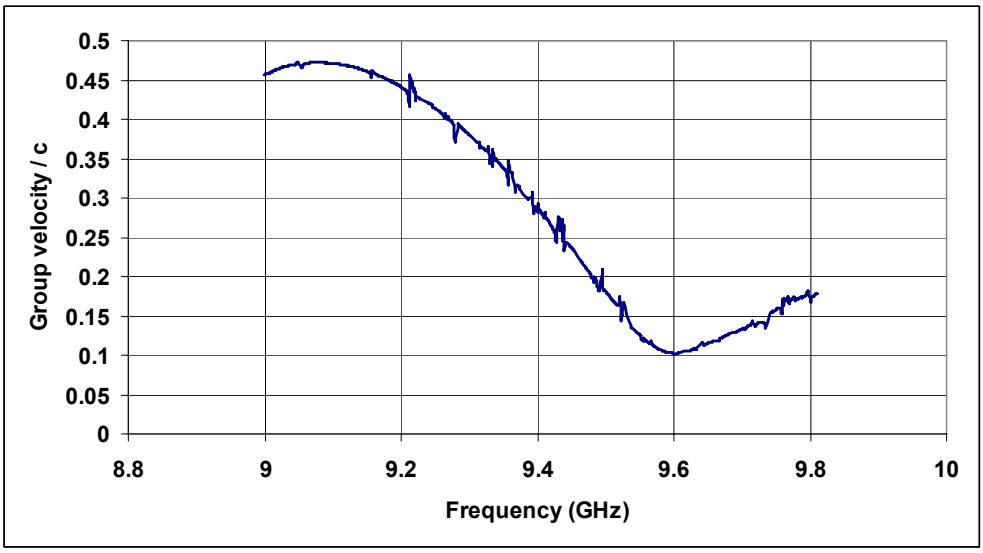

Figure 5-21 Group velocity dispersion chart from eigenwave dispersion data of VNA.

5.7 ANALYSIS OF EIGENWAVE DISPERSION RESULTS

The operating eigenwave dispersion and group velocity dispersion results from the three methods used to find the dispersions; analytical (Coupled wave theory), numerical (CST MWS) and experimental (VNA) for the 5-fold helically corrugated waveguide were analysed. The results from the eigenwave dispersion findings are charted on one plot, (Figure 5-22).

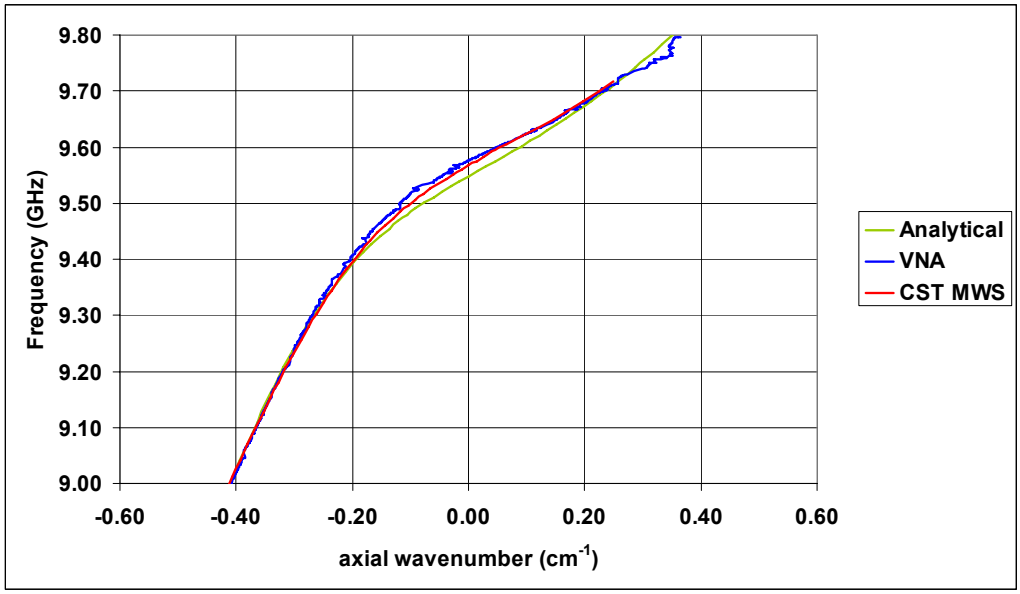

Figure 5-22 Chart of Eigenwave dispersion results.

Upon inspection of the eigenwave dispersion plots (Figure 5-22), the eigenwave dispersions calculated using CST MWS and from the VNA measurements agree fairly well with one another. The eigenwave dispersion calculated analytically deviates from the other two results in the region of 9.3 GHz to 9.6 GHz by a small amount. From 9.0 GHz to 9.6 GHz the eigenwave dispersions of the numerical and experimental findings are in very good agreement with one another.

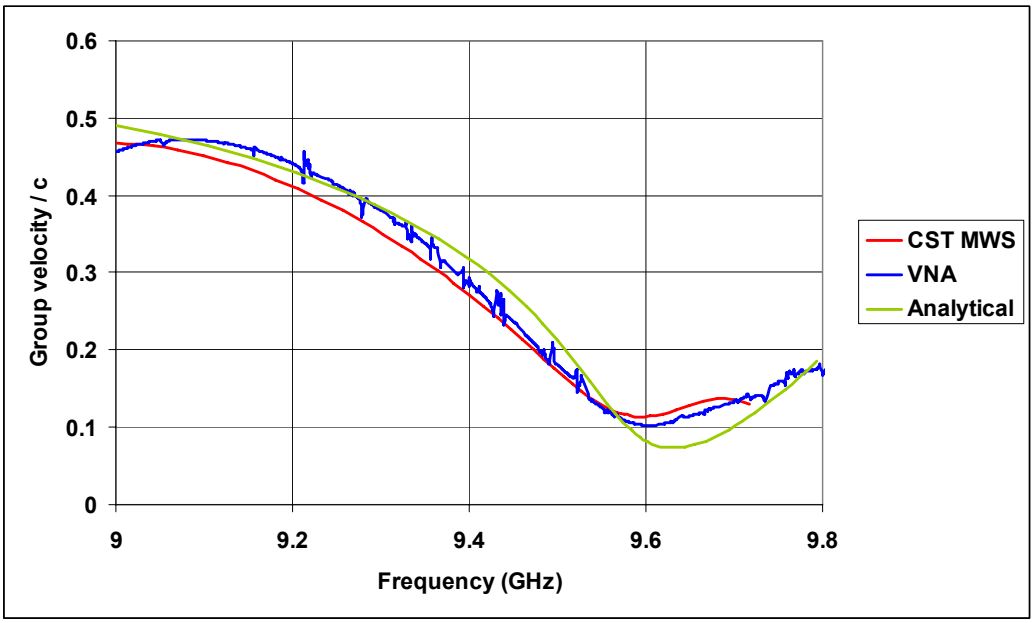

Figure 5-23 Chart of group velocity dispersion results.

The maximum group velocity was 0.49c at 9.0 GHz with a minimum group velocity of 0.07c at 9.63 GHz calculated, analytically, from coupled wave theory. The maximum group velocity was 0.46c at 9.0 GHz with a minimum group velocity of 0.11c at 9.59 GHz calculated numerically from CST MWS. The maximum group velocity was 0.48c at 9.1 GHz and a minimum group velocity of 0.10c at 9.60 GHz calculated, experimentally, from the VNA measurements.

From the three methods the average minimum group velocity was 0.11c and the average maximum group velocity was 0.48c. From the group velocity dispersions (Figure 5-23) a table was constructed to show the minimum and maximum group velocities, (Table 5-2).

Method	Minimum v_{gr}/c	Maximum v_{gr}/c
Numerical (CST MWS)	0.11	0.46
Experimental (VNA)	0.1	0.48
Analytical (Coupled wave)	0.07	0.49

Table 5-2 Group velocity results for 5-fold helically corrugated waveguide.

5.8 LOSSES MEASUREMENT IN 5-FOLD COMPRESSOR

The losses within the 5-fold waveguide compressor system were measured in the RF laboratory using two experimental methods. Firstly using the scalar network analyser (SNA) and secondly with the vector network analyser, (VNA). Each method is described in turn.

5.8.1 SNA measurement

The SNA was calibrated using a thru calibration, [Hewlett Packard 1992]. The calibration reference planes were taken to be at the ends of the elliptical polarisers, which meant that the device under test (DUT) was purely the 5-fold waveguide compressor system, (input-cones, mode converters and the main section of pulse compressor). The frequency span over which the S_{21} transmission measurement was performed on the SNA was from 9.0 GHz – 9.7 GHz. The data from the SNA measurement was exported from the computer in the RF laboratory to Microsoft Excel to produce a chart of the measured transmission, (Figure 5-24). From the chart the loss ranged, at the lower-frequency end, from approximately 0.8 dB at about 9.05 GHz to a loss, at the higher-frequency end, of approximately 2 to 2.6 dB at 9.5 – 9.7 GHz. From these figures this suggests that the losses could be anything ranging from 20 % (at 1dB) to 45% (at 2.6 dB).

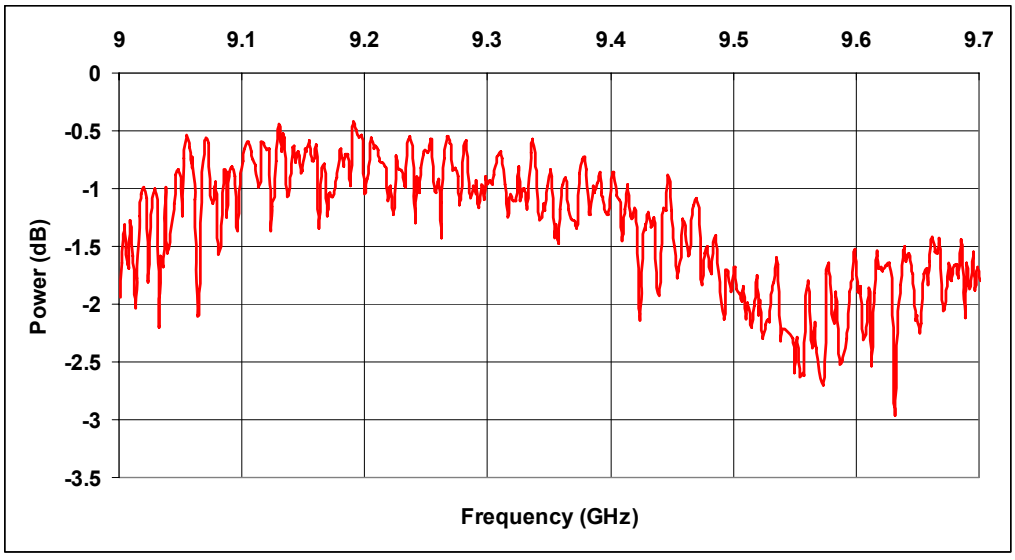

Figure 5-24 Transmission (S_{21}) measurement in 5-fold pulse compressor using SNA.

Using the data from the S_{21} measurement, the loss at intervals of 0.1 GHz from the region of 9.0 GHz to 9.6 GHz was established, (Table 5-3).

Frequency (GHz)	Loss (dB)
9.0	1.51
9.1	0.92
9.2	0.98
9.3	0.96
9.4	0.95
9.5	1.69
9.6	1.88

Table 5-3 Loss measurements for 5-fold pulse compressor using SNA.

5.8.2 VNA measurement

The VNA was calibrated using the line-reflect-line (LRL) technique as described previously where the calibration planes where taken to be the end of the co-axial-to rectangular waveguide adapters. After calibration the 5-fold helically corrugated waveguide pulse compressor was connected in place and a S_{21} measurement recorded from the Anritsu VNA.

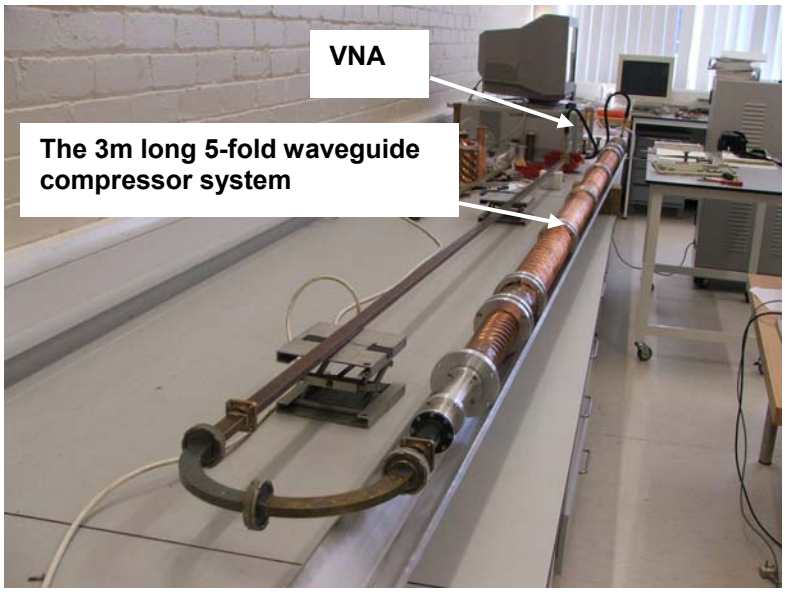

Figure 5-25 Digital photograph of Experimental set-up for VNA loss measurement.

From the measured S_{21} data the waveguide losses were established. A chart of the transmitted power variation as a function of the frequency is shown in Figure 5-26 below,

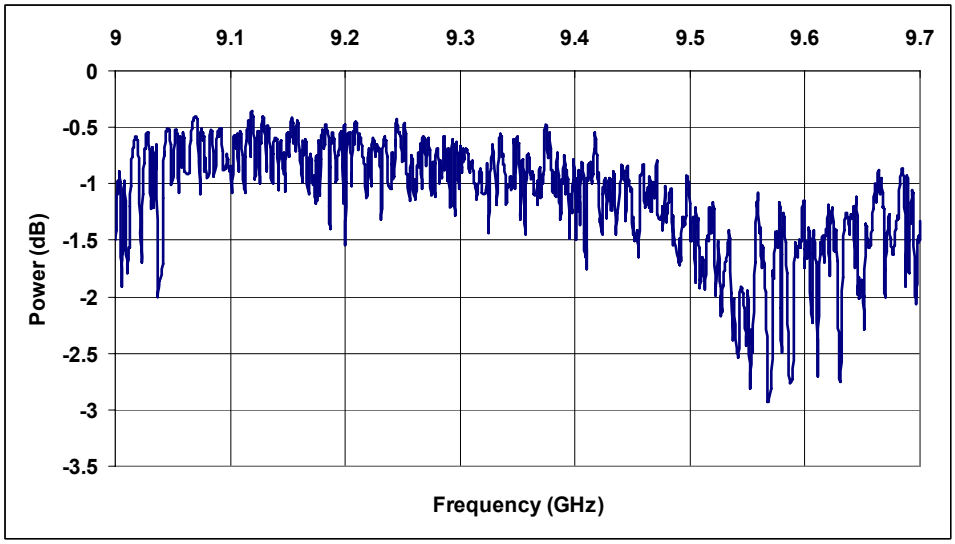

Figure 5-26 Transmission (S_{21}) measurement using VNA.

From the chart of Figure 5-26 the loss ranged, at the lower-frequency end, from approximately 0.8-0.9 dB at about 9 – 9.3 GHz to a loss, at the higher-frequency end, of approximately 1.6 to 2.6 dB at 9.5 – 9.7 GHz. Table 5-4 shows the measured loss at a particular frequency

Frequency (GHz)	Loss (dB)
9.0	1.39
9.1	0.86
9.2	0.87
9.3	0.83
9.4	0.94
9.5	1.61
9.6	1.74

Table 5-4 Loss measurements for 5-fold compressor using VNA.

The SNA and VNA loss measurements are compared with one another on a single chart, (Figure 5-27).

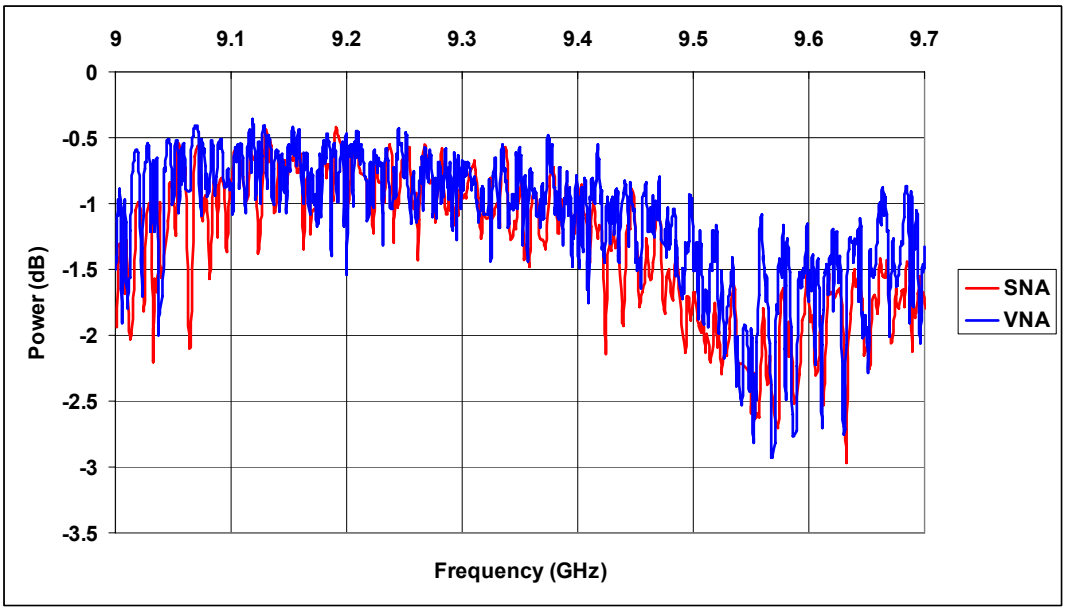

Figure 5-27 Transmission measurements in 5-fold compressor using SNA (red) and VNA (blue).

To examine more closely the measurements acquired from both the SNA and VNA the difference between the two measurements was calculated, (Table 5-5).

Frequency (GHz)	Difference in loss measurements (dB)
9.0	0.12
9.1	0.06
9.2	0.11
9.3	0.13
9.4	0.01
9.5	0.08
9.6	0.14

Table 5-5 Comparison of loss measurements for SNA and VNA.

From Table 5-5 the largest difference in measurements is at 9.3 GHz with 0.13 dB difference. The smallest difference is at 9.4 GHz with 0.01 dB difference. The average value of the difference in loss is 0.09 dB with a median value of 0.11 dB.

5.9 SIMULATION OF MICROWAVE PULSE COMPRESSION

Using the same method outlined in chapter 3 (section 3-9) the frequency-swept input pulse was simulated using equation 3-5 from the 1-D Fourier optics approach, [Burt 2004, Samsonov 2004]. The Matlab code was altered for the 5-fold helically corrugated waveguide parameters: mean radius = 3.284 cm, corrugation depth = 0.243 cm and period = 3.326 cm. The optimum eigenwave dispersion for the 5-fold helically corrugated waveguide is shown in Figure 5-28 below,

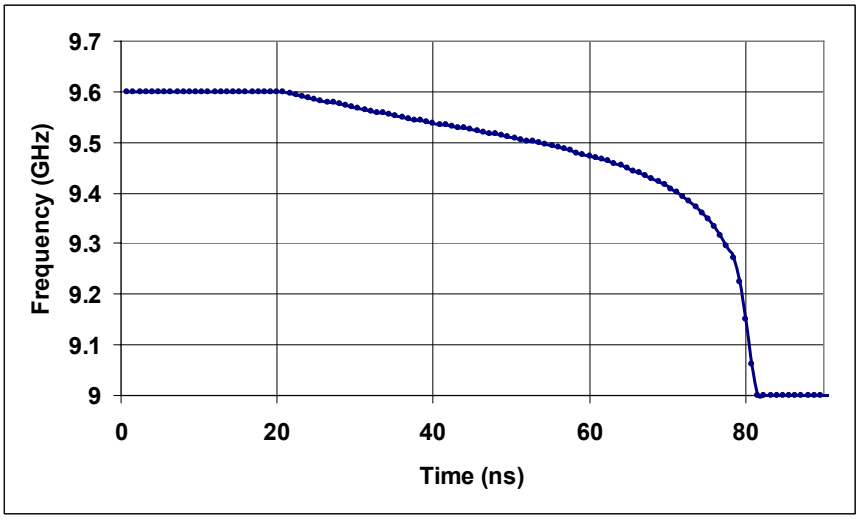

Figure 5-28 Optimum frequency-sweep for the 5-fold helically corrugated waveguide.

For the given optimum frequency-sweep of Figure 5-28 the Matlab code simulated the output microwave pulse. A power compression factor of 31 was simulated which was inclusive of ohmic losses.

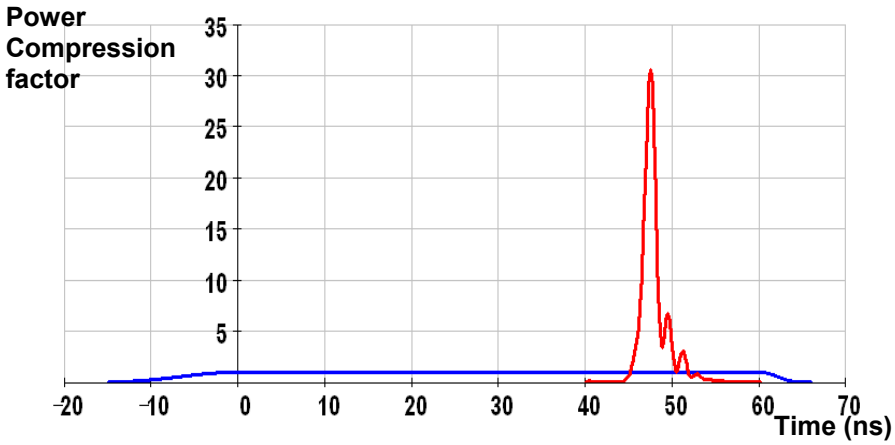

Figure 5-29 Simulation of pulse compression in 5-fold helically corrugated waveguide.

Chapter 6

The 5-Fold Microwave Pulse Compression Experiments

The chapter details the sweep-frequency based microwave pulse compression experiment results using the 5-fold helically corrugated waveguide microwave pulse compressor system. Experiments at both low (mW) and medium (kW) power levels were carried out to optimise the peak power compression factor. Power compression factors were calculated and energy compression efficiencies determined for such a waveguide compression system.

6.1 INTRODUCTION TO 5-FOLD COMPRESSION EXPERIMENTS

The experiment starting point was testing the performance of the pulse compressor for a given programmed input pulse derived from the eigenwave dispersion characteristics for the 5-fold helically corrugated waveguide detailed in chapter 5. Pulse compression experiments using the programmed input pulses where carried out at both mW and kW powers.

6.2 PULSE COMPRESSION EXPERIMENTS AT mW POWERS

The programmed input pulse from the AWG was fed into the IQ inputs of the VSG by execution of the Matlab program from the control window of the AWG. The AWG programmed input pulse had a frequency modulation of 9.6 GHz to 9.0 GHz with pulse duration 90 ns, (Figure 6-1).

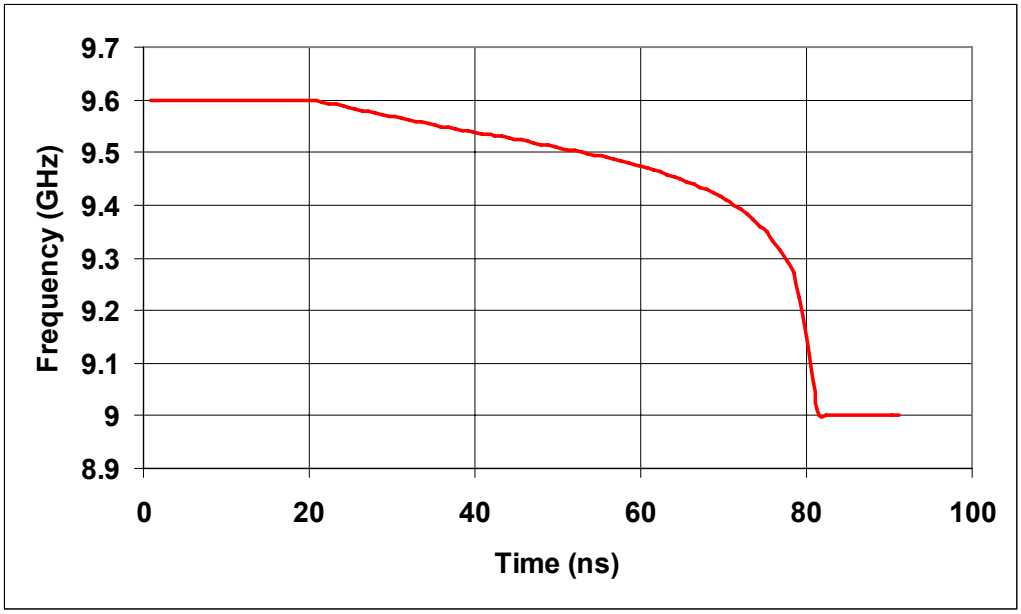

Figure 6-1 Frequency-sweep data from AWG of the input pulse to the 5-fold helically corrugated waveguide compressor.

6.2.1 Measurement of a.c. input microwave pulse

The experimental set-up to measure the input pulse was the same as that for the 3-fold pulse compressor experiment (Chapter 4). The a.c. microwave input pulse was measured on the Tektronix 12 GHz DSO. The data of the microwave input pulse on the scope was exported to Microsoft Excel, (Figure 6-2).

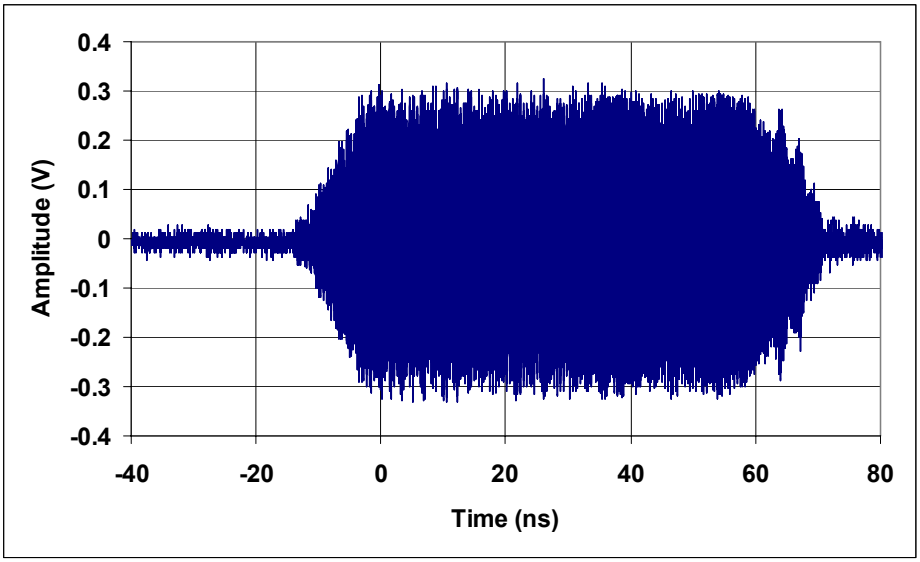

Figure 6-2 Measured a.c. input microwave pulse on 12 GHz DSO.

The data from the measured input pulse of Figure 6-2 was used in the Matlab code of Appendix H to test the frequency response of the pulse with that of the AWG programmed frequency sweep. The measured and programmed frequency-sweeps were a good match as shown below in Figure 6-3,

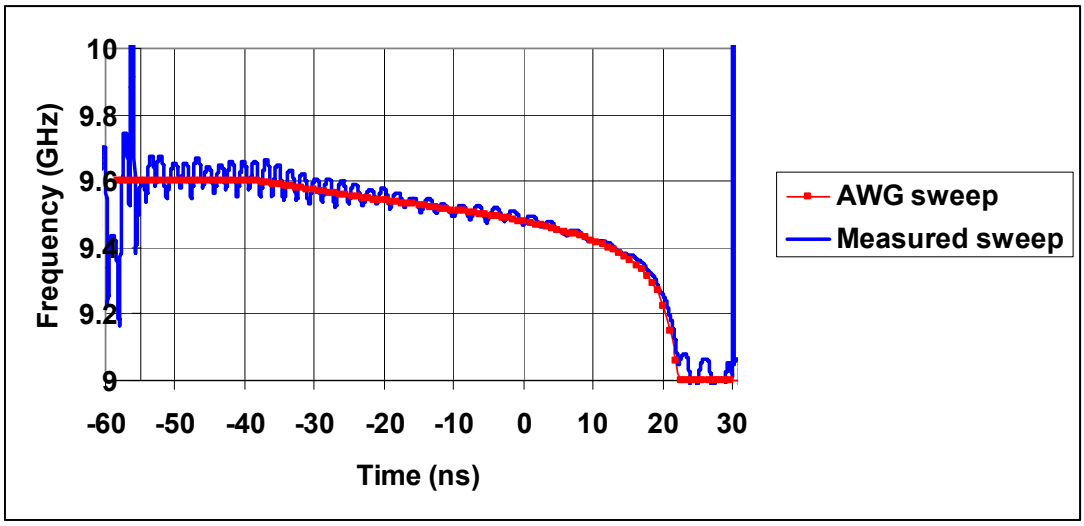

Figure 6-3 Frequency sweep of input pulse; red is AWG sweep and blue is calculated sweep using measured input pulse data.

The data from the DSO for the input microwave pulse was used to calculate the pulse properties such as the average power contained within the input pulse and the pulse

duration. The power envelope of the input microwave pulse was calculated using Microsoft Excel, (Figure 6-4).

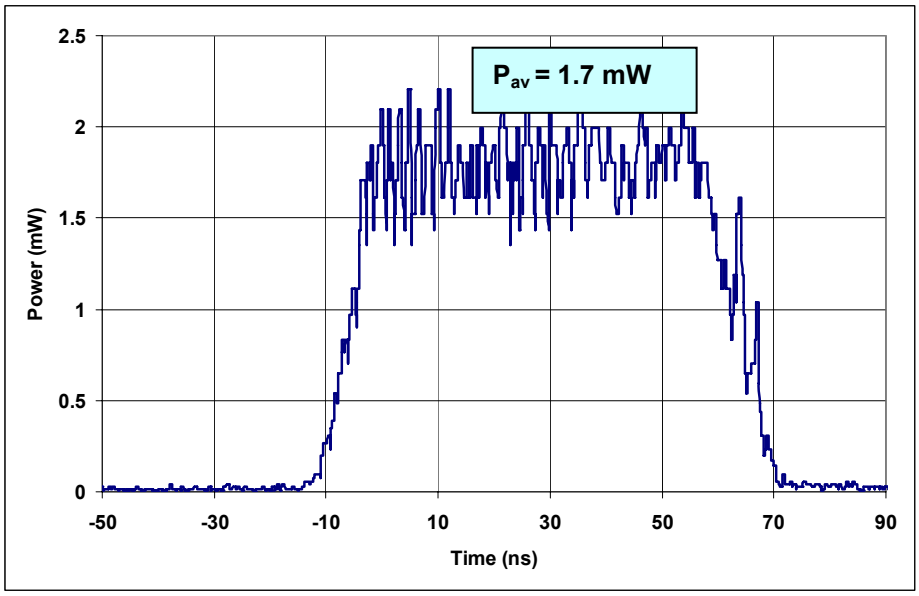

Figure 6-4 Power envelope of the input pulse to the 5-fold waveguide pulse compressor.

The input pulse had an average power (P_{av}) of 1.7 mW and pulse duration of 71 ns.

6.2.2 Measurement of a.c. output microwave pulse

The 12 GHz DSO was positioned at the output end of the waveguide pulse compressor to measure the output (compressed) microwave a.c. pulse, (Figure 6-5).

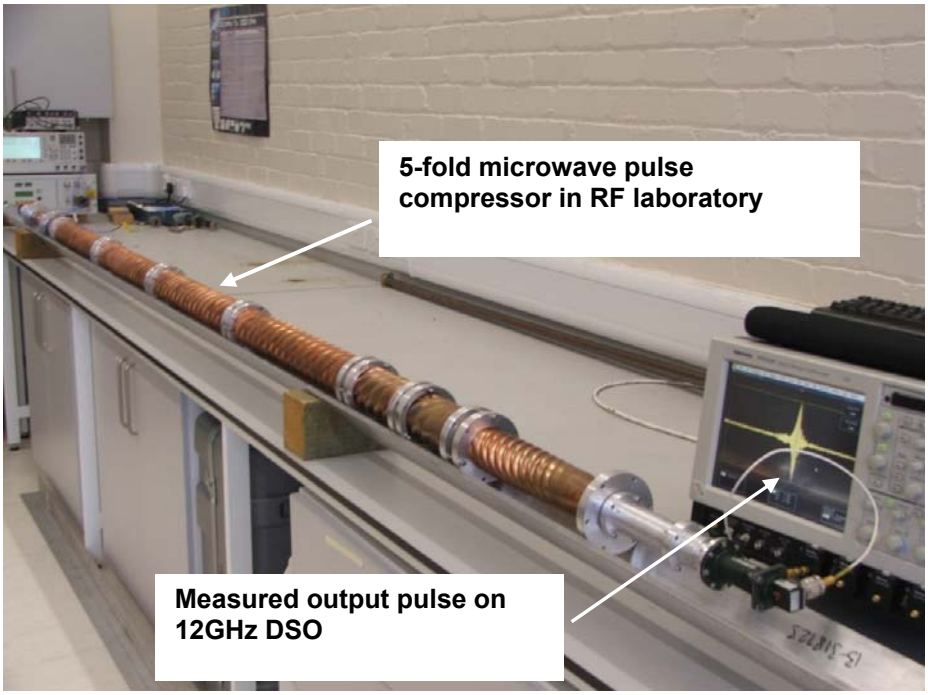

Figure 6-5 Digital photograph of the output (compressed) pulse displayed on DSO.

The data from the DSO of the measured a.c. output microwave pulse is charted in Microsoft Excel and shown below in Figure 6-6,

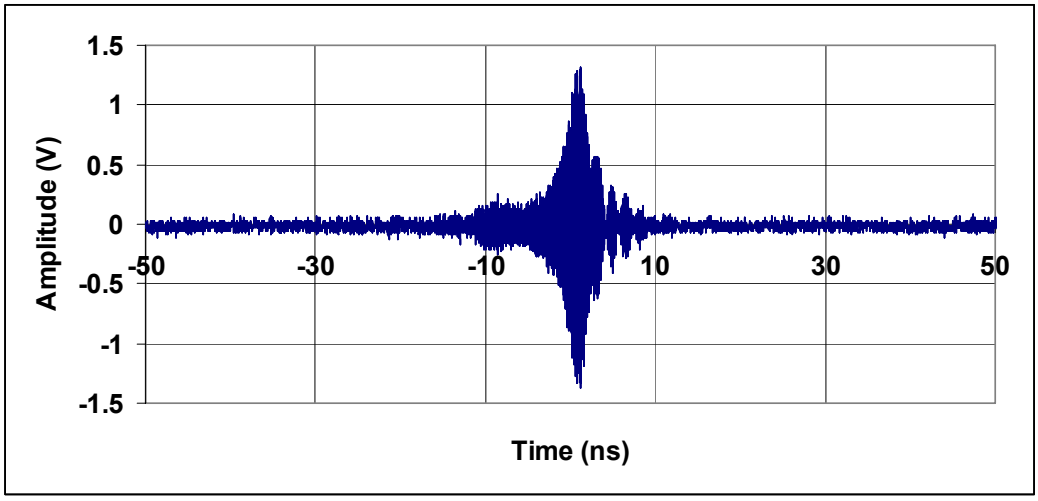

Figure 6-6 Chart of measured a.c. output microwave pulse on 12 GHz DSO.

Using the measured compressed pulse data obtained from the DSO the power envelope of the compressed pulse was calculated in Microsoft Excel. It was measured that the peak power (P_{peak}) in the compressed pulse was 37.0 mW and at FWHM the pulse width was 1.5 ns as shown in Figure 6-7 below,

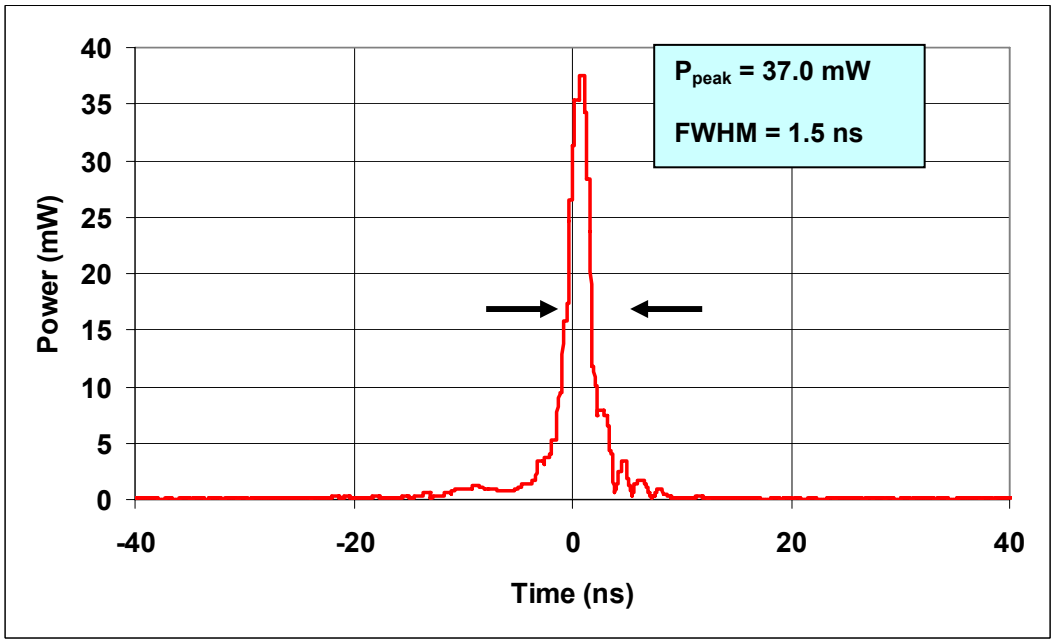

Figure 6-7 Chart of power envelope of compressed microwave pulse.

The power compression factor was calculated using the experiment data for the input and output (compressed) microwave pulses. The peak power value of the compressed pulse was measured to be 37.0 mW. The average power contained in the input microwave pulse was calculated to be 1.7 mW. From the peak power of the compressed pulse and the average power of the input pulse the power compression ratio was calculated to be 22 (13.4 dB) with an error of ± 0.5 dB. The input pulse duration was 71 ns and the compressed pulse duration at FWHM was 1.5 ns resulting in a time compression ratio of 47.3. From the ratio of the input pulse energy to that of the compressed pulse energy the pulse compression efficiency was calculated to be 41 ± 5 %.

6.3 PULSE COMPRESSION EXPERIMENTS AT kW POWERS

The inclusion of the 7-kW TWT amplifier allows for medium powers of microwave radiation to be transported in the 5-fold pulse compressor waveguide system. To trigger the TWT a pulse generator in combination with a 'trigger' oscilloscope was used to time the triggering of the input pulse. The output microwave pulse from the TWT would be the input pulse to the 5-fold waveguide pulse compressor system. To measure this pulse from the TWT microwave attenuators (co-axial and variable attenuators) and directional couplers were required to reduce the power entering the 12 GHz DSO for safe measurement and thus prevent damaging the DSO. Figure 6-8 shows the experiment set-up in the RF laboratory for measuring the input microwave pulse to the compressor.

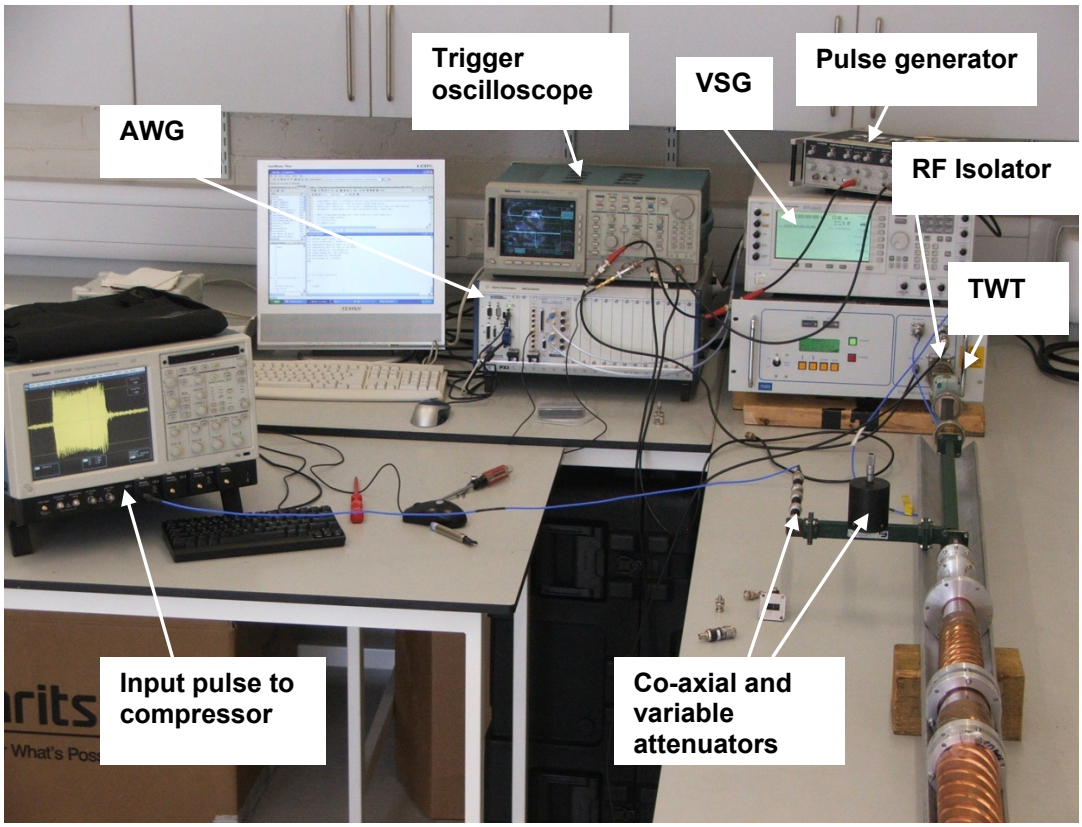

Figure 6-8 Digital photograph of experimental set-up to measure the a.c. input pulse to compressor from the TWT.

The frequency-swept AWG programmed pulse to the TWT was amended to allow for the power response to frequency in the TWT. This allowed for more control of

the output pulse from the TWT. The optimised programmed sweep (Figure 6-9) to the AWG resulted in an optimised peak power compression ratio.

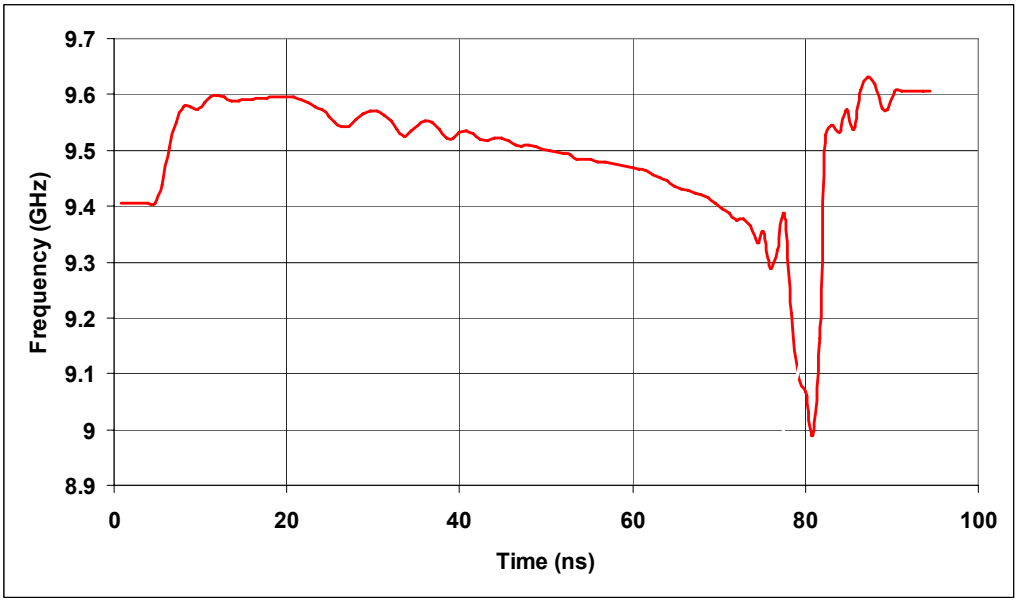

Figure 6-9 Chart of AWG frequency sweep for input microwave pulse.

6.3.1 Measurement of the a.c. input microwave pulse

The microwave input pulse from the TWT was measured with 59 dB of attenuation from the TWT to the 12 GHz DSO and this level of attenuation gave a good signal-to-noise ratio which resulted in a well defined input pulse.

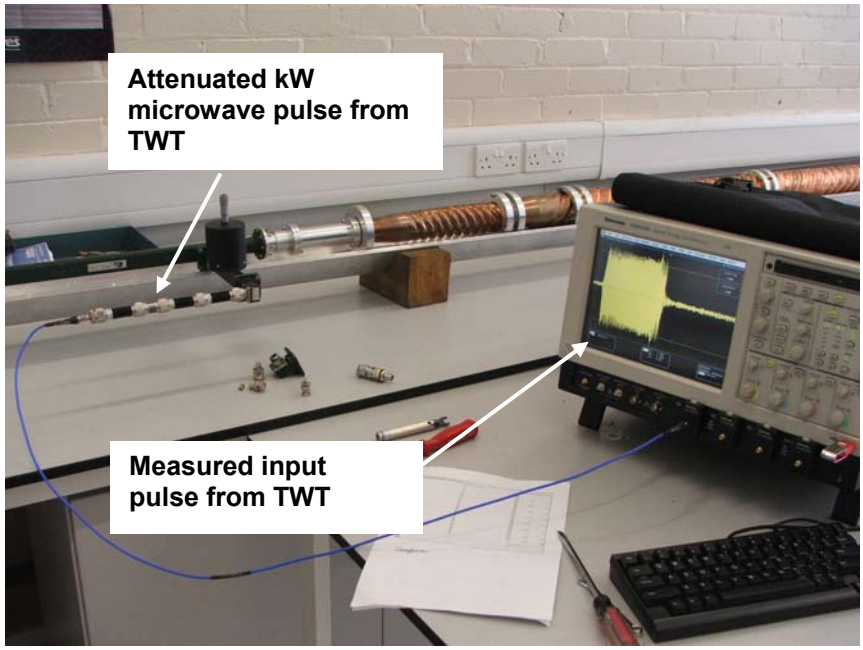

(a)

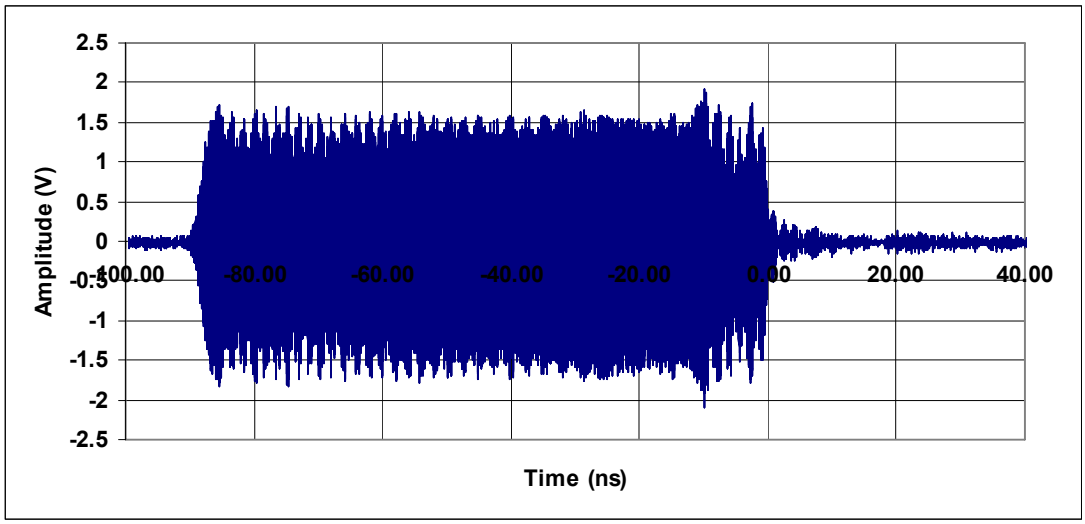

(b)

Figure 6-10 (a) Digital photograph of attenuated input microwave pulse from TWT (b) chart of attenuated a.c. input microwave pulse plotted on Microsoft Excel.

The data from the DSO of the measured input pulse to the compressor was imported into the code of Appendix H to establish the frequency response of the input microwave pulse. The output from the Matlab code (Figure 6-11) was in good agreement with that of the programmed AWG frequency-swept pulse, (Figure 6-9).

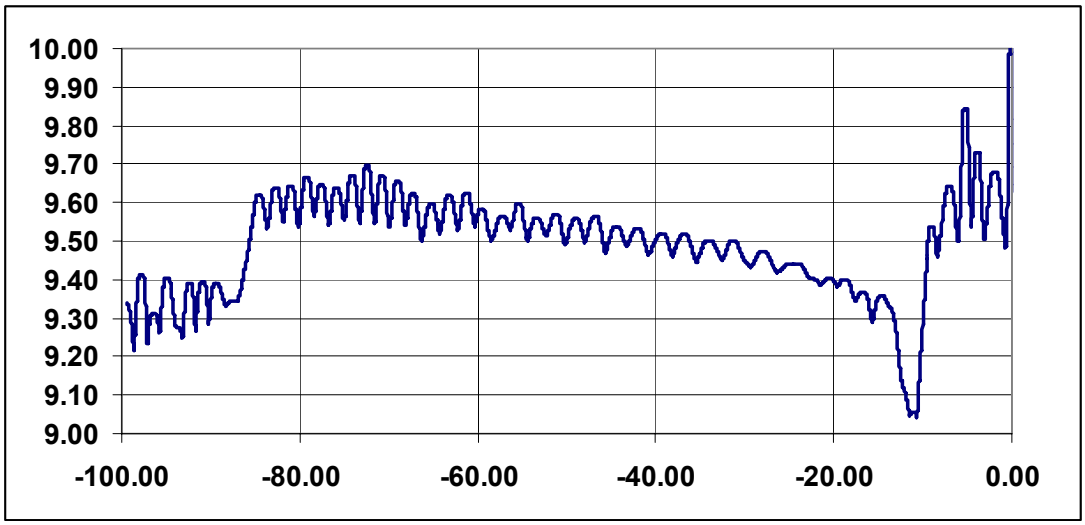

Figure 6-11 Chart of calculated frequency response of measured input pulse.

Using the pulse data from Figure 6-10 (b) the attenuated pulse was converted to the 'actual' power in the pulse i.e. where the actual power of pulse and envelope of the

power was calculated by taking into account the level of attenuation that had been applied to safely measure the kW-level input pulse from the TWT, (Figure 6-12).

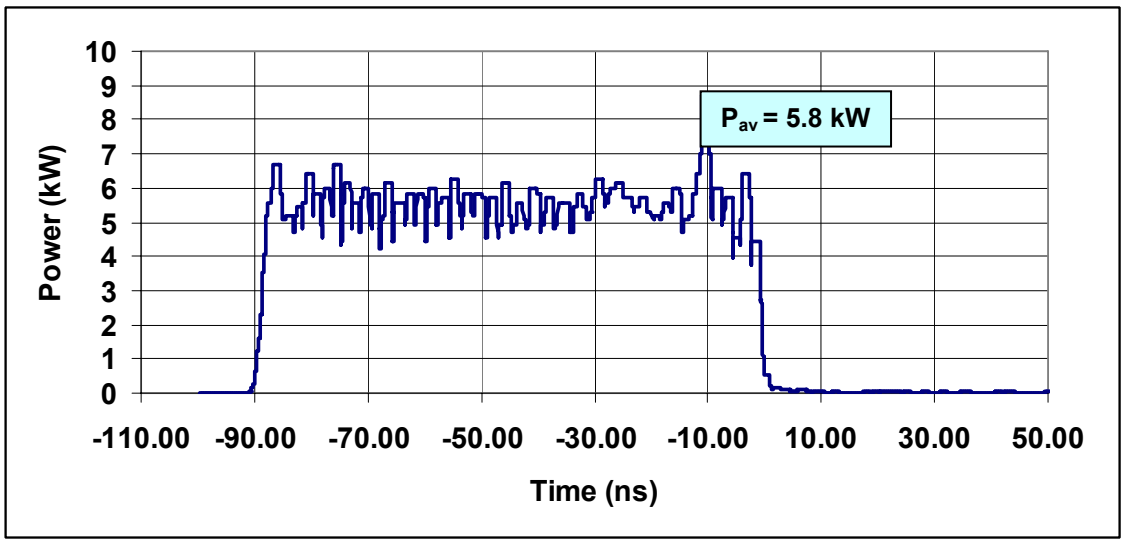

Figure 6-12 Chart of power envelope of input microwave pulse.

Analysing the input pulse data in Microsoft Excel the pulse had duration of 85 ns and an average power (P_{av}) of 5.8 kW.

6.3.2 Measurement of a.c. output microwave pulse

The compressed pulse was measured at the output of the waveguide pulse compressor via a series of microwave attenuators (co-axial attenuators and variable attenuators) on the DSO, (Figure 6-13).

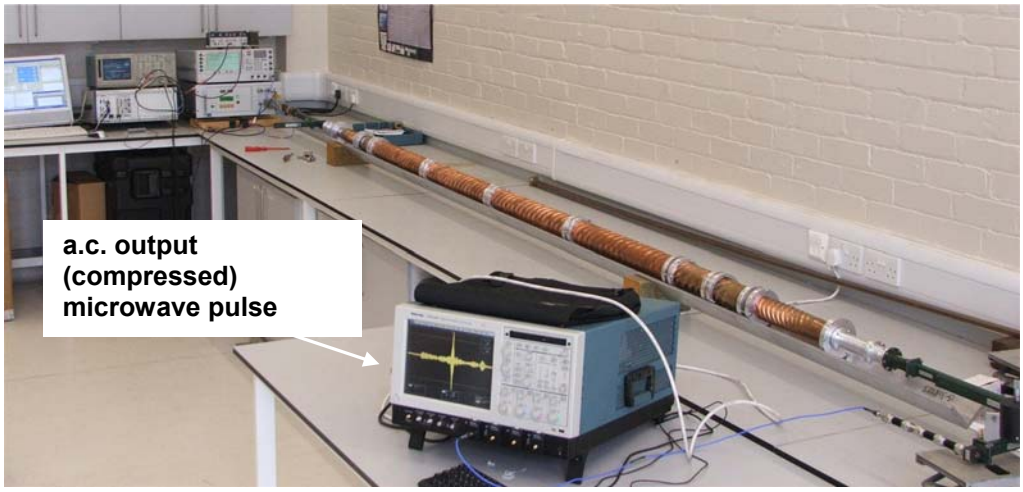

Figure 6-13 Digital photograph of output (compressed) pulse displayed on DSO.

From the measured output pulse data the peak power (P_{peak}) of the compressed microwave pulse was 144 kW at a FWHM of 1.5 ns as shown below in Figure 6-14 below,

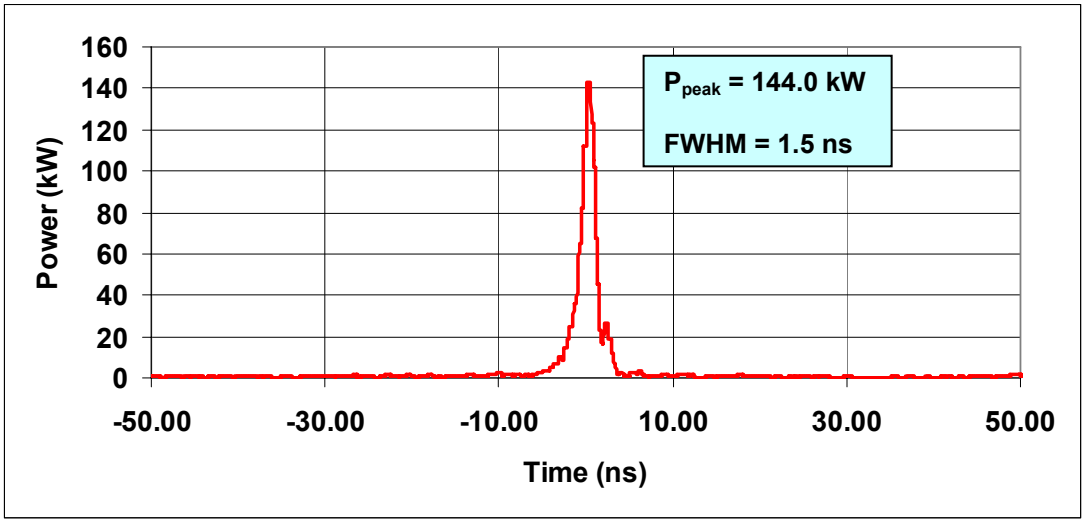

Figure 6-14 Power envelope of compressed kW microwave pulse.

The measured output (compressed) microwave pulse from the 5-fold helically corrugated waveguide compressor resulted in a compressed pulse having a peak power of 144 kW with pulse duration at FWHM of 1.5 ns. Using the average input pulse power of 5.8 kW the ratio of the peak power of the compressed pulse with the average power in the input pulse resulted in a peak power compression ratio of 24.8, with a time compression ratio calculated from the input pulse duration of 85 ns and the compressed pulse duration of 1.5 ns to be 56 and an energy pulse compression efficiency of 40 ± 5 %.

6.4 METHOD OF ATTENUATION EXPERIMENT AT kW POWERS

Using the method of attenuation as described in chapter 4 (section 4.3 and 4.5) the peak amplitudes of the rectified input pulse and rectified compressed pulse were measured on the 12 GHz Tektronix DSO to establish the peak power compression ratio as shown in Figure 6-15 below,

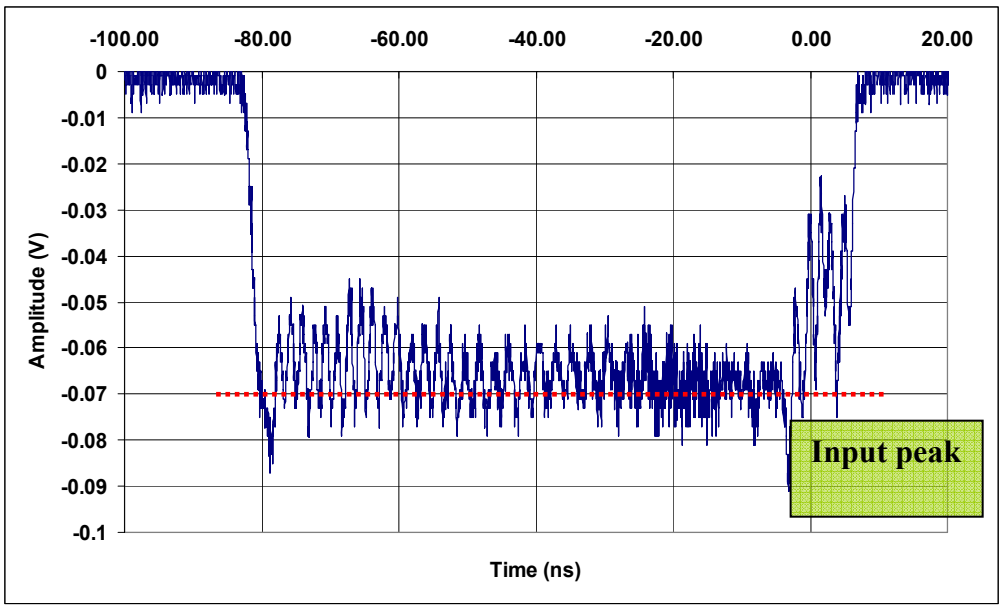

(a)

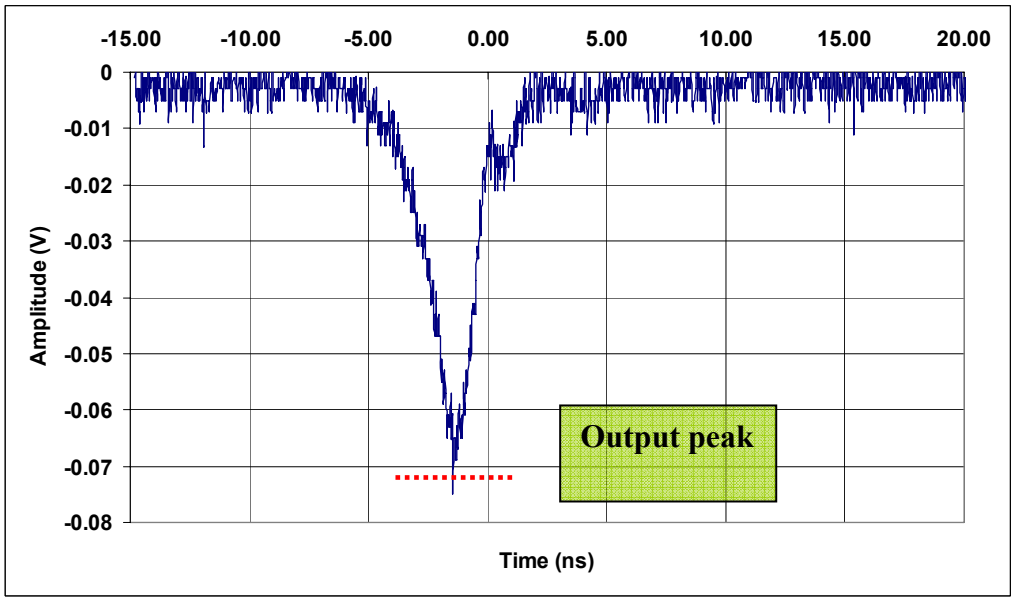

(b)

Figure 6-15 Measurement of (a) rectified input microwave pulse and (b) rectified output microwave pulse.

The variable microwave attenuator was carefully controlled to align the two peaks of both the rectified input and the rectified output microwave pulses. The measured reading from the barrel of the microwave attenuator corresponded to 13.5 dB from the calibration chart for the attenuator with an error of ± 0.5 dB which resulted in a maximum power compression ratio of 25.

Chapter 7

Conclusion

The chapter details the findings from the sweep-frequency based microwave pulse compression experiments. The experiments investigated the use of a microwave pulse compressor system using helically corrugated waveguides. Two types of helically corrugated waveguides were studied; firstly, a 3-fold helically corrugated waveguide and secondly, a larger diameter 5-fold helically corrugated waveguide. In each case the microwave power compression ratio and compression efficiencies were determined. The chapter concludes with a synopsis on possible future work that could be carried out as a result of the findings from this study.

7.1 OVERVIEW OF STUDY

A microwave compressor in the form of a helically corrugated cylindrical waveguide can have the necessary dispersion characteristics whilst, at the same time, handle high-strength electromagnetic fields and possess a low level of reflections. The helically designed microwave compressor operates far from cut-off; a distinct advantage over a smooth circular pulse compressor where the optimum region of operation is close to cut-off (Figure 7-1a). The helical compressor is less prone to reflections of part of the input pulse due to the helical waveguide being able to operate using an eigenwave far from cut-off (Figure 7-1b).

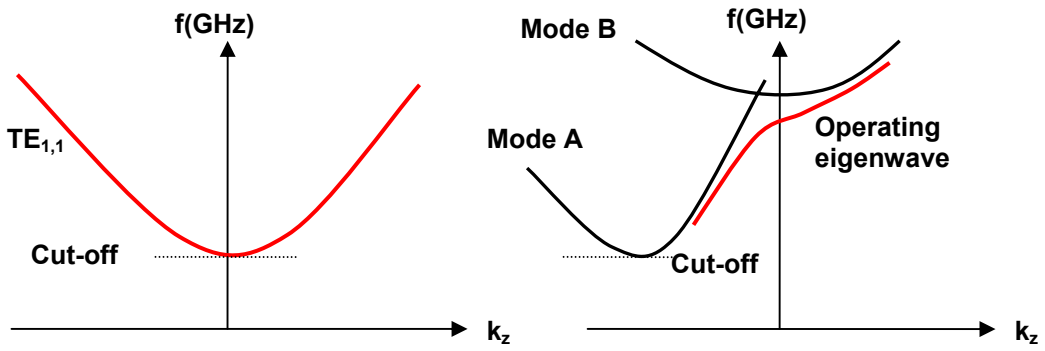

(a) (b)

Figure 7-1 Schematic of (a) circular compressor and (b) helically corrugated waveguide dispersion diagrams.

To achieve passive microwave pulse compression in the helically corrugated waveguide the frequency is swept from a higher-frequency to a lower-frequency. The wave group velocity in the dispersive medium is strongly dependent on the frequency where by the tail of the pulse moves to overtake its leading edge, resulting in pulse shortening and a corresponding growth in amplitude if the losses are sufficiently small. The significant change in group velocity with frequency is a distinct advantage for the helical compressor as this change is achieved using shorter lengths of waveguide as compared with the circular compressor which would require much longer lengths, where the frequency is swept from a lower-frequency to a higher-frequency. To that effect the helical compressor would have less ohmic loss than that of the circular compressor.

For a helical microwave compressor the optimum negative frequency sweep can be realised at the falling edge of a relativistic BWO pulse. Due to its reflection less properties a helical compressor can be used effectively at the output of a powerful amplifier.

A combination of a moderately relativistic BWO or TWT with a helical pulse compressor may result in a multi-gigawatt short-pulse microwave source which is attractive for a number of applications including radar technology and plasma chemistry.

Two types of helical compressors were investigated. Firstly, a 3-fold helically corrugated waveguide was studied and pulse compression experiments carried out. Secondly, a 5-fold helically corrugated waveguide was designed, constructed, and operated for the first time. The 5-fold helical waveguide had an average diameter of approximately two times that of the 3-fold helically corrugated waveguide. This increase in diameter would enhance its RF breakdown strength.

7.2 MICROWAVE PULSE COMPRESSION EXPERIMENTS

For both compressor systems the experiments were carried out at both low (mW) and medium (kW) powers. Before conducting the laboratory experiments a thorough analysis of the dispersion characteristics for each helically corrugated waveguide was performed using analytical, numerical and experimental techniques.

7.2.1 The 3-fold microwave pulse compressor

The use of the 3-fold copper helically corrugated waveguide of average diameter 2.94 cm resulted in a power compression ratio of 22.5 ± 2.5 with a length of approximately 2m. The 5.6 kW input pulse of duration 80 ns to the compressor had a frequency sweep which was generated in combination with the arbitrary waveform generator and vector signal generator from 9.61 GHz to 9.1 GHz. The compressed

output pulse of 140 kW had duration, full width half maximum, of 1.5 ns and a compression efficiency of 42 ± 5 %.

7.2.2 The 5-fold microwave pulse compressor

The designed, manufactured and constructed 5-fold copper helically corrugated waveguide of average diameter 6.56 cm, effectively two times larger diameter than the 3-fold waveguide, with the purpose of being able to handle higher electromagnetic powers was operated. The length of the 5-fold waveguide system was approximately 3m inclusive of the helical tapers to transport the $TE_{3,1}$ mode into the compressor helix and the mode converters which converted the $TE_{1,1}$ mode to the $TE_{3,1}$ mode and simultaneously serve as a cut-ff reflector for the $TE_{3,1}$ mode.

The compressor system achieved at best a power compression ratio of 22.3 ± 2.5 with a 144 kW compressed pulse of 1.5 ns from a 5.8 kW, 85 ns input pulse with an energy compression efficiency of approximately 40 ± 5 %.

7.3 POSSIBLE APPLICATIONS OF FINDINGS FROM STUDY

The compressed output pulse has a high-peak power and a short temporal duration. These two characteristics could be applied in the radar technology field. Radars prescribe to have good range resolution which is a function of pulse duration where the smaller the pulse duration the better the resolution. Secondly, radars require to have excellent target detection which is a function of the total energy therefore having a very high-peak power will be able to compensate for the small pulse duration thus achieving excellent target detection distances.

7.4 FUTURE WORK

7.4.1 Gyro-TWT

The microwave pulse compression experiments were carried out on the ‘bench’ where the input pulse power to the compressor was approximately 5 kW

from a conventional TWT. The Atoms, Beams and Plasmas group within the University of Strathclyde have a working gyro-TWT available. Using the output pulse from the gyro-TWT as an input pulse to the compressor could test the compressors capability at MW power levels. Furthermore, the output pulse from the gyro-TWT would be in the correct orientation of circular polarisation allowing for pulse compression to happen with relative ease.

7.4.2 Frequency-swept BWO

The BWO can produce a microwave pulse with a power of over 100 MW. The BWO can also produce very fast frequency sweeps. The optimum frequency sweep has a decreasing frequency ramp for pulse compression using a helical microwave compressor. For a helical compressor the optimum negative frequency sweep can quite naturally be realised at the falling edge of an X-band relativistic BWO pulse using the decay of the accelerating voltage pulse from a Marx bank. A method based on generation of a frequency-modulated (FM) pulse by a BWO following its compression due to propagation through a dispersive medium in the form of a hollow metallic waveguide with helical corrugation of the inner surface can be studied to produce short GW pulses.

7.5 DISCUSSION

This thesis investigated experimentally the use of both a 3-fold and 5-fold helical pulse compressor using an input pulse created on an arbitrary waveform generator and vector signal generator to produce the microwave pulse for the compressors.

For both microwave compressors the power compression ratio was around 25 and the compressed microwave pulse had temporal pulse duration of approximately 1.5 ns at full width half maximum. Given such a power compression ratio, peak powers from high-power oscillators could be exploited resulting in possible multi-gigawatt peak powers. Given the physical length of the compressor system; 2m approximately for

the 3-fold compressor and 3m approximately for the 5-fold compressor then for certain applications, say, airborne radar type applications then some engineering design factors may have to be overcome for the compressor to be both practical and functional in ‘real-life’ situations.

The larger 5-fold microwave pulse compressor having greater power handling capabilities than the smaller 3-fold microwave pulse compressor could be used at the output of a high-power BWO. Given that the guide is oversized RF breakdown would not occur.

REFERENCES

Abubakirov E B, et al., *An X-Band Gigawatt Amplifier*, IEEE Trans. Plasma. Sci., **30**, No. 3, 1041, 2002.

Agilent, E8257D/67D PSG V*ector Signal Generator Operator's User's Guide*, Agilent Technologies, Inc, USA, (2006).

Agilent, N6030A Series A*rbitrary Waveform Generator User's Guide*, Agilent Technologies, Inc, USA, (2006).

Alvarez R A, Byrne D and Johnson R M, *Pre-pulse Suppression in Microwave Pulse-Compression Cavities*, Rev. Sci. Instum., **57** (10), pp.2475-2480,1986.

Alvarez R A, *Some Properties of Microwave Resonant Cavities Relevant to Pulse-Compression Power Amplification*, Rev. Sci. Instum., **57** (10), pp.2481-2488, 1986.

Anritsu, *Vector Network Analyser Operator's Manual*, Agilent Technologies, Inc, USA, (2007).

Antonsen T M, Safier P, Chernin D P, and Levush B, *Stability of travelling wave amplifiers with reflections*, IEEE Trans. Plasma Sci., **30**, No. 3, 1089, 2002.

Barker R J and Schamiloglu E, Eds., *High-Power Microwave Sources and Technologies*, (IEEE Press, New York, 2001).

Benford J and Swegle J, *High-Power Microwaves*, (Artech House, Boston and London, 2007).

Benson H, *University Physics Revised Ed.*, (John-Wiley & Sons, Inc., NY, 1996).

Birx D et al., *Microwave Power Gain Utilizing Superconducting Resonant Energy Storage*, Appl. Phys. Lett., **32** (1), pp.68-70, 1978.

Bratman V L, Cross A W, Denisov G G, et al., *High-Gain Wide-Band Gyrotron Travelling Wave Amplifier with a Helically Corrugated Waveguide*, Phys. Rev. Lett., **84**, No. 12, 2746, (2000).

Bratman V L, Denisov G G, Samsonov S V, et al., *Method for Achievement of a Multigigawatt Peak Power by Compressing Microwave Pulse of a Relativistic Backward-Wave Oscillator in a Helical Waveguide,* Radiophysics and Quantum Electronics, **50**, No. 1, (2007).

Bratman V L, Denisov G G, Samsonov S V, et al., *High-Efficiency Wideband Gyro-TWTs and Gyro-BWOs with Helically Corrugated Waveguides*, Radiophysics and Quantum Electronics, **50**, No. 2, (2007).

Bromley R A and Callan B E, *Use of a Waveguide Dispersive Line in an f.m. Pulse Compression System*, Proc., IEE **114**, 1213, (1967).

Bryant G H, *Principles of Microwave Measurements*, IEE Electrical Measurement Series 5, (1993).

Burt G, Samsonov S V, Ronald K, et al., *Dispersion of Helically Corrugated Waveguides: Analytical, Numerical, and Experimental Study*, Phys. Rev. E, **70**, No. 4, 046402, (2004).

Burt Graeme C, *Sweep-frequency microwave pulse compression using a helically corrugated waveguide*, PhD Thesis, (2004).

Burt G, Samsonov S V, Phelps A D R, et al., *Microwave Pulse Compression Using a Helically Corrugated Waveguide*, IEEE Trans. Plasma Sci., **33**, No. 2, 661, (2005).

Cairns R A and Phelps A D R, Eds., *Generation and Application of High-Power Microwaves*, (Bristol, U.K.: IOP, 1997).

Cohen B, Cohen R H, Nevins W M and Rognlien T D, *Theory of free-electron laser heating and current drive in magnetized plasmas*, Rev. Mod. Phys., **63**, 1991 pp. 949 -990

Collin Robert E, *Foundations of Microwave Engineering* 2nd Edition, IEEE Press Series on Electromagnetic Wave Theory, New York, (2001).

Cook Nigel P, *Microwave Principles and Systems*, (Prentice-Hall, 1986).

Cooke S J and Denisov G G, *Linear Theory of a Wide-Band Gyro-TWT Amplifier using Spiral Waveguide*, IEEE Trans. Plasma Sci., **26**, No. 3, 519, (1998).

Cornbleet S, *Microwave Optics*, Academic Press Inc., London, (1976).

Cross A W, He W, Phelps A D R, et al., *Helically Corrugated Waveguide Gyrotron Traveling Wave Amplifier using a Thermionic Electron Gun*, Appl. Phys. Lett., **90**, 253501, (2007).

CST Microwave Studio User's Manual, Wellesley Hills, MA, USA, 2009.

Denisov G G, Bratman V L, Phelps A D R and Samsonov S V, *Gyro-TWT with a Helical Operating Waveguide: New Possibilities to Enhance Efficiency and Frequency Bandwidth*, IEEE Trans. Plasma Sci., **26**, No. 3, 508, (1998).

Denisov G G, Bratman V L, Cross A W, et al., *Gyrotron Travelling Wave Amplifier with a Helical Interaction Waveguide*, Phys. Rev. Lett., **81**, No. 25, 5680, (1998).

Dobbs E R, *Electromagnetic Waves*, Routledge & Kegab Paul, London, (1985).

Eastwood J W, *Computer Modelling of Microwave Sources*, in Generation and Application of High-Power Microwaves, edited R.A. Cairns, and A.D.R. Phelps, (Bristol, U.K.: IOP, 1997).

Edgcombe C J, Ed., *Gyrotron Oscillators*, (Taylor and Francis, London, 1993).

Farkas Z D, Hogg H A, Loew G A and Wilson P B, *SLED: A mehod for doubling SLACs energy*, SLAC-PUB-1453, Stanford Linear Accelerator Centre, California, 1974.

Farkas Z D, *Binary Peak Power Multiplier and Its Application to Linear Accelerator Design*, IEEE Trans. Microwave Theory Tech., **MTT-34**, 1036, (1986).

Farkas Z D, Spalek G and Wilson P B, *RF Pulse Compression Experiment at SLAC*, IEEE Proc. Particle Accelerator Conference, Accelerator Science and Technology, (1989).

Farkas Z D et. al., *Two-Klystron Binary Pulse Compression at SLAC*, SLAC-PUB-6100, (1993).

Feynman Richard P, Leighton Robert B and Sands Matthew, *The Feynman Lectures on Physics*, vol. 2, (Addison-Wesley Publishing Company, Sixth Printing, 1977).

Fleisch D, *A Student's Guide to Maxwell's Equations*, Cambridge University Press, (2009).

Flyagin V A, Gaponov A V, Petelin M I and Yulpatov V K, *The Gyrotron*, IEEE Trans. Microwave Theory Tech., **MTT-25**, 514, (1977).

Freund H P and Antonsen T M, *Principles of Free-electron Lasers* (Chapman and Hall, London, 1992).

Fuks M I, Kovalev N, *Selective Multichannel Feedback*, IEEE Trans. Plasma Sci., **30**, No. 3, 1147, (2002).

Fuller A J Baden, *Microwaves*, (Pergamon Press, 1969).

Gaponov–Grekhov A V and Granatstein V L, Editors, *Applications of High-Power Microwaves*, (Artech House, Boston and London, 1994).

Gilmour A S, Jr., *Microwave Tubes*, (Artech House, Boston and London, 1986).

Gilmour A S, Jr., *Principles of Travelling Wave Tubes*, (Artech House, Boston and London, 1994).

Gold S H and Nusinovich G S, *Review of High-Power Microwave Source Research*, Rev. Sci. Instrum., **68**, (11), (1997).

Granatstein V L and Alexeff I, *High-Power Microwave Sources*, Artech House, Boston and London, (1987).

Granatstein V L and Lawson W, *Gyro-Amplifiers as Candidate RF Drivers for TeV Linear Colliders*, IEEE Trans. Plasma. Sci., **24**, pp.648 – 665, 1996.

Grant I S and Phillips W R, *Electromagnetism* 2nd Ed., John Wiley & Sons, (2004).

Gunin A V, Klimov A I, Korovin S D, et al., *Relativistic X-Band BWO with 3 GW Output Power*, IEEE Trans. Plasma Sci., **26**, No. 3, pp. 326-331, (1998).

Hanselman Duane and Littlefield Bruce, *Mastering Matlab 7* (International Edition) Pearson Prentice Hall Publishing, (2005).

He W, Ronald K, Young A R, et al., *Gyro-BWO Experiments Using a Helical Interaction Waveguide*, IEEE Trans. Electron Devices, **52**, No. 5, 839, (2005).

He W, Cross A W, Phelps A D R, et al., *Theory and Simulations of a Gyrotron Backward Wave Oscillator using a Helical Interaction Waveguide*, Appl. Phys. Lett., **89**, 091504, (2006).

Hecht, *Optics* 2nd Ed., Addison-Wesley Publishing Company, 1987.

Hewlett Packard, 8757D Scalar Network Analyser, Operations Manual, 1992.

Hirshfield J L and Wachtel J M, *Electron Cyclotron Maser*, Phys. Rev. Lett., **12**, No. 19, pp. 533-537, (1964).

Hirshfield J L and Granatstein V L, *The Electron Cyclotron Maser – An Historical Survey*, IEEE Trans. Microwave Theory Tech., **MTT-25** 522, (1977).

Hirshfield J L et al., *Active RF Pulse Compression for Accelerator Applications*, IEEE Trans. Microwave Theory Tech., **MTT-S** digest, pp.1021-1022, (2004).

Humphries S, Jr., *Charged Particle Beams*, (Wiley, New York, 1990).

Ishii T. Koryu, *Microwave Engineering*, 2nd Edition, Harcourt Brace Jovanovich, Inc., 1989.

Ishii T. Koryu, *Handbook of Microwave Technology* Vol. 2 Academic Press, 1995.

Jackson J D *Classical Electrodynamics*, Wiley & Sons, New York, 1998.

Kreyszig E, *Advanced Engineering Mathematics,* 9th Edition, John Wiley & Sons, Inc., 2006.

Lance A L, *Introduction to Microwave Theory and Measurements*, McGraw-Hill Book Company, USA, 1964.

Laverghetta T, *Microwave Materials and Fabrication Techniques 2nd Edition*, Artech House: Boston London, 1991.

Lorrain P, Corson D R, and Lorrain F, *Electromagnetic Fields and Waves* 3rd Ed., W.H. Freeman and Company, New York, 1985.

Maxwell J C, *A Dynamical Theory of the Electromagnetic Field*, Phil. Trans. R. Soc. Lond. 1865, **155** 459-512.

M. McStravick, S.V. Samsonov, K. Ronald, S.V. Mishakin, W. He, G.G. Denisov, C.G. Whyte, V.L. Bratman, A.W. Cross, A.R. Young, P. MacInnes, C.W. Robertson, and A.D.R. Phelps, *Experimental results on microwave pulse compression using helically corrugated waveguide*, J. Appl. Phys., **108**, 054908 (2010).

Motz H, J. *Applications of the Radiation from Fast Electrons*, Appl. Phys. Lett., **22**, p.527, (1951).

Nantista C, Farkas Z D et. al., *High-Power RF Pulse Compression with SLED II at SLAC*, SLAC-PUB-6145, (1993).

Page R M, *The Origin of Radar*, (New York: Doubleday, 1962).

Petelin M I, Hirshfield J L, Kuzikov S V, and Vikharev A L, *High power microwave pulse compressors: Passive, active, and combined*, Proc. Intense Microwave Pulses VII, H E Brandt, ED., SPIE vol. 4031, pp 224-231, 2000.

Phelps A D R, *Introduction to Microwave Sources*, in Generation and Application of High-Power Microwaves, edited R.A. Cairns, and A.D.R. Phelps, (Bristol, U.K.: IOP, 1997).

Pierce J R, *Traveling Wave Tubes*, N.J.:D. Van Nostrand, 1950.

Pozar D M, *Microwave Engineering Second Edition* (John-Wiley & Sons, Inc New York, 1998).

Ridenour L N and G B Collins, *Radiation Laboratory Series*, (Cambridge, Mass.: M.I.T. Press, 28 volumes, 1946).

Rosen A, Stuchly M A, and Vander Vorst A, *Applications of RF/Microwaves in Medicine*, IEEE Trans. Microwave Theory Tech., **MTT-50**, No.3, 963 – 974, 2002.

Samsonov S V, Denisov G G, Bratman V L, et al., *Frequency-Tuneable CW Gyro-BWO with a Helically Rippled Operating Waveguide*, IEEE Trans. Plasma Sci., **32**, No. 3, 884, (2004).

Samsonov S V, Phelps A D R, Bratman V L, et al., *Compression of Frequency-Modulated Pulses using Helically Corrugated Waveguide and Its Potential for Generating Multigigawatt rf Radiation*, Phys. Rev. Lett., **92**, No. 11, 2004.

Scott W Allan, *Understanding microwaves*, A John Wiley & Sons, Inc., (2005).

Seeger John A, *Microwave Theory, Components, and Devices*, (Prentice-Hall, 1986).

Spiegel Murray R, *Vector Analysis and An Introduction to Tensor Analysis*, Schaum's Outline Series, McGraw-Hill, 1959.

Squires G L, *Practical Physics*, 3rd Edition, Cambridge University Press, 1997.

Tantawi S G, Ruth R D, Vlieks A E, *Active Radio Frequency Pulse Compression using Switched Resonant Delay Lines*, Nuclear Instruments and Methods in Physics Research A, 370 pp. 297-302, (1996).

Tantawi S G, Ruth R D, Vlieks A E and Zolotorev M, *Active High-Power RF Pulse Compression using Optically Switched Resonant Delay Lines*, IEEE Trans. Microwave Theory Tech., **MTT-45** 1486, (1997).

Tantawi S G, Ruth R D, and P B Wilson, Proceedings of the Particle Accelerator Conf. 423 – 425 *A comparison between pulse compression options for the NLC* (New York, 1999).

Tantawi S G, et al., *A Half Gigawatt Dual-Moded X-band Transmission and Rf Pulse Compression System*, IEEE Trans. Microwave Theory Tech., **MTT-S** digest, pp. 1023-1026, (2004).

Tantawi S G, Nantista C D, Dolgashev V A, et al., *High-Power Multimode X-Band RF Pulse Compression System for Future Linear Colliders*, Physical Review Special Topics –Accelerators and Beams, **8**, 042002, (2005).

Tektronix, TDS6000B & TDS6000C Series *Digital Storage Oscilloscope Operator's Manual*, (USA, 071-1658-02).

Thomas H E, *Handbook of Microwave Techniques and Equipment*, Prentice-Hall, Inc, Englewood Cliffs, N.J. 1972.

Thumm M K, *Modes and Mode Conversion in Microwave Devices*, in Generation and Application of High Power Microwaves, edited R.A. Cairns, and A.D.R. Phelps, (Bristol, U.K.: IOP, 1997).

Thumm M K and Kasparek W, *Passive High-Power Microwave Components*, IEEE Trans. Plasma Sci. **30**, p.755, (2002).

Tsimring S E, *Electron Beams and Microwave Electronics*, John Wiley & Sons, Inc., (2007).

Twiss R Q, *Radiation Transfer and the Possibility of Negative Absorption in Radio Astronomy,* Aust. Journal Phys., **11**, 1958.

Vanderlinde J, *Classical Electromagnetic Theory*, John Wiley & Sons, Singapore, 1993.

Vikharev A L et al., *100 MW Active X-band Pulse Compressor*, Proc. of the Particle Accelerator Conf. pp. 1474-1476, (New York, 1999).

Vikharev A L et al., *First High-Power Experiments on a Two-Channel X-band Active RF Pulse Compressor*, Proc. of the Particle Accelerator Conference, pp. 1147 – 1149, (2003).

Vikharev A L et al., *Plasma Switch for X-band Active SLED-II RF Pulse Compressor*, American Institute of Physics, pp. 790 -796, (2004).

Vikharev A L, Gorbachev A M, Ivanov O A, et al., *High Power Active X-Band Pulse Compressor using Plasma Switches*, Physical Review Special Topics – Accelerators and Beams, **12**, 062003, (2009).

Vrba J, *Medical Applications of Microwaves*, Electromagnetic, Biology and Medicine, **24**: 441 – 448, (2005).

Watt Sir Robert Watson, *The Pulse of Radar*, (New York: Dial, 1959).

Wilson P B, Farkas Z D and Ruth R D, *SLED II: A new method of RF pulse compression*, SLAC-PUB-5330, Stanford Linear Accelerator Centre, California, Sept. 1990).

Yakovlev V P, Nezhevenk O A, Hirshfield J L, et al., *Active RF Pulse Compressor with a Ferroelectric Switch*, Proceedings of the 2003 Particle Accelerator Conference.

Appendices

Appendix A - Overview of vacuum electronics and devices
Appendix B - Maxwell's equations in matter
Appendix C - Mode patterns for rectangular and circular waveguide
Appendix D - Matlab code to calculate dispersion using coupled waves
Appendix E - VBA macro for helically corrugated waveguide
Appendix F - Polarisation
Appendix G - Matlab code to drive AWG in compression experiments
Appendix H - Matlab code for analysis of measured input pulses
Appendix I - Author's publications

Appendix A

Historically, microwave electronics goes back to the experimental work of a German professor of physics by the name of Heinrich Hertz. He carried out his work around 1887. Hertz used a spark gap generator to produce electromagnetic waves in a very large frequency band around 450 MHz with an antenna that measured half a wavelength at this frequency. The receiving antenna had the same dimensions. Hertz also used parabolic mirrors and lenses of dielectric material. Hertz was the first pioneer experimenter in the microwave field, [Jackson 1998, Pozar 1998].

In 1893 Lord Kelvin gave a theoretical analysis of hollow waveguides and shortly afterwards Oliver Lodge demonstrated waveguides at frequencies of 1.5 - 4 GHz. Guylielmo Marconi's early experiments in radio communications, from 1894 to 1896, were at frequencies of up to 1 GHz. During the 1930s there were a number of important developments in microwaves. Marconi experimented with line-of-sight communications links at frequencies around 600 MHz. In 1933, he installed a microwave link between the Vatican and the summer residence of the pope, a distance of 15 miles. A. G. Clavier directed the setting up and demonstration of a microwave link between Dover, England and Calais, France, in 1931.

It was the need for radar, an acronym of 'radio detection and ranging', during World War II (1939 -1945) that stimulated a very rapid growth in microwave technology [Page 1962, Watt 1959]. The first radars used wavelengths of a few metres but it was realised from the start shorter wavelengths would yield better directivity of the radar beam as well as stronger reflections from small objects such as airplanes. Microwave research in the United States during the war is documented in the 28-volume MIT Radiation Laboratory series, [Ridenour 1946]. Also significant during this period was the work of George C. Southworth and W. L. Barrow in developing hollow waveguides. Southworth, Schelkunoff, Slate and Hansen also did important theoretical work on resonators and antennas. However, the main things needed were generators and detectors for these high microwave frequencies.

A significant development in the microwave area was the invention of the Barkhausen Kurz tube in 1919, which made it possible to build effective oscillators at frequencies above 300 MHz. The invention and improvement of microwave sources and amplifiers have been milestones in the history of microwaves. Such sources are summarised below,

The magnetron

Magnetrons are devices which are efficient generators of microwave energy and were the first devices capable of generating high-power microwaves. Arthur Hull developed the co-axial magnetron, as a low frequency amplifier and oscillator. The development of the high-power cavity magnetron by J. T. Randal and H. A. H. Boot in 1940 made effective radar systems possible [Benford 1992]. The magnetron is a cross field device, where the static electric and static magnetic fields are at right angles with each other, [Gilmour 1986]. The magnetron is made up of circular resonant cavities around a cathode immersed in a perpendicular magnetic field. This magnetic field results in a force that changes the motion of electrons from a straight path to a curved one. It is the curved motion that allows for efficient means of electron bunching that extracts direct current (DC) energy from the electrons to the radio frequency (RF) field to produce high-power microwave output. A small hook, usually referred to as a pick-up loop, is used to extract the microwave energy from this cavity (and thereby all others) when the magnetron oscillates in one of the cavities.

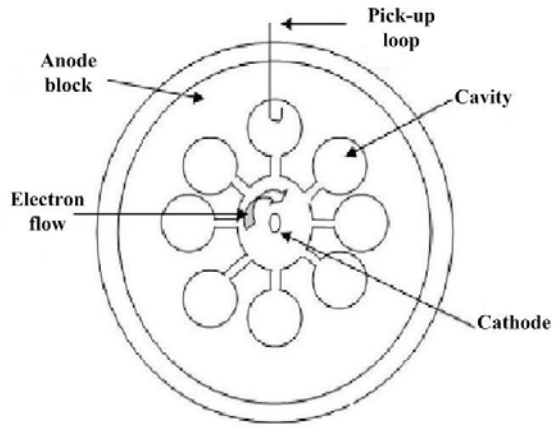

Figure A1 Schematic of cavity magnetron.

The cavity magnetron could be utilized to supply short, high-powered, microwave frequency pulses for radar applications and was instrumental in the development of the first radar system used in World War II. Depending on the application there are two types of magnetrons; pulsed, with a peak output power of kWs to MWs, and continuous wave (CW) of output powers of Ws to tens of kWs.

The klystron

The invention of the klystron tube by the brothers Russell and Sigurd Varian resulted around 1939 when they succeeded in using the transit time of an electron beam for the amplification and generation of high frequency microwaves [Humphries 1990]. A thermionic cathode emits a stream of electrons that immediately are attracted and travel to the large positive potential on the collector via the two cavities called a 'buncher' and a 'catcher'. An input signal applied to the 'buncher' causes oscillations within that cavity. These oscillations cause a speeding up and slowing down of the electron stream travelling from cathode to anode. The 'buncher' cavity oscillations cause bunches of electrons at the frequency of the input signal. The velocity-modulated electron bunches move away from the 'buncher' cavity and enter the drift space. The drift space is where the accelerated electrons tend to catch up with the retarded electrons and form bunches. Bunches of electrons pass the gap of the 'catcher' resonator. These bunches induce oscillations in the 'catcher' resonator, and these oscillations are transferred out of the cavity by using loop coupling.

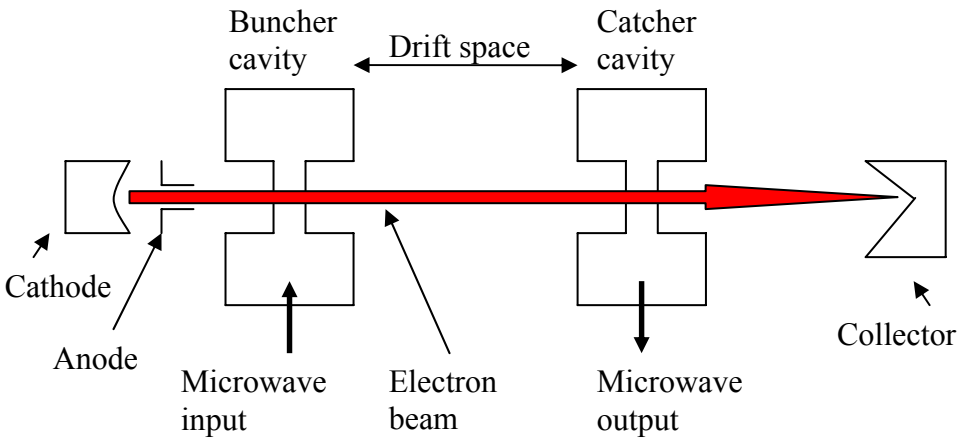

Figure A2 Schematic of klystron.

The travelling-wave tube

This device is a linear-beam microwave tube and the invention of the travelling wave tube amplifier (TWT) was by R. Kompfner in 1944. This electron tube uses velocity modulation to achieve amplification of a microwave signal [Gilmour 1994, Pierce 1950]. A thermionic cathode emits electrons which are accelerated toward a large potential on the collector. The signal to be amplified is applied at the waveguide input and travels along the helix. The coil of the helix is fairly long and, at microwave frequencies, our wavelength is very small, so many RF cycles will occur within the length of the helix. These cycles set up electromagnetic fields that interact with the electron stream travelling from the cathode to anode. At points where the RF voltage is positive, nearby electrons are accelerated; where the RF voltage is negative, the electrons are slowed down. Bunches of electrons are produced all along the tube within the helix. As bunches of electrons move towards the collector their charges induce voltages in the helix that add to the electromagnetic waves of the RF input signal resulting in an amplified output signal.

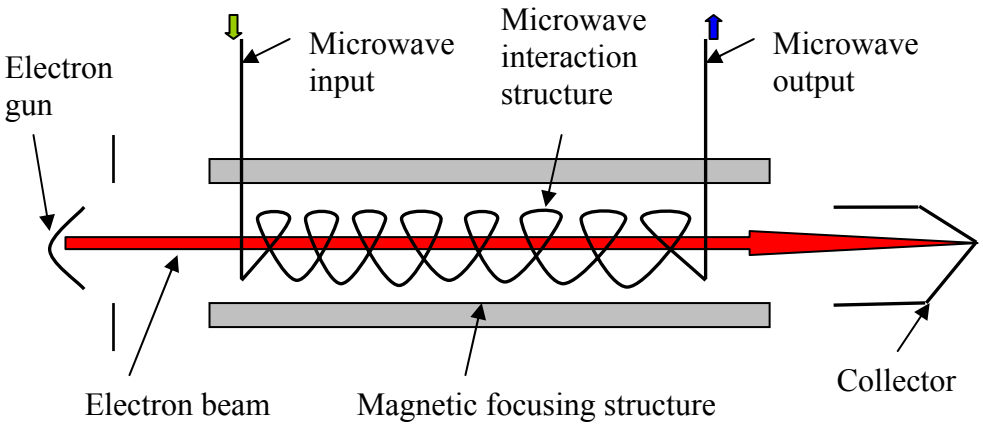

Figure A3 Schematic of travelling wave tube (TWT).

The backward-wave oscillator

Backward wave oscillators (BWOs) were developed in the 1940s and have the same basic structure as the travelling-wave tube. An electron gun generates an electron beam that interacts with a slow-wave structure. Oscillations are sustained by the propagation of a travelling wave against the beam direction. This amplified wave is extracted at the gun end.

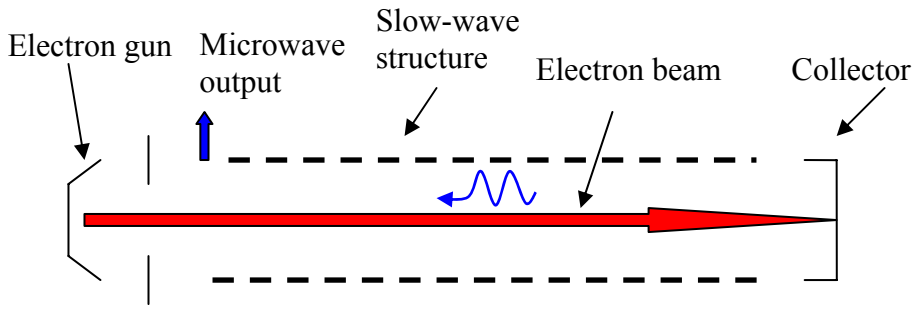

Figure A4 Schematic of backward wave oscillator (BWO).

The BWO is voltage–tuneable; by changing the voltage, the BWO can be tuned rapidly over a very wide range of frequencies. The BWO produces an extremely clean signal, with the desired output signal being at least 60 dB larger than the total of all the spurious frequencies. At X-band frequencies BWOs can produce gigawatt output powers of microwave radiation [Barker 2001, Tsimring 2007].

The free electron laser

A free electron laser (FEL) is a laser that emits high power coherent radiation at microwave frequencies and beyond, [Freund 1992]. Hans Motz proposed the 'wiggler' magnet configuration (an array of magnets with alternating poles) which is a critical feature of the FEL, [Motz 1951]. The FEL uses a relativistic electron beam as the lasing medium which moves freely through the magnetic 'wiggler' structure. The relativistic electron beam passes through the 'wiggler' which by the Lorentz force causes the electrons in the beam to follow a sinusoidal path. The acceleration of electrons along this path results in the release of synchrotron radiation in the forward

direction. Since the electron motion is in phase with the field of the wave already emitted, the fields add together coherently.

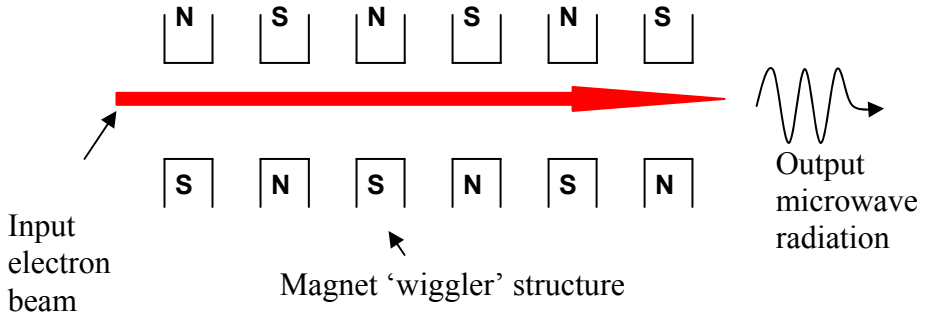

Figure A5 Schematic of free electron laser (FEL).

The gyrotron

The history of the gyrotron dates back to the late 1950s when a theory for the device was proposed by R. Q. Twiss and J. Schneider, [Twiss 1958]. The gyrotron [Flyagin 1977] is a type of free electron maser (microwave amplification by stimulated emission of radiation) and is a fast-wave device, since the phase velocities of the simple circuits (such as ordinary waveguide) are faster than the velocity of light ($v_p > c$), rather than the slow wave devices, such as the microwave devices mentioned above (TWT, BWO). The bunching of the electrons depends on a relativistic effect called the cyclotron maser instability, [Hirshfield 1964, 1977]. An electron beam is produced in a hollow-beam electron gun and then transported in a compression system composed of an axisymmetric magnetic field according to the adiabatic invariant $v_\perp^2/B = \text{constant}$, where $v_\perp$ is the Larmor orbit velocity and B is the magnetic field strength. This is a magnetic mirror effect similar to that used to confine plasmas, where perpendicular, azimuthal electron energy is increased at the expense of longitudinal drift energy. In the interaction space the electrons are guided by highly uniform fields. Magnetic coupling to the RF cavity fields is responsible for the microwave amplification and after completing interaction the electrons settle on an extended collector surface in a region of weaker magnetic field.

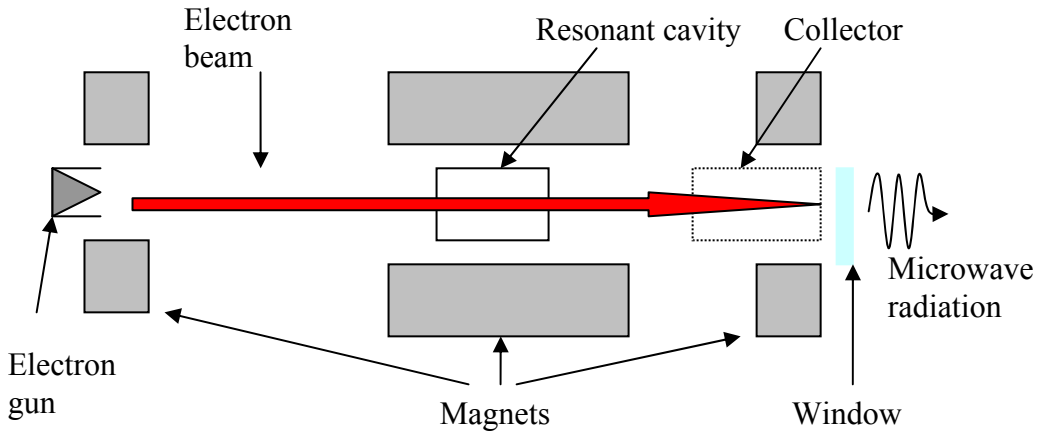

Figure A6 Schematic of gyrotron.

The gyrotron family [Edgcombe 1993] of devices includes the gyro-travelling-wave tube (gyro-TWT) and the gyro-backward-wave oscillator (gyro-BWO).

Appendix B

The physics of electromagnetic waves in the presence of matter is presented, [Fleisch 2009].

Gauss's Law for Electric Fields

In the presence of an electric field within a dielectric material the field will force charges to become displaced creating an electric polarisation given by,

$$\underline{P} = N\underline{p} \qquad \textbf{Equation B-1}$$

where $\underline{P}$ is the electric polarisation, N is the number of molecules and $\underline{p}$ is the electric dipole moment. The bound charge (ρ_b) is a build up of charge within the dielectric material given by,

$$\rho_b = -\underline{\nabla} \circ \underline{P} \qquad \textbf{Equation B-2}$$

Gauss's law in free-space is given by $\underline{\nabla} \circ \underline{E} = \rho/\varepsilon_0$. Where the charge density (ρ) is comprised of contributions from bound charge (ρ_b) and free charge (ρ_f) where $\rho = \rho_f + \rho_b$ therefore Gauss's law may be written as,

$$\underline{\nabla} \circ \underline{E} = \frac{\rho}{\varepsilon_0} = \frac{\rho_f + \rho_b}{\varepsilon_0} \qquad \textbf{Equation B-3}$$

Substituting equation B-2 for ρ_b and multiplying equation B-3 by ε_0 gives,

$$\underline{\nabla} \circ \varepsilon_0 \underline{E} = \rho_f + \rho_b = \rho_f - \underline{\nabla} \circ \underline{P} \qquad \textbf{Equation B-4}$$

Re-arranging equation B-4 gives,

$$\underline{\nabla} \circ \left(\varepsilon_0 \underline{\mathrm{E}} + \underline{\mathrm{P}}\right) = \rho_{\mathrm{f}}$$ **Equation B-5**

The term in the brackets is the electric displacement $\underline{D}$ where $\underline{\mathrm{D}} = \varepsilon_0 \underline{\mathrm{E}} + \underline{\mathrm{P}}$, thus Gauss's law for electric fields in matter can be written as,

$$\underline{\nabla} \circ \underline{D} = \rho_f$$ **Equation B-6**

Ampere- Maxwell Law

The $\underline{J}$ in the Ampere-Maxwell law is dependent on bound currents ($\underline{J}_b$), free currents ($\underline{J}_f$) and polarisation currents ($\underline{J}_P$). The bound current density is given by,

$$\underline{\mathrm{J}}_{\mathrm{b}} = \underline{\nabla} \times \underline{\mathrm{M}}$$ **Equation B-7**

where $\underline{\mathrm{M}}$ represents the magnetisation of the material.

The polarisation current density is given by,

$$\underline{\mathrm{J}}_{\mathrm{P}} = \frac{\partial \underline{\mathrm{P}}}{\partial \mathrm{t}}$$ **Equation B-8**

The total current density $\underline{J}$ is given by $\underline{\mathrm{J}} = \underline{\mathrm{J}}_{\mathrm{f}} + \underline{\mathrm{J}}_{\mathrm{b}} + \underline{\mathrm{J}}_{\mathrm{P}}$ and the Ampere-Maxwell law may be given as,

$$\underline{\nabla} \times \underline{\mathrm{B}} = \mu_0 \left(\underline{\mathrm{J}}_{\mathrm{f}} + \underline{\mathrm{J}}_{\mathrm{b}} + \underline{\mathrm{J}}_{\mathrm{P}} + \varepsilon_0 \frac{\partial \underline{\mathrm{E}}}{\partial \mathrm{t}} \right)$$ **Equation B-9**

Substituting equation B-7 for $\underline{J}_b$ and equation B-8 for $\underline{J}_p$ and dividing by μ_0 in equation B-9 gives,

$$\frac{1}{\mu_0}\underline{\nabla}\times\underline{\mathrm{B}}=\mathrm{J_f}+\underline{\nabla}\times\underline{\mathrm{M}}+\frac{\partial\underline{\mathrm{P}}}{\partial\mathrm{t}}+\varepsilon_0\frac{\partial\underline{\mathrm{E}}}{\partial\mathrm{t}}$$ **Equation B-10**

Re-arranging equation B-10 gives,

$$\underline{\nabla}\times\left(\frac{\underline{\mathrm{B}}}{\mu_0}-\underline{\mathrm{M}}\right)=\underline{\mathrm{J}}_\mathrm{f}+\frac{\partial\left(\varepsilon_0\underline{\mathrm{E}}+\underline{\mathrm{P}}\right)}{\partial\mathrm{t}}$$ **Equation B-11**

The term in brackets is the magnetic field intensity $\underline{H}$ where $\underline{\mathrm{H}}=\frac{\underline{\mathrm{B}}}{\mu_0}-\underline{\mathrm{M}}$ and the Ampere-Maxwell law in matter is given by,

$$\underline{\nabla}\times\underline{H}=\underline{J}_f+\frac{\partial\underline{D}}{\partial t}$$ **Equation B-12**

Gauss's law for magnetic fields and Faraday's law don't change as these equations have no direct involvement with charge or current. To that extent Maxwell's equations in matter are shown immediately below,

$$\underline{\nabla}\circ\underline{D}=\rho_f$$ **Equation B-13 Gauss's law for electric fields**

$$\underline{\nabla}\circ\underline{B}=0$$ **Equation B-14 Gauss's law for magnetic fields**

$$\underline{\nabla}\times\underline{E}=-\frac{\partial\underline{B}}{\partial t}$$ **Equation B-15 Faraday's law**

$$\underline{\nabla}\times\underline{H}=\underline{J}_f+\frac{\partial\underline{D}}{\partial t}$$ **Equation B-16 Ampere-Maxwell law**

Appendix C

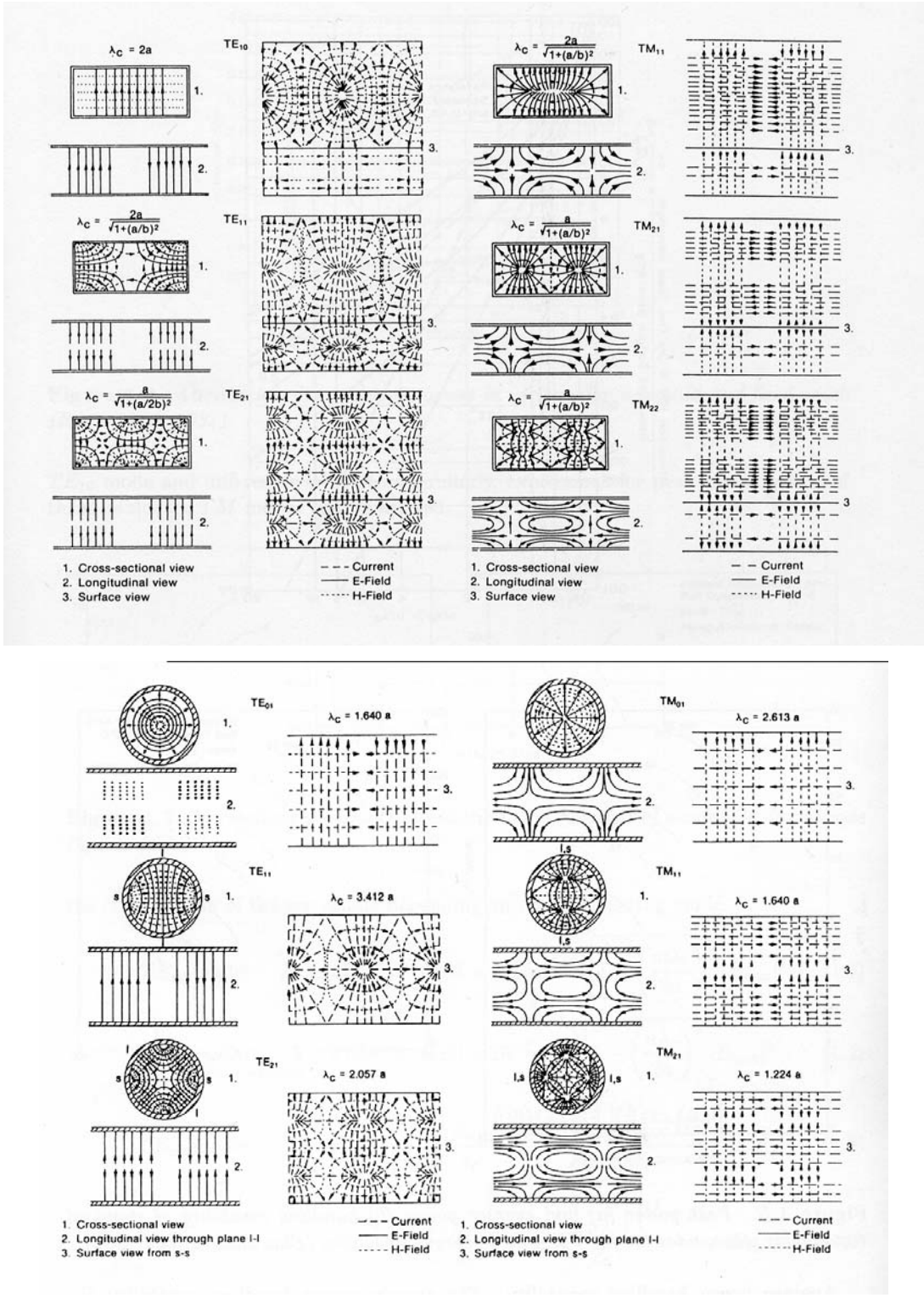

Figure C1 Mode patterns for the rectangular and circular waveguide, [Thumm 1997].

Appendix D

* In the code the 3-fold helix mode 1 is the $TE_{2,1}$ and mode 2 is the $TE_{1,1}$
# In the code the 5-fold helix mode 1 is the $TE_{2,2}$ and mode 2 is the $TE_{3,1}$

```
clear all;

%Waveguide geometry
cm = 10^(-2);
c = 3.0E8;
f_unit = 1E9;
r0 = 1.47*cm; % average radius of helix
r1 = 0.14*cm; % corrugation depth of helix
d = 2.89*cm; % period

% Azimuthal components
m1 = 2;  %  mode1
m2 = -1;  % mode2

% Roots of Bessel function
Z1 = 3.054; %  mode1
Z2 = 1.841; %  mode2

% Cut-off frequency wavevector for mode2
k1 = Z2/r0;

% Cut-off frequency wavevector for mode1
k0 = Z1/r0;

% Bragg axial wavenumber
kb = 2*pi/d;

%Normalised Bragg axial wavenumber
kb_norm = kb/k0
N=100; %Number of data points
h=linspace(-100,50,N);
h_cm = h * cm;

%Plot the electromagnetic waves
k_TE21=sqrt(k0.^2+(h).^2);
k_TE11=sqrt(k1.^2 + (h).^2);
k_TE11_1 = sqrt(k1.^2 + (h + kb).^2);
f_TE21 =  k_TE21 * c / (2 * pi) / f_unit;
f_TE11 =  k_TE11 * c / (2 * pi) / f_unit;
f_TE11_1 = k_TE11_1 * c / (2 * pi) / f_unit;
plot(h_cm,f_TE21,'r',h_cm,f_TE11,'b',h_cm,f_TE11_1,'g');
xlabel('wave number cm^-1')
grid on;
```

```
hold on;

% Calculate the intersection point
kzj = -((k0^2)-(k1^2)-(kb^2))/(2*kb);
kzl = kb - kzj;
k = (k1^2 + kzj^2)^0.5;

%Calculate the coupling coefficient
Kapa_right = r1/(r0^3);
Kapa_Up_1 =  (Z1^2) *  (Z2^2);
Kapa_Up_2_1 =  m1 * m2 * (r0^2);
Kapa_Up_2_2 = - kzl * kzj + k ^2 ;
Kapa_Down  =  sqrt((Z2^2-m2^2)*(Z1^2-m1^2));
Kapa_1 = Kapa_right .* (Kapa_Up_1 + Kapa_Up_2_1 * Kapa_Up_2_2)./
Kapa_Down;
mcoeff = 1.8;
Kapa = Kapa_1 * mcoeff;
sigma_un = Kapa .^2;

%Find roots of polynomial
order_4 = 1 .* ones(1,length(h));
order_3 =0 .* ones(1,length(h));
order_2 = -((h.^2 + k0.^2) + (h + kb).^2 + k1.^2);
order_1 = 0 .* ones(1,length(h));
order_0 =(h.^2 + k0.^2) .* (k1.^2 + (h + kb).^2) - sigma_un; % +/-
coef = [order_4' order_3' order_2' order_1' order_0'];
k_disp_temp = (-(order_2.^2/4 - order_0).^0.5 - order_2/2) .^ 0.5;
k_disp = k_disp_temp';
f_disp = k_disp * c / (2*pi)/f_unit;
h_cm = h_cm';
data_disp = [h_cm f_disp];
save ('data_disp.txt', 'data_disp', '-ascii', '-tabs')
f1 = f_disp*2 *pi *f_unit/c;
plot(h_cm, f_disp, 'k')
hold off;
xlabel('axial wavenumber (1/cm)');
ylabel('frequency (GHz)');
```

Appendix E

The following code is used to create the curve outline for face of the three-fold helix[1]

```
Sub Main ()
On Error GoTo Curve_Exists
Curve.NewCurve "3D-Analytical"
Curve_Exists:
On Error GoTo 0
Dim sCurveName As String
sCurveName = "3dpolygon_1"
With Polygon3D
  .Reset
  .Name sCurveName
  .Curve "3D-Analytical"
Dim xxx As Double, yyy As Double, zzz As Double, rrr as double, ttt As Double, nnn as double
a = 3 'azimuthal component'
r0 = 1.47 'mean radius in cm'
l = 0.14  'corrugation amplitude in cm'
For nnn = 1 To 361 STEP 1
ttt = (nnn-1)*(2*Pi/360)  't = theta in radians'
rrr=r0+l*Cos(a*ttt)       'r = radius for the helical profile'
xxx=rrr*Cos(ttt)
yyy=rrr*Sin(ttt)
zzz=0
.Point xxx,yyy,zzz
Next nnn
.Create
End With
End sub
```

[1] This macro can be used for the 5-fold helically corrugated waveguide by replacing azimuthal component, a with 5, average radius, r0 with 3.284 cm, and corrugation amplitude, l with 0.243 cm.

Appendix F

Polarisation

In the compression experiments elliptical waveguide polarisers are used to convert linearly polarised microwave radiation into circularly polarised radiation. In the case of the 3-fold helically corrugated waveguide compressor the linearly polarised $TE_{1,1}$ wave is converted to a left-circularly polarised $TE_{1,1}$ wave and transported in the 3-fold helix. For the 5-fold helically corrugated waveguide compressor the linearly polarised $TE_{1,1}$ wave is converted to a left-circularly polarised $TE_{1,1}$ wave to enter the mode converter and from the mode converter a right-circularly polarised $TE_{3,1}$ wave is transported in the 5-fold helix. Below is a brief outline of the physics of linear polarisation and circular polarisation.

Linear Polarisation

The polarisation of a wave describes the behaviour of the electric field in the x-y plane, [Hecht 1987]. A plane wave can be described by the following equation,

$$\underline{E}_0 = E_{0x}\,\underline{\hat{i}} + E_{0y}\,\underline{\hat{j}} \qquad \textbf{Equation F-1}$$

where $\underline{E}_0$ is the electric field amplitude and E_{0x} and E_{0y} are constant where $\underline{\hat{i}}$ and $\underline{\hat{j}}$ are unit vectors in the x and y directions respectively. The direction of the electric field polarisation is given by,

$$\tan\theta = \frac{E_{0y}}{E_{0x}} \qquad \textbf{Equation F-2}$$

Since E_{0x} and E_{0y} are in phase, θ must be constant, (Figure F1).

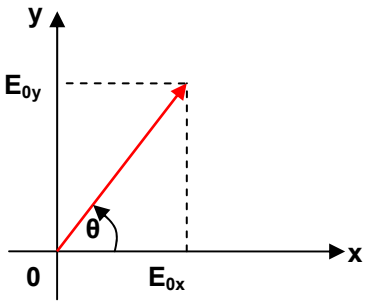

Figure F1 The electric field vector in a plane wave that is linearly polarised.

If the waves are propagating in the z-direction the components of the electric field are given by,

$$\underline{E}_x(z,t) = \hat{\underline{i}}E_{0x}\cos(kz - \omega t) \qquad \textbf{Equation F-3}$$

and

$$\underline{E}_y(z,t) = \hat{\underline{j}}E_{0y}\cos(kz - \omega t + \phi) \qquad \textbf{Equation F-4}$$

where ϕ is the relative phase difference between the waves.

The resultant vector of the two perpendicular waves is given by,

$$\underline{E}(z,t) = \underline{E}_x(z,t) + \underline{E}_y(z,t) \qquad \textbf{Equation F-5}$$

If $\phi = 0$ or an integer multiple of $\pm 2\pi$ the waves are in phase and the resultant vector sum of these two waves is given by,

$$\underline{E} = \left(\hat{\underline{i}}E_{0x} + \hat{\underline{j}}E_{0y}\right)\cos(kz - \omega t) \qquad \textbf{Equation F-6}$$

The resultant wave has fixed amplitude $\left(\hat{\underline{i}}\underline{E}_{0x} + \hat{\underline{j}}\underline{E}_{0y}\right)$ and is linearly polarised.

If ϕ is an odd integer multiple of $\pm\pi$ the two waves are 180˚ out of phase and

$$\underline{E} = \left(\hat{\underline{i}}E_{0x} - \hat{\underline{j}}E_{0y}\right)\cos(kz - \omega t) \qquad \textbf{Equation F-7}$$

the resultant wave is again linearly polarised.

Circular Polarisation

If both constituent waves have the equal amplitude where $E_{0x} = E_{0y} = E_0$ and their relative phase difference $\phi = -\frac{\pi}{2} + 2m\pi$, where $m = 0, \pm 1, \pm 2, \pm 3..$ the resultant wave is no longer linearly polarised and now have,

$$\underline{E}_x(z,t) = \underline{\hat{i}} E_0 \cos(kz - \omega t) \qquad \textbf{Equation F-8}$$

and

$$\underline{E}_y(z,t) = \underline{\hat{j}} E_0 \sin(kz - \omega t) \qquad \textbf{Equation F-9}$$

Thus the resultant vector sum is given by,

$$\underline{E} = E_0\left[\underline{\hat{i}} \cos(kz - \omega t) + \underline{\hat{j}} \sin(kz - \omega t)\right] \qquad \textbf{Equation F-10}$$

The direction of $\underline{E}$ is time-varying and rotating with angular frequency (ω) and the wave will be right circularly polarised, (Figure F2).

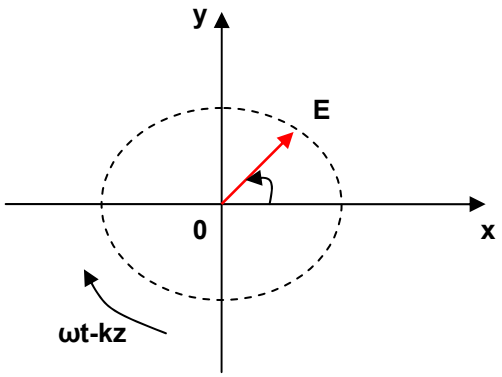

Figure F2 The electric field vector in a plane wave that is circularly polarised.

The term right-circular polarisation refers to the electric field vector rotating clockwise as viewed by an observer toward whom the wave is moving.

If $\phi = \frac{\pi}{2} + 2m\pi$ where again $m = 0,\pm1,\pm2,\pm3..$ then we have,

$$\underline{E} = E_0\left[\underline{\hat{i}}\cos(kz - \omega t) - \underline{\hat{j}}\sin(kz - \omega t)\right] \qquad \textbf{Equation F-11}$$

the electric field vector is now left-circularly polarised and is rotating counter clockwise.

By using the elliptical polarisers the electric field polarisation can be converted from linear to circular, (Figure F3).

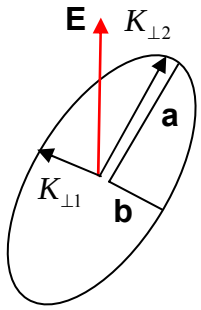

Figure F3 Schematic of elliptical structure of polariser.

$K_{\perp 1}$ and $K_{\perp 2}$ are the wave number components of the linearly polarised electric field vector and 'a' and 'b' are the waveguide dimensions in the x and y directions respectively which for an elliptical waveguide correspond to the major axis ('a') and minor axis ('b'). The wavenumber components are given by,

$$K_{\perp 1} = \frac{\zeta'_{m,n}}{a} \qquad \textbf{Equation F-12}$$

$$K_{\perp 2} = \frac{\zeta'_{m,n}}{b} \qquad \textbf{Equation F-13}$$

where $\zeta'_{m,n}$ are roots of the Bessel function for the TE modes.

The elliptical nature of the polariser gives the following relationship,

$$\frac{K_{\perp 1}}{K_{\perp 2}} = \frac{a}{b} \qquad \textbf{Equation F-14}$$

where $K_{z1} = \sqrt{K^2 - K_{\perp 1}^2}$ and $K_{z2} = \sqrt{K^2 - K_{\perp 2}^2}$

The phase difference created by the elliptical polariser is given by,

$$\varphi = (K_{z1} - K_{z2})L \qquad \textbf{Equation F-15}$$

where L is the length of the elliptical polariser.

From a practical point of view, in terms of the microwave pulse compression experiments carried out in the RF laboratory, the elliptical polarisers used in the experiments where labelled 'L' for major axis and 'S' for minor axis. The two elliptical polarisers, one at the input to the helical compressor and one at the output of the helical compressor had to be 'crossed' with one another i.e. the major axes of the two polarisers were 90˚ to one another and similarly with the minor axes which were also at 90˚ to one another.

Appendix G

```
=========================================================================
% Wideband non-linear chirp
=========================================================================
clear all
close all
=========================================================================
% SCRIPT OPTIONS
=========================================================================
% -------------------------------------------------------------------
% Signal download?
% -------------------------------------------------------------------
reply = input('Enable signal download to N6030? Y/N [Y]: ', 's');
if isempty(reply)
    reply = 'Y';
end

if upper(reply)=='Y'
    dLoad=1;
else
    dLoad=0;
end
% -------------------------------------------------------------------
% Save bin files?
% -------------------------------------------------------------------
reply = input('Save waveform binaries? Y/N [Y]: ', 's');
if isempty(reply)
    reply = 'Y';
end

if upper(reply)=='Y'
    dSaveWav=1;
else
    dSaveWav=0;
end
% -------------------------------------------------------------------
% Plot waveforms?
% -------------------------------------------------------------------
reply = input('Plot waveforms? Y/N [Y]: ', 's');
if isempty(reply)
    reply = 'Y';
end

if upper(reply)=='Y'
    dPlot=1;
else
    dPlot=0;
end
% -------------------------------------------------------------------
% Apply corrections
% -------------------------------------------------------------------
reply = input('Apply corrections Single|Amplified|None [S]: ', 's');
if isempty(reply)
    reply = 'S';
end
if upper(reply)=='S'
    dCorr=0;
```

```
elseif upper(reply)=='A'
    dCorr=1;
else
    dCorr=2;
end
% PSG centre frequency: set somewhere between 9.1 GHz to 9.6 GHz
Fo=9.3e9;
% Number of padding zeros (sets the duty cycle)
% Note select Npad>400
Npad=512;
% Setup filenames for signal and correction files
File_Signal=[pwd '\signal.txt'];
if dCorr==0
    File_Corr=[pwd '\se500.txt'];
elseif dCorr==1
    File_Corr=[pwd '\amp500.txt'];
else
    File_Corr=' ';
end
% Setup filenames for output
if dSaveWav==1
   if dCorr==0
        IbinFile=[pwd '\demoSE_Isig'];
        QbinFile=[pwd '\demoSE_Qsig'];
   elseif dCorr==1
       IbinFile=[pwd '\demoAMP_Isig'];
       QbinFile=[pwd '\demoAMP_Qsig'];
   else
       IbinFile=[pwd '\demoNOCORR_Isig'];
       QbinFile=[pwd '\demoNOCORR_Qsig'];
   end
end
%=========================================================================
% SIGNAL GENERATION
%=========================================================================
disp('Generating signal...');

Fs=1.25e9;      % Sample rate
Ts=1/Fs;        % Sample interval
% -----------------------------------
% Load signal parameters from txt file
% -----------------------------------
A=load(File_Signal);
F=A(:,1)*1e9;       % Frequency profile
M=A(:,2);           % Amplitude profile

DF=F-Fo;            % Delta frequency
% -----------------------------------
% Generate phase profile and I/Q
% -----------------------------------
phi=(2*pi/Fs)*cumsum(DF);
Isig=M.*cos(phi);
Qsig=M.*sin(phi);
Tsig=Isig+j*Qsig;

% ---------------------------------------
% PAD signal with zeros to set duty cycle
% ---------------------------------------
NZ=8*round((length(Isig)+Npad)/8)-length(Isig);
```

```
disp(['Number of actual pad zeros: ' num2str(NZ)]);
disp(['Total number of samples:    ' num2str(NZ+length(Isig)) ]);
PADpre=zeros(1,64);
PADpost=zeros(1,NZ-64);
IsigP=[PADpre Isig' PADpost];
QsigP=[PADpre Qsig' PADpost];
TsigP=IsigP+j*QsigP;
% ----------------------------------------
% Load frequency response correction file
% and perform corrections
% ----------------------------------------
if dCorr<2
    disp('Performing frequency response corrections...');
    C=load(File_Corr);
    Icorr=arbcorr(IsigP,C);
    Qcorr=arbcorr(QsigP,C);
    TsigPCorr=Icorr+j*Qcorr;
else
    Icorr=IsigP;
    Qcorr=QsigP;
    TsigPCorr=TsigP;
end
%Format for download
TsigPCorrD=[Icorr ; Qcorr];
% ----------------------------------------
% Save waveform files (optional step)
% ----------------------------------------
if dSaveWav==1
    disp('Save binary waveforms: STARTING')
    disp('Save I signal: STARTED');
    [errNum, desc] = agt_awg_savebin(IbinFile,Icorr);
    disp(['Save I signal: ' num2str(errNum)]);

    disp('Save Q signal: STARTED');
    [errNum, desc] = agt_awg_savebin(QbinFile,Qcorr);
    disp(['Save Q signal: ' num2str(errNum)]);
end
=========================================================================
% PLOT WAVEFORMS
=========================================================================
if dPlot==1;
    T=(0:length(Isig)-1)*Ts*1e9;
    figure
    subplot(2,1,1)
    plot(T,abs(Isig+j*Qsig));
    ylim([-0.1 1.1]);
    ylabel('Amplitude');
    grid on;
    subplot(2,1,2)
    plot(T,DF/1e9);
    ylim([min(DF/1e9)-0.1 max(DF/1e9)+0.1])
    ylabel('Freq (GHz)');
    xlabel('Time (ns)');
    grid on
    %figure
    %plot(abs(TsigCorr))
    %grid on
end
=========================================================================
```

```
% SIGNAL DOWNLOAD
% Open session
% Download waveform
% Enable output, set to arb mode
% Output config=SE
% Output filter: ON
% Output filter setting: 500 MHz
% Start playback
% Close session
=====================================================================
if dLoad==1
    disp('Downloading signal to N6030A');
    disp('Open N6030A session: STARTING');
    [instrH,errNum,errMsg]=agt_awg_open('pci','PXI*::*');
    disp(['Open N6030A session: ' errMsg]);
    disp('Waveform download: STARTING')
    [waveH,errNum,errMsg]=agt_awg_storewaveform(instrH,TsigPCorrD);
    disp(['Waveform download: ' errMsg]);
    disp('Enable instrument state: STARTING');
    [errNum,errMsg]=agt_awg_setstate(instrH,'outputenabled','true');
    disp(['Enable instrument state: ' errMsg]);
    disp('Setting to arb mode: STARTING');
    [errNum,errMsg]=agt_awg_setstate(instrH,'outputmode','arb');
    disp(['Setting to arb mode: ' errMsg]);
    if dCorr==0
    disp('Configuring SE output: STARTING');
    [errNum,errMsg]=agt_awg_setstate(instrH,'outputconfig','se');
    % diff(differential)|se(single ended)|amp(amplified se)
    disp(['Configuring SE output: ' errMsg]);
    elseif dCorr==1
    disp('Configuring AMP output: STARTING');
    [errNum,errMsg]=agt_awg_setstate(instrH,'outputconfig','amp');
    % diff(differential)|se(single ended)|amp(amplified se)
    disp(['Configuring AMP output: ' errMsg]);
    end
        disp('Enable output filter: STARTING');
[errNum,errMsg]=agt_awg_setstate(instrH,'outputfilterenabled','true'
);
    % true | false
    disp(['Enable output filter: ' errMsg]);
        disp('Set filter to 500e+6: STARTING');
    [errNum,errMsg]=agt_awg_setstate(instrH,'outputbw',500000000);
    % 250e6|500e6
    disp(['Set filter to 500e+6: ' errMsg]);
    disp('Playback: STARTING');
    [errNum,errMsg]=agt_awg_playwaveform(instrH,waveH);
    disp(['Playback: ' errMsg]);
    disp('Close session: STARTING');
    [errNum,errMsg]=agt_awg_close(instrH);
    disp(['Close session: ' errMsg]);
end%
```

Appendix H

```
%start
clear all;
%variables
df=(10-8.8)/500;
f=[8.8:df:10];
%read in the input pulse
[time,input]=textread('pulse1.dat','%f %f','delimiter','   ');
Ts=(time(3)-time(1))/2; %sampling period.
%plot the input pulse
subplot(6,1,1), plot(time,input,'r-s')
title('Input pulse to helical waveguide')
xlabel('Time(ns)')
ylabel('Amplitude(V)')
legend('Input pulse')
axis tight
grid on

%Fourier transform F(f)
Phi=f'*time'; %matrix multiplication of the frequency and time.
F=(input'*exp(-i*2*pi*Phi)')*Ts; %Fourier transform operation.

%plot the Fourier components of F(f)
subplot(6,1,2),plot(f,real(F),'rx-',f,imag(F),'bo:',f,abs(F),'g*--')
title('Components of the Fourier transform')
xlabel('Frequency(GHz)')
ylabel('F(f)')
legend('real','imag','abs')
axis tight
grid on

%Inverse Fourier transform
Phi=(f-9)'*time'; %matrix multiplication of the heterodyne frequency and time
IF=2*(exp(i*2*pi*Phi')*F')*df; %inverse Fourier transform

%plot the inverse Fourier components of F(f)
subplot(6,1,3), plot(time,real(IF),'rx-',time,imag(IF),'bo:',time,abs(IF),'g*--')
title('Components of the inverse Fourier transform')
xlabel('Time(ns)')
ylabel('IF')
legend('real','imag','abs')
axis tight
grid on

%phase evolution of the pulse
phase=atan(imag(IF)./real(IF)); %phase evolution in radians
```

```
%plot the phase vs time of the pulse (phase evolution)
subplot(6,1,4),plot(time,phase)
title('Phase evolution of pulse')
xlabel('Time(ns)')
ylabel('Phase(radians)')
legend('Phase evolution')
axis ([-20 100 -pi/2 pi/2])
grid on

%frequency sweep of the pulse (rate of change of phase with time)
N=length(time);
J=[3:1:N]';
time1=J*Ts+time(1);
frequency=9+(phase(J)-phase(J-2))/Ts/4/pi;

%read in optimised sweep from AWG
[time2,input2]=textread('AWG_sweep.dat','%f %f','delimiter','   ');

%plot the input pulse
subplot(6,1,5), plot(time2,input2,'r.')
title('Optimum sweep produced on AWG')
xlabel('Time(ns)')
ylabel('Frequency (GHz)')
legend('Op-sweep')
axis ([-20 100 9 10])
grid on

%plot the frequency vs time of the pulse (phase evolution)
subplot(6,1,6),plot(time1,frequency,'b.',time2,input2,'r.')
title('Rate of change of pulse with time')
xlabel('Time(ns)')
ylabel('Frequency(GHz)')
legend('Frequency sweep')
axis ([-20 100 9 10])
grid on

%end
```

Appendix I

1. M. McStravick, S.V. Samsonov, K. Ronald, S.V. Mishakin, W. He, G.G. Denisov, C.G. Whyte, V.L. Bratman, A.W. Cross, A.R. Young, P. MacInnes, C.W. Robertson, and A.D.R. Phelps, *Experimental results on microwave pulse compression using helically corrugated waveguide*, J. Appl. Phys., **108**, 054908 (2010).

2. V.L Bratman, G.G. Denisov, N.G. Kolganov, S.V. Mishakin, S.V. Samsonov, A.W. Cross, W. He, L. Zhang, M. McStravick, C.G. Whyte, A.R. Young, K. Ronald, C.W. Robertson, and A.D.R. Phelps, *Generation of 3 GW microwave pulses in X-band from a combination of a relativistic backward-wave oscillator and a helical-waveguide compressor*, Physics of Plasmas **17**, 110703 (2010).

Experimental results on microwave pulse compression using helically corrugated waveguide

M. McStravick,[1,a)] S. V. Samsonov,[2] K. Ronald,[1] S. V. Mishakin,[2] W. He,[1] G. G. Denisov,[2] C. G. Whyte,[1] V. L. Bratman,[2] A. W. Cross,[1] A. R. Young,[1] P. MacInnes,[1] C. W. Robertson,[1] and A. D. R. Phelps[1]
[1]*SUPA, Department of Physics, University of Strathclyde, Glasgow G4 0NG, Scotland, United Kingdom*
[2]*Institute of Applied Physics, Russian Academy of Sciences, Nizhny Novgorod 603950, Russia*

(Received 21 June 2010; accepted 26 July 2010; published online 15 September 2010)

The paper presents new results on the development of a method to generate ultrahigh-power short-microwave pulses by using a known principle of compression (reduction in pulse duration accompanying with increase in pulse amplitude) of a frequency-swept wave packet propagating through a dispersive medium. An oversized circular waveguide with helical-corrugations of its inner surface ensures an eigenwave with strongly frequency dependent group velocity far from cutoff. These dispersive properties in conjunction with high rf breakdown strength and low Ohmic losses make a helically corrugated waveguide attractive for increasing microwave peak power. The experiments performed at kilowatt power levels, demonstrate that an X-band microwave pulse of 80 ns duration with a 5% frequency sweep can be compressed into a 1.5 ns pulse having 25 times higher peak power by optimizing the frequency modulation of the input wave packet.
 [doi:10.1063/1.3482024]

I. INTRODUCTION

Research into high-power, short-duration, microwave pulses for a range of applications including particle accelerators, telecommunications, radar technology, and plasma chemistry is an active area of microwave science.[1,2] Various methods can be used to generate peak powers at centimeter and millimeter wavelengths from vacuum electronic devices. One method is to increase the power of electron beams up to a few mega electron volts and tens of kiloamperes,[3] however this makes the installations very problematic for user applications. Alternative advanced methods aimed at generating microwave pulses with the same peak power level but using substantially less intense electron beams has been developed, including the use of super radiance effects[4] and pulse compression (active and passive) both of which have recently demonstrated great promise (see e.g., Refs. 3 and 4, and references cited there).

II. HELICALLY CORRUGATED WAVEGUIDE

Helically corrugated waveguides have been studied and used as interaction regions in gyrotron traveling-wave tube (TWT) amplifiers[5–7] and in gyrotron backward-wave oscillators (BWOs).[8,9] As was shown in Ref. 10, the use of a metal overmoded circular waveguide with appropriate helical-corrugations of its inner surface [Fig. 1(a)] as a dispersive medium enables effective compression of monotonously frequency modulated microwave pulses. The region of operating parameters (frequency range, input pulse duration, and sweep interval) in conjunction with low reflection and high rf electric strength, make the helical-waveguide compressor attractive for increasing the peak power from powerful nonresonant electron devices such as relativistic BWOs and TWTs, up to extremely high-power levels.

The helical-corrugation couples a pair of circularly polarized partial modes of the smooth waveguide,[11] having significantly different group velocities: one mode [mode (1) in Fig. 1(b)] is far from cutoff and the other mode [mode (2) in

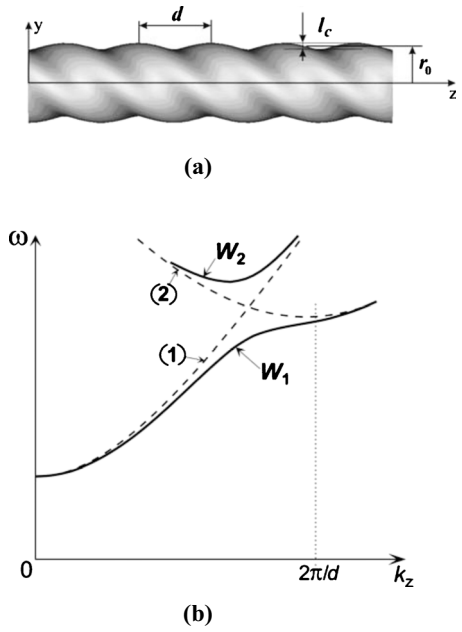

FIG. 1. (a) Helically corrugated waveguide (the surface equation in cylindrical coordinates is $r(\varphi,z)=r_0+l_c\cos(m_c\varphi+k_cz)$, where r_0 is the waveguide mean radius, l_c, m_c, and $k_c=2\pi/d$ are the amplitude, azimuthal, and axial numbers of the corrugation, respectively, and d is the corrugation period); (b) its dispersion diagram: (1) is a lower partial mode of a smooth waveguide, (2) is a spatial harmonic of a near-cutoff mode; W_1 and W_2 are the eigenmodes of the helical-waveguide.

[a)]Electronic mail: michael.mcstravick@strath.ac.uk.

Fig. 1(b)] is close to cutoff.[12] As a result in the region of their resonant coupling, an eigenmode appears having a strongly frequency dependent group velocity [mode W_1 in Fig. 1(b)], which is favorable for pulse compression. If the rf oscillations in an incident pulse are swept from a frequency having a low-group velocity to a frequency having a high-group velocity, the tail of the pulse will endeavor to overtake its leading edge when propagating through the waveguide, resulting in pulse shortening and corresponding growth in its amplitude if the losses are sufficiently small.

III. EXPERIMENT

The previous experiments,[13] using a nonoptimized frequency swept pulse, at kilowatt power levels showed that X-band radiation, of 70 ns duration, with 3% frequency modulation, can be compressed into a 3 ns pulse, having 10.9 times higher peak power and containing more than 44% of the input pulse energy. The theoretical analysis predicts further increase in the power compression ratio up to 20–30 times, by increasing the frequency sweep interval and using an optimum modulation of the input signal. This paper introduces the first compression measurements, where an optimally down-chirped input pulse was synthesized.

New pulse compression experiments were carried out at the University of Strathclyde in collaboration with the Institute of Applied Physics. The helically corrugated waveguide was constructed from copper and had threefold right-handed corrugations ($m_c=3$), which coupled the right-handed circularly polarized $TE_{2,1}$ near-cutoff mode with the left-handed circularly polarized $TE_{1,1}$ far from cutoff mode. The wave dispersion of the helically corrugated waveguide was measured using both scalar network analyzers and vector network analyzers (SNAs and VNAs)[14] (Fig. 2). The resultant eigenwave dispersion and corresponding group velocity dispersion were calculated using the measured data from the SNA and VNA. The losses of the compressor were measured as a function of frequency (using the SNA). Elliptical polarizers were used to ensure a circularly polarized $TE_{1,1}$ wave was launched into the helical compressor. The sharp peaks in the losses [Fig. 2(b)] measurement were due to small cavity effects of the elliptical polarizers.

In the experiments the input radiation was launched from an X-band (8.2–12.5 GHz) waveguide and proceeded through a rectangular-to-circular adapter then through an elliptical cross-sectional polarizer which converted the linearly polarized $TE_{1,1}$ mode to a circularly polarized mode. This mode was adiabatically transformed into the operating mode [Fig. 2(a)] passing through a four-period section with linearly increasing amplitude of the helical corrugation. At the output, the opposite transition occurred. The helical structure with parameters $r_0=14.7$ mm, $l_c=1.4$ mm, and $d=28.9$ mm had a total length of the regular helical-corrugation of 2.08 m. The compression experiments were carried out by programming an Agilent N6030A arbitrary waveform generator (AWG) to generate an optimized input signal, in the form of I and Q data, to the mixers of an Agilent E8267D vector signal generator (VSG). Real time diagnostics were facilitated by using a 12 GHz Tektronix

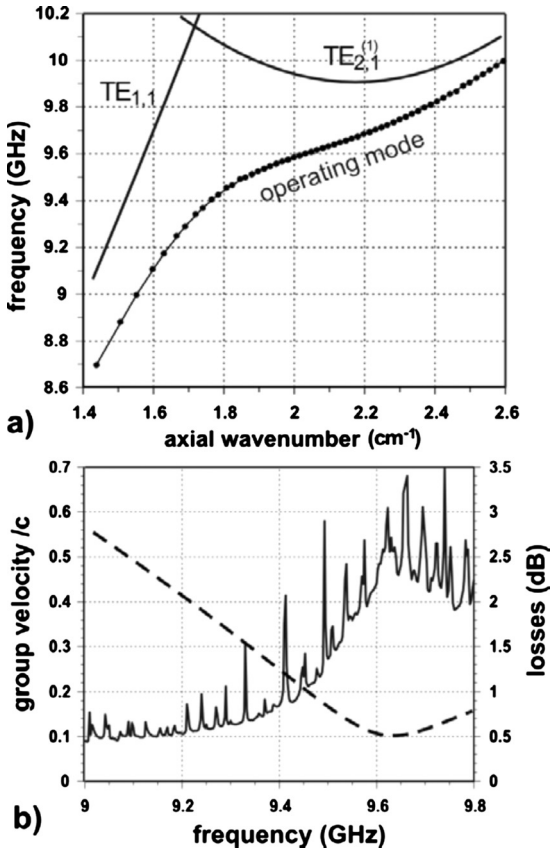

FIG. 2. Measured characteristics of helically corrugated waveguide used in the compression experiment: (a) dispersion; (b) group velocity of the operating mode (dashed line) and losses (solid line) for whole compressor.

TDS 6124C real time digitizing storage oscilloscope to monitor the input and output radiation signals of the compressor (Fig. 3). A conventional X-band TWT was used to amplify the radiation generated by the solid-state oscillators and mixers, up to a power of between 5 and 8 kW. The optimum frequency modulation of a quasirectangular input pulse was found from analysis of the measured helical-waveguide dispersion. The sweep started from the frequency corresponding to the minimum value of the group velocity (approximately 10% the speed of light at 9.61 GHz) and

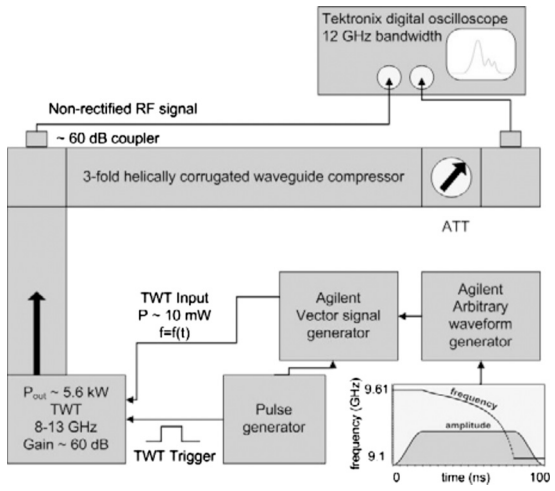

FIG. 3. Setup of the pulse compression experiment.

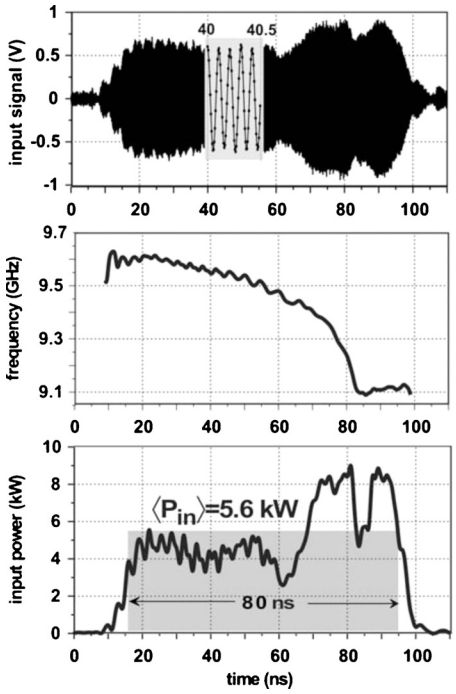

FIG. 4. Input pulse details for pulse compression experiment.

extended down to a frequency of higher group velocity (approximately 55% the speed of light at 9.10 GHz), in such a manner that the inverse group velocity was a linearly decreasing function of time over an input pulse whose duration was determined by the length of the waveguide. The required frequency sweep was processed by a MATLAB script incorporated into the controls of the AWG, which generated sweep-data for the two 500 MHz channels of the AWG. The two signals synthesized from the data by the AWG were used as inputs into I and Q wideband inputs of the VSG's mixer, with a 9.3 GHz local oscillator signal, to upmix the signal to produce a microwave pulse with a frequency sweep from 9.61 to 9.10 GHz in 80 ns at a maximum sweep rate of up to 20 MHz/ns. The measured frequency modulation coincided with the optimum frequency sweep (Fig. 4) predicted by theory.

IV. RESULTS

As a result, almost the maximum available (for this compressor) power compression ratio of 25 was achieved, with a 5.6 kW (averaged over the pulse), 80 ns duration microwave pulse, compressed to a 1.5 ns duration pulse with a peak power of 140 kW (Fig. 5). Approximately 50% of the input energy is compressed to the main body of the compressed pulse (assuming the main body as a Gaussian-shaped waveform with 1.5 ns full width half maximum) and approximately 25% of the energy is retained in the train of lower amplitude secondary pulses. Further experimental optimization of the input pulse (changing durations of the sweep, leading and falling edges, frequency interval, and its mean value) showed the possibility of substantial reduction in the energy retained in the secondary pulses (down to 7%–10% in energy) but at the expense of reduction in the power compression ratio down to 18–20. All the experimental results

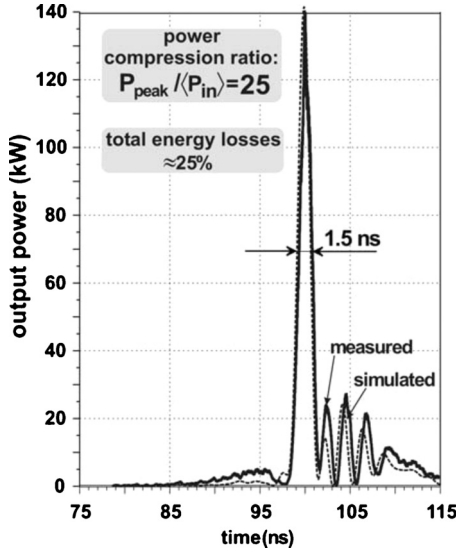

FIG. 5. Measured (solid line) and simulated (dashed line) compressed pulse.

were found to be in very good agreement with simulations (Fig. 5). The simulations of the output pulse were carried out in MATLAB using a double Fourier transform in which the data from the oscilloscope corresponding to the input pulse were used as an input waveform and the measured characteristics of the compressor (Fig. 2) were used to determine the frequency response of the medium.

V. CONCLUSION

Experiments involving detailed measurements and subsequent optimization of the input pulse chirp profile was carried out with a helical-waveguide compressor. Good agreement was achieved between theory and experiment providing improved understanding for further development of the concept and its application as a method of generation of ultrahigh-power microwave pulses. In particular, it was shown that X-band radiation of 80 ns duration with optimized 5% frequency modulation can be compressed into a 1.5 ns pulse with 25-fold power amplification.

ACKNOWLEDGMENTS

The authors thank the UK Engineering and Physical Sciences Research Council, the Russian Foundation for Basic Research (Grant No. 10-02-00975), and the Program of Presidium of Russian Academy of Sciences "Basic problems of relativistic pulsed and stationary high-power electronics" for supporting this work and Howard Smith of TMD Ltd. for the loan of the high-power TWT. We thank Dave Gamble of Dstl, UK, and Dr. Graeme Burt, Department of Engineering at University of Lancaster for useful scientific discussions.

[1]*Applications of High-Power Microwaves*, edited by A. V. Gaponov-Grekhov and V. L. Granatstein (Artech House, Norwood, MA, 1994).
[2]M. K. Thumm and W. Kasparek, IEEE Trans. Plasma Sci. **30**, 755 (2002).
[3]S. P. Bugaev, V. A. Cherepenin, V. I. Kanavets, A. I. Klimov, A. D. Kopenkin, V. I. Koshelev, V. A. Popov, and A. I. Slepkov, IEEE Trans. Plasma Sci. **18**, 525 (1990).
[4]A. A. Eltchaninov, S. D. Korovin, G. A. Mesyats, I. V. Pegel, V. V. Rostov, V. G. Shpak, and M. I. Yalandin, IEEE Trans. Plasma Sci. **32**, 1093 (2004).

[5]A. W. Cross, W. He, A. D. R. Phelps, K. Ronald, C. G. Whyte, A. R. Young, C. W. Robertson, E. G. Rafferty, and J. Thomson, Appl. Phys. Lett. **90**, 253501 (2007).
[6]G. G. Denisov, V. L. Bratman, A. W. Cross, W. He, A. D. R. Phelps, K. Ronald, S. V. Samsonov, and C. G. Whyte, Phys. Rev. Lett. **81**, 5680 (1998).
[7]V. L. Bratman, A. W. Cross, G. G. Denisov, W. He, A. D. R. Phelps, K. Ronald, S. V. Samsonov, C. G. Whyte, and A. R. Young, Phys. Rev. Lett. **84**, 2746 (2000).
[8]W. He, A. W. Cross, A. D. R. Phelps, K. Ronald, C. G. Whyte, S. V. Samsonov, V. L. Bratman, and G. G. Denisov, Appl. Phys. Lett. **89**, 091504 (2006).
[9]W. He, K. Ronald, A. R. Young, A. W. Cross, A. D. R. Phelps, C. G. Whyte, E. G. Rafferty, J. Thomson, C. W. Robertson, D. C. Speirs, S. V. Samsonov, V. L. Bratman, and G. G. Denisov, IEEE Trans. Electron Devices **52**, 839 (2005).
[10]S. V. Samsonov, A. D. R. Phelps, V. L. Bratman, G. Burt, G. G. Denisov, A. W. Cross, K. Ronald, W. He, and H. Yin, Phys. Rev. Lett. **92**, 118301 (2004).
[11]G. G. Denisov, V. L. Bratman, A. D. R. Phelps, and S. V. Samsonov, IEEE Trans. Plasma Sci. **26**, 508 (1998).
[12]S. J. Cooke and G. G. Denisov, IEEE Trans. Plasma Sci. **26**, 519 (1998).
[13]G. Burt, S. V. Samsonov, A. D. R. Phelps, V. L. Bratman, K. Ronald, G. G. Denisov, W. He, A. R. Young, A. W. Cross, and I. V. Konoplev, IEEE Trans. Plasma Sci. **33**, 661 (2005).
[14]G. Burt, S. V. Samsonov, K. Ronald, G. G. Denisov, A. R. Young, V. L. Bratman, A. D. R. Phelps, A. W. Cross, I. V. Konoplev, W. He, J. Thomson, and C. G. Whyte, Phys. Rev. E **70**, 046402 (2004).

Generation of 3 GW microwave pulses in X-band from a combination of a relativistic backward-wave oscillator and a helical-waveguide compressor

V. L. Bratman,[1] G. G. Denisov,[1] N. G. Kolganov,[1] S. V. Mishakin,[1] S. V. Samsonov,[1] A. W. Cross,[2] W. He,[2] L. Zhang,[2] M. McStravick,[2] C. G. Whyte,[2] A. R. Young,[2] K. Ronald,[2] C. W. Robertson,[2] and A. D. R. Phelps[2]
[1]*Institute of Applied Physics, Russian Academy of Sciences, Nizhny Novgorod 603950, Russia*
[2]*Department of Physics, Scottish Universities Physics Alliance, University of Strathclyde, Glasgow, Scotland G4 0NG, United Kingdom*

(Received 20 September 2010; accepted 5 October 2010; published online 2 November 2010)

The phenomenon of passive compression of frequency-modulated (FM) pulses in a dispersive media (DM) was used to increase the peak microwave power up to the multigigawatt level. A helically corrugated waveguide was used as the DM, while a relativistic X-band backward-wave oscillator (RBWO) with a descending-during-the-pulse accelerating voltage served as a source of FM pulses. Compression of pulses down to a halfwidth of 2.2 ns accompanied by a 4.5-fold power increase up to a value of about 3.2 GW has been demonstrated. © *2010 American Institute of Physics*.
[doi:10.1063/1.3505825]

Radio frequency (rf) pulses with multigigawatt peak power levels have recently become available owing to progress in relativistic vacuum electronics. Multigigawatt powers open up many opportunities for fundamental plasma studies and promising applications.[1] For example, the power of 8.7 GW if focused on an area of the order of the wavelength squared imparts a relativistic oscillatory velocity to electrons. In contrast with challenging ways of generating gigawatt power level radiation by increasing directly the power of electron beams up to a few MeVs and tens of kiloamperes,[2] some advanced methods using substantially less intense beams are being actively developed. Among these methods, results achieved based on superradiance effects[3] and pulse compression (active and passive) (see, e.g., Refs. 1 and 4–7 and references cited there) show great promise.

In a series of publications, the well-known phenomenon of passive pulse compression (reduction in duration accompanied with an increase in amplitude), widely used in optics (see, e.g., Refs. 8 and 9), has been proposed and investigated both theoretically and in low-power proof-of-principle experiments[6,7] as a method of achieving microwave radiation with multigigawatt peak powers. The method is based on generation of a frequency modulated (FM) pulse by a relativistic backward-wave oscillator (RBWO) following its compression due to propagation through a DM in the form of a hollow metallic waveguide with helical corrugation of the inner surface. In this letter we present the first pulse compression experiment in which multigigawatt peak power of X-band radiation has been achieved. The experimental setup comprises two key elements (Fig. 1): the source of FM radiation (an RBWO) and the DM [a helical-waveguide (HW) compressor].

A helical-waveguide compressor with appropriate parameters, namely, having a relatively shallow helical corrugation (periodical in both axial and azimuthal directions) of the inner wall of a waveguide with circular cross-section, can resonantly couple a pair of circularly polarized partial modes of the unperturbed waveguide, having significantly different group velocities where one mode is far from the cutoff and the other mode is close to cutoff.[6] As a result, in the frequency region of their resonant coupling, an eigenmode appears having a strong frequency dependent group velocity, which is favorable for the pulse compression. In contrast with a smooth or axially symmetric corrugated waveguide, the helical corrugation allows the frequency regions with zero or negative group velocity of the eigenwave to be avoided. This ensures good rf matching of the compressor to the input source over a suitably wide frequency band.

In the experiment under discussion, a fivefold sinusoidal corrugation was used which coupled a circularly polarized $TE_{3,1}$ mode having large group velocity with a near-cutoff counter-rotating $TE_{2,2}$ mode. The use of these relatively high-order modes ensured sufficient rf breakdown strength at the gigawatt power level.[7] The inner surface of the waveguide in cylindrical coordinates r, φ, and z had the following form: $r(\varphi,z)=31.5+2.7\sin(2\pi z/32.4-5\varphi)$ (all dimensions are in millimeters). The HW consisted of four aluminum sections and had a total length of the regular corrugation of 972 mm, bounded from each side by three-period sections with linearly increasing/decreasing amplitude of corrugation for adiabatic conversion of the radiation from the incident $TE_{3,1}$ mode into the operating eigenwave of the HW, at the input, and back to the $TE_{3,1}$ mode, at the output. The most favorable frequency region for the pulse compression is a part of the dispersion characteristic where the operating wave group velocity has a large negative gradient as a function of frequency, which, for the HW under consideration, is the region from 9.4 to 9.95 GHz (Fig. 2). Therefore, in order to be effectively compressed, an input pulse should have a negative frequency sweep within the mentioned frequency interval.

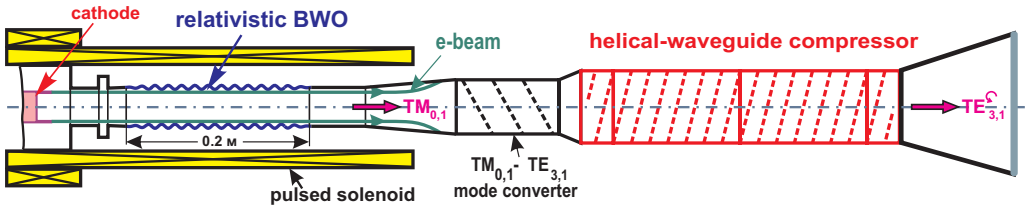

FIG. 1. (Color online) Scheme of the experimental setup.

Relativistic backward-wave oscillator. An analysis, based on a 1D theoretical model,[10] and more detailed numerical simulations using the time-domain particle-in-cell code KARAT (Ref. 11) were performed, resulting in the design of an RBWO which combined high output power, high efficiency which was able to be frequency tuned over a sufficiently wide range for a moderately relativistic electron beam.[7] According to the simulations, the RBWO oscillation frequency should smoothly sweep from 10 to 9.5 GHz when the accelerating voltage gradually changes in time from 600 to 300 kV.

The experiments were performed using a SINUS-6 accelerator (IAP RAS) where an accelerating voltage pulse was formed by a combination of a Tesla transformer and a coaxial transmission line. When operating to a matched load it produces pulses of voltage up to 600 kV and current of 6–7 kA with about 15 ns long flat top and 5–10 ns long rising/falling edges. Because of the principle of operation of the SINUS-6 accelerator it is very problematic to realize the necessary voltage sweep for the RBWO voltage over the main central region of the pulse by modifying the external circuit. Nevertheless, it was experimentally found how to realize an appropriate voltage drop "internally."[12] To achieve this change in voltage a dielectric cylinder was introduced into the region of the magnetically insulated coaxial diode where the electron beam was formed. Presumably due to some plasma effects, this dielectric insert led to a significant decrease (with characteristic time of 10–20 ns) of the diode impedance during the process of explosive-emission beam generation, resulting in a decrease in the accelerating voltage and an increase in the beam current at the top of the pulse [Fig. 3(a)]. Moreover, varying the axial distance between edges of the cathode and dielectric insert within several millimeters we could control the magnitude of the voltage drop and hence control the frequency sweep interval, which was used in the final experimental optimization of the combination of the RBWO with the compressor. At optimum configuration, when the top-pulse voltage decreased from 550 to 300 kV and beam current increased from 7 to 9 kA the RBWO generated radiation with power of 0.6–0.8 GW when frequency sweeping from 10 to 9.6 GHz during about 15 ns (Fig. 3).

The frequency sweep was measured by means of a heterodyne technique, when a small fraction of output radiation from the RBWO was nonlinearly mixed with radiation of a

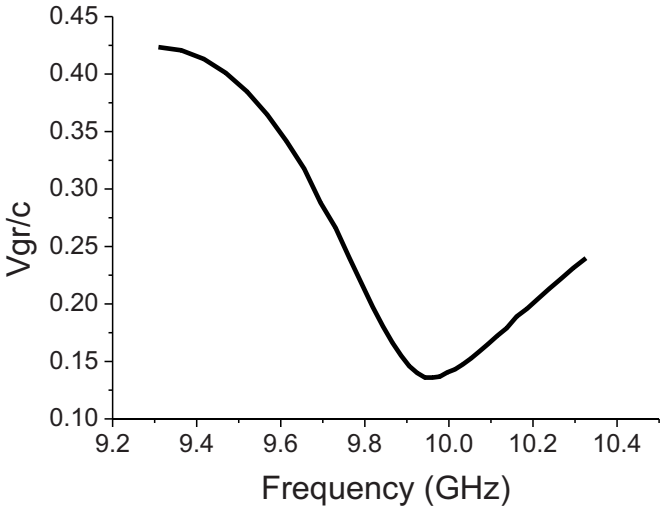

FIG. 2. Group velocity (normalized to the speed of light) of the helical waveguide operating wave.

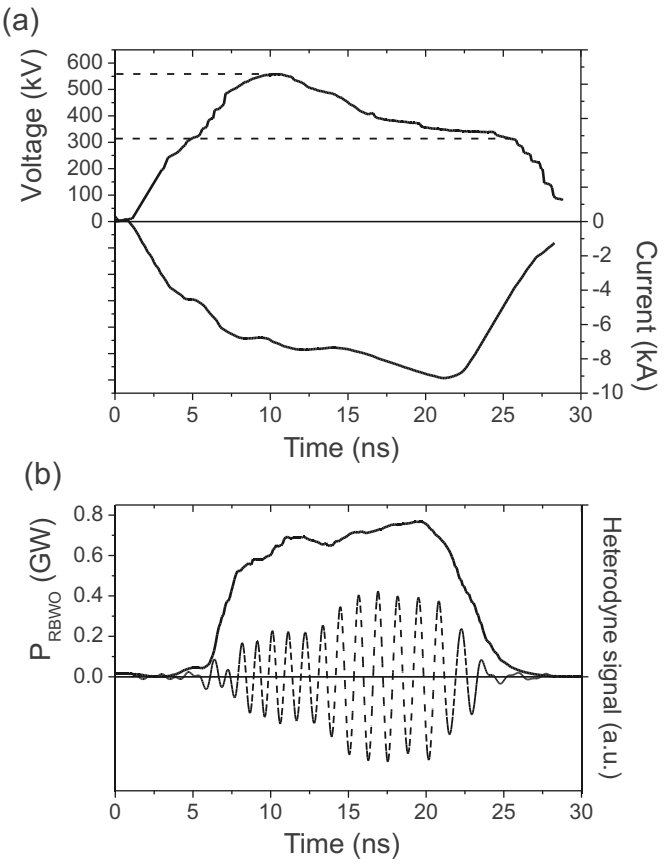

FIG. 3. Time characteristics of the relativistic backward-wave oscillator: (a) accelerating voltage (upper curve) and beam current (lower curve); (b) output power (solid curve) and heterodyne signal (dashed curve) at the master oscillator frequency of 9.1 GHz.

pulsed magnetron at a fixed frequency, resulting in a waveform at the intermediate frequency [Fig. 3(b), dashed curve]. The power of the output rf pulse [Fig. 3(b), solid curve] from the RBWO was obtained by processing of the rf detector signal, detector voltage-power calibration, and data from a calorimeter measuring the total rf energy in the pulse.

Combination of the RBWO and the HW compressor. The RBWO was combined with the HW compressor in a common vacuum system via a mode converter which transformed the power from the RBWO in the form of the $TM_{0,1}$ mode into the incident operating mode of the compressor, namely, the circularly polarized $TE_{3,1}$ mode (Fig. 1). The output power in the form of the $TE_{3,1}$ mode from the whole system was radiated through a horn terminated with a 300 mm diameter 0.3 mm thick lavsan window and then absorbed in a calorimeter with an aperture of 600 mm in diameter.

The experimental optimization aiming to obtain the maximum peak power of the compressed pulse was performed by variation of the axial distance between the cathode and dielectric insert, electron beam diameter (factors influencing the RBWO power and frequency sweep) and the length of the HW which could be adjusted in six-period-long sections. As a result the maximum peak power of the compressed pulse was measured to be as high as 3.2 GW while its halfwidth amounted to 2.2 ns with a total pulse energy of 9.7 ± 0.2 J (Fig. 4). As compared to the RBWO having approximately 0.7 GW pulse-averaged output power and 10.2 ± 0.2 J of pulse energy, a 4.5-fold power amplification due to the compression was achieved. Assuming the energy content in a "useful" pulse as a product of its peak power and halfwidth an compressing efficiency of nearly 70% was realized. (The rest of energy goes to Ohmic losses and the pulse sidelobes.)

It should be noted that the achievable power compression ratio by the method discussed is approximately proportional to the input FM pulse width. Therefore if the duration of the RBWO accelerating voltage pulse (which should have a negative slope) is increased from 15 ns, as used in the experiment presented, to 40–50 ns and the HW compressor is proportionally elongated a further threefold power increase of the compressed pulse is achievable. In conclusion, the method of generation of ultra-high-power microwave pulses based on a combination of a voltage-swept RBWO and an HW compressor has been experimentally demonstrated at multigigawatt power levels and has a serious potential for further peak power enhancement.

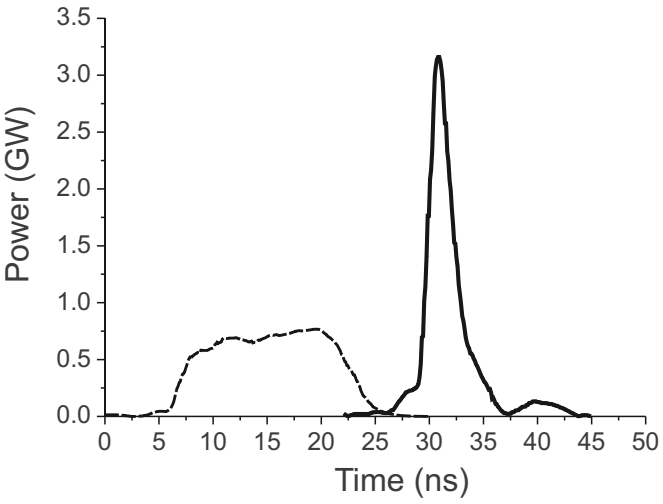

FIG. 4. The resultant compressed pulse (solid curve) shown in contrast with the relativistic backward-wave oscillator output pulse (dashed curve).

This work was supported by the Russian Foundation for Basic Research (Grant No. 10-02-00975) and the EPSRC U.K. (Grant No. EP/E058868/1).

[1] *Applications of High-Power Microwaves*, edited by A. V. Gaponov-Grekhov and V. L. Granatstein (Artech, Norwood, MA, 1994).
[2] S. P. Bugaev, V. A. Cherepenin, V. I. Kanavets, V. I. Koshelev, V. A. Popov, and A. N. Vlasov, IEEE Trans. Plasma Sci. **18**, 525 (1990).
[3] A. A. Eltchaninov, S. D. Korovin, G. A. Mesyats, I. V. Pegel, V. V. Rostov, V. G. Shpak, and M. I. Yalandin, IEEE Trans. Plasma Sci. **32**, 1093 (2004).
[4] W. M. Manheimer and B. H. Ripin, Phys. Fluids **29**, 2283 (1986).
[5] M. K. Thumm and W. Kasparek, IEEE Trans. Plasma Sci. **30**, 755 (2002).
[6] S. V. Samsonov, A. D. R. Phelps, V. L. Bratman, G. Burt, G. G. Denisov, A. W. Cross, K. Ronald, W. He, and H. Yin, Phys. Rev. Lett. **92**, 118301 (2004).
[7] V. Bratman, G. G. Denisov, S. V. Samsonov, A. W. Cross, K. Ronald, and A. D. R. Phelps, Radiophys. Quantum Electron. **50**, 36 (2007).
[8] O. Svelto and D. C. Hanna, *Principles of Lasers*, 4th ed. (Springer, New York, NY, 1998).
[9] R. H. Lehmberg and J. M. McMahon, Appl. Phys. Lett. **28**, 204 (1976).
[10] B. Levush, T. Antonsen, A. Bromborsky, W. R. Lou, and Y. Carmel, Phys. Fluids B **4**, 2293 (1992).
[11] V. P. Tarakanov, *User's Manual for Code KARAT* (Berkley Research, Springfield, VA, 1992).
[12] A. M. Bechasnov, V. L. Bratman, N. G. Kolganov, S. V. Mishakin, and S. V. Samsonov, Tech. Phys. Lett. **36**, 140 (2010).